PONTIFICIA UNIVERSIDAD CATOLICA DE CHILE
SCHOOL OF ENGINEERING

THERMOPHOTOVOLTAIC CELL DESIGN IMPROVEMENTS THROUGH NUMERICAL SIMULATIONS: UNCERTAINTY QUANTIFICATION AND GEOMETRY OPTIMIZATION

GERARDO ANDRÉS SILVA OELKER

Thesis submitted to Pontificia Universidad Católica de Chile and University of Notre Dame in partial fulfillment of the requirements for the degree of Doctor in Engineering Sciences

Advisors:
CARLOS JEREZ-HANCKES
PATRICK FAY

Santiago de Chile, January 2019

PONTIFICIA UNIVERSIDAD CATOLICA DE CHILE

SCHOOL OF ENGINEERING

THERMOPHOTOVOLTAIC CELLS DESIGN IMPROVEMENTS THROUGH NUMERICAL SIMULATIONS: UNCERTAINTY QUANTIFICATION AND GEOMETRY OPTIMIZATION

GERARDO ANDRÉS SILVA OELKER

Members of the Committee:

CARLOS JEREZ

PATRICK FAY

MANUEL SOLANO

SEBASTIAN REYES

MARCELO GUARINI

KEN SAUER

JORGE VÁSQUEZ

Thesis submitted to Pontificia Universidad Católica de Chile and University of Notre Dame in partial fulfillment of the requirements for the degree of Doctor in Engineering Sciences

Santiago de Chile, January, 2019

To my wife, for her love, patience,
and support.

ACKNOWLEDGEMENTS

Firstly, I would like to express my most sincere gratitude to my advisors Dr. Carlos Jerez–Hanckes for his help, support, and always trying to put me back on track, and Dr. Patrick Fay, who is always willing to put aside his own work for a discussion or to solve any physical or existential problem. I express my gratitude to both of them for giving me the opportunity to join their research groups and for their patience, motivation, and advice.

Besides my advisors, I would like to thank the rest of my PUC thesis committee: Dr. Manuel Solano, Dr. Sebastian Reyes, and Dr. Marcelo Guarini as well as the ND committee: Dr. David Burghoff, Dr. Scott Howard, and Dr. Ken Sauer for their insightful comments and questions which incentivized me to widen my research from various perspectives. My special and sincere thank to Dr. Anthony Hoffman, for his advice, support, and willingness to answer every single question.

I thank my fellow labmates at PUC José (Pintoso) Pinto, Rubén (Rubensio) Aylwin, and Paul Escapil-Inchauspé for the stimulating discussions and their support with the *obscure* world of the boundary elements method. I also thank my labmates at ND, especially my friend Roy Stillwell, who always was there to help me with insightful comments, correct my precarious English, and share a beer when necessary. I also thank my friends Marcela Natalia Vega Muñoz, Jorge (JCrew) Morales, and Francisco (Pancho) Herrera for their continuous support and help, as well as Paolo Paletti and David Connelly, who always had time to help me with my endless lists of questions about devices and circuits.

My gratitude also goes to the entire "Chilean community" in South Bend for the countless barbecues and beers.

Last but not least, I want to express my entire gratitude to my wife, Fernanda, for her inexhaustible patience, support, love, and constant encouragement to finish this thesis. None of this would have been possible without her.

This thesis research was supported by Comisión Nacional de Investigación Científica y Tecnológica (CONICYT), Becas de Doctorado Nacional and Vicerrectoría de Investigación of PUC.

TABLE OF CONTENTS

LIST OF FIGURES

LIST OF TABLES

ABSTRACT

Two avenues of research on numerical simulations to achieve robust designs in thermophotovoltaic (TPV) energy conversion devices are explored. For the first of these, a recently proposed numerical scheme able to quantify performance changes due to shape perturbations and its application to one-dimensional (1D) gratings is investigated. The second avenue, also based on numerical simulations, focuses on the study of gratings as selective emitters to enhance TPV cell energy conversion efficiency.

In the first part, we present a novel deterministic method capable of calculating statistical moments of transverse electric polarized fields scattered by perfect electric conductor gratings with small surface random perturbations. Based on a first-order shape Taylor expansion, the resulting electric field integral equations are solved via the method of moments with constant hierarchical basis or Haar wavelets. This allows for a sparse tensor approximation, significantly reducing the number of required unknowns and yielding a higher rate of convergence than a dense approximation. Moreover, the proposed approach converges faster than Monte-Carlo simulations with significantly less computational effort. Validation of the proposed approach is performed for several cases, and simulations applied to the calculation and prediction of grating efficiency for realistic grating structures reveal the applicability of the method.

In the second part, we explores the performance potential of gratings based on tungsten/hafnia (W/HfO_2) stacks for thermophotovoltaic thermal emitters via numerical simulations. Structures consisting of a W grating over a HfO_2 spacer layer and a W substrate are analyzed over a range of geometries. For shallow gratings (W grating thickness much smaller than the grating pitch), an emittance of 99.9% can be achieved for transverse magnetic (TM) polarization, but the transverse electric (TE) performance is appreciably lower. For deep gratings (W grating thickness on the order of the grating pitch), peak emittances

of 97.7% and 99.7% for TE and TM polarizations, respectively, are achieved. We find that both surface plasmon polaritons and magnetic polaritons play a crucial role in shaping the emittance for TM radiation. On the other hand, cavity resonances are responsible for the almost perfect emittance in the case of TE polarization. These results suggest that by introducing an HfO_2 layer it is possible to reach high emittance for operating temperatures that match the absorption characteristics of GaSb and InGaAs photovoltaic cells.

In addition, tungsten-hafnia (W-HfO_2) selective thermal emitters with high hemispherical emittance for thermophotovoltaic (TPV) applications are explored through numerical simulations. Two structures were analyzed: a planar multilayer stack and a grating. In both cases, through suitable design choices high thermal emittance with low directional sensitivity can be obtained. The designs are obtained by optimization of the structures using a genetic algorithm and a suitable cost function, along with simulations of the structures' emittance by using rigorous coupled wave analysis. Calculations show that these optimized structures possess high hemispherical thermal emittance for the wavelength range that matches the optical response of GaSb photovoltaic cells. For each structure, both the output power from the TPV cell and the conversion efficiency are studied as a function of emitter temperature and physical understanding of the optimized structures is developed.

Keywords: Thermophotovoltaics, gratings, periodic structures, boundary elements method, numerical methods, surface plasmon polaritons, computational electromagnetics.

RESUMEN

En esta tesis se exploran dos líneas de investigación basadas en simulaciones numéricas para aplicaciones en celdas termofotovoltaicas (TPV por sus siglas en inglés). En primer lugar, se investiga un método numérico propuesto recientemente, el cual permite cuantificar cambios en el desepeño de estructuras periódicas unidimensionales, llamadas *gratings*, debido a perturbaciones de forma en su superficie. La segunda línea, también basada en simulaciones numéricas, está enfocada en el estudio de estructuras periódicas como parte de emisores térmicos en sistemas TPV y en como estas estructuras permiten mejorar la eficiciencia de dichas celdas.

En la primera parte, presentamos un nuevo modelo capaz de calcular momentos estadísticos del campo dispersado en *gratings* en forma determinística. Se estudian estructuras con superficies perfectamente conductoras perturbadas estocásticamente, las cuales dispersan radiación incidente polarizada en forma transversal eléctrica. El método se basa en una expansión de Taylor de la derivada de forma a primer orden, resultando en ecuaciones integrales las cuales son resueltas a través del método de los momentos con bases jerárquicas llamadas *wavelets* de Haar. Dichas bases permiten una aproximación no densa, la cual reduce significativamente el número de incógnitas requeridas y, además, entrega una mayor tasa de convergencia al compararlo con una aproximación densa. Junto a lo anterior, mostramos que el método propuesto converge más rápido que el conocido método de Monte-Carlo, requiriendo menor esfuerzo computacional. El modelo es validado mediante la comparación con diferentes casos y, junto con ello, simulaciones aplicadas a problemas de eficiencia de difraccción en *gratings* revelan la aplicabilidad del método propuesto.

En la segunda parte, se investiga el potencial desempeño de *gratings* basados en capas de tungsteno (W) y hafnia (HFO_2) como emisores térmicos selectivos en celdas TPV. Estructuras que consideran un grating de tungsteno sobre una capa de hafnia y un substrato

de tungsteno son analizadas para diferentes geometrías. El primer caso considera *gratings* poco profundos (donde el espesor del grating de tungsteno es mucho menor que el paso del grating), logrando una emitancia térmica del 99 % para ondas transverales magnéticas (TM), no obstante, el desempeño que presenta dicha estructura es deficiente para la radiación transversal eléctrica (TE). Un segundo caso considera *gratings* profundos (donde el espesor del *grating* de tungsteno es del orden de magnitud del paso del grating), para el cual *peaks* de emitancia del 98% y el 99% son obtenidos para las polarizaciones TE y TM, respectivamente. En ambos casos encotramos que tanto plasmones polaritones superficiales y polaritones magnéticos juegan un rol crucial para la polarización TM. Por otra parte, las resonancias de cavidad son las responsables de la alta emitancia térmica en el caso de la polarización TE. Estos resultados sugieren que introduciendo una capa de HfO_2 es posible alcanzar altas emitancias para temperaturas de operación las cuales se ajustan a las características ópticas de las celdas fotovoltaicas compuestas de GaSb y InGaAs.

Junto a lo anterior, presentamos dos estructuras unidimensionales de sencilla fabricación compuestas por tungsteno y hafnia como emisores térmicos para aplicaciones en celdas TPV. Analizamos numéricamente y comparamos dos estructuras; una multicapa y una *grating* para los cuales se obtuvo alta emitancia térmica y baja sensibilidad a la dirección de la radiación. Se realizó una optimización de la geometría a través de un algoritmo genético (GA por sus siglas en inglés) y una adecuada función de costo junto con el método riguroso de acoplamiento de ondas. Los cálculos muestran que estas estructuras poseen alta emitancia térmica hemisférica para rangos de longitudes de onda que se ajustan a la respuesta óptica de celdas fotovoltaicas tales como InGaAs y GaSb. Para cada estructura analizamos la emisividad en-banda (*in-band emissivity*) y la eficiencia espectral, así como también la potencia emitida por los emisores. El desempeño de dichos emisores es evaluado tanto para diferentes longitudes de onda de corte de emisión como temperaturas. Además, a través de simulaciones numéricas y consideraciones teóricas, entregamos explicaciones acerca de la mejora en la emitancia. Por último, dado que el algoritmo de optimización sugiere espesores de tungsteno delgados, también se ha realizado un análisis de tolerancia.

Palabras Claves: Celdas termofotovoltaicas, *gratings*, estructuras periódicas, método de elementos de borde, métodos numéricos, plasmones polaritones superficiales, electromagnetismo computacional.

You can know the name of that bird in all the languages of the world, but when you're finished, you'll know absolutely nothing whatever about the bird. You'll only know about humans in different places, and what they call the bird. ... —RICHARD FEYNMAN

I can live with doubt and uncertainty and not knowing. I think it is much more interesting to live not knowing than to have answers that might be wrong. —RICHARD FEYNMAN

NOTATION

General notation

$\mathbf{D}$	electric displacement
$\mathbf{E}$	electric field
$\mathbf{B}$	magnetic flux
$\mathbf{H}$	magnetic field
$\mathbf{J}_s$	surface current density in Chapter 1
ζ	surface current density in Chapter 2
Ω	probability space
$\langle \cdot, \cdot \rangle$	inner product
D	spatial domain
$\Gamma := \partial D$	surface of the spatial domain D
$\hat{n}$	unitary vector
θ_i	angle of incidence
Λ	structure period
Ω	stochastic domain
ε	dielectric constant
μ	permeability
σ	electrical conductivity
n	refraction index
$\mathbf{k}$	wavevector
$k := \lvert\mathbf{k}\rvert$	wavenumber with components k_i, $i = x, y, z$
λ	wavelength
ω	angular frequency in Chapter 1

ω	stochastic parameter in Chapter 2
M	number of realizations of Monte Carlo method
N_k	number of oscillators in the Lorentz's model
l, m, n	integers
$\imath$	imaginary
φ	basis functions
G	Green functions
e_n	diffraction efficiency of the n-mode
$\mathcal{I}$	index set
u	scalar electric or magnetic field
ϵ	perturbation in Chapter 2
ϵ_{in}	in-band emissivity in Chapters 3 and 4
η_{sp}	spectral efficiency in Chapters 3 and 4

Operators

$\mathcal{A}$	linear operator
d	derivative
$\partial_{\mathbf{n}}$	normal derivative
∇_t	tangential gradient
SL	single layer potential
DL	double layer potential
$\mathcal{V}$	weakly singular operator

Var	variance
Cor	correlation
$\mathbb{E}$	expected value
$\Delta = \nabla \cdot \nabla = \nabla^2$	Laplacian operator
$\mathcal{M}^{(q)}$	q-moment operator
$\partial_{\mathbf{n}}$	normal derivative

Subscripts	i, j, k	integers
Upper scripts	p	periodic
	s	scattered
	i	incident
Accents	$\overline{()}$	complex conjugate
	$\dot{()}$	shape derivative

1. INTRODUCTION AND BACKGROUND

1.1. Introduction and Motivation

Thermophotovoltaic (TPV) energy conversion is a novel technology that may offer some unique advantages. The use of a TPV cell is a clever way to use solar energy or to recycle waste heat from industrial processes, such as nuclear generation (Teofilo, Choong, Chang, Tseng, & Ermer, 2008), concentrated solar power (CSP) waste heat (Seyf & Henry, 2016), and other high temperature industrial processes. TPV cells are static energy conversion devices—which means no moving parts—composed of a thermal emitter coupled to a photovoltaic (PV) cell. The PV cell is responsible for converting the thermal radiation from the emitter into electricity. A key enhancement of this approach is to use an emitter with an output spectrum that has been tailored to match the response of the PV cell (vs. using blackbody radiation). Furthermore, according to Carnot's efficiency, it is possible to reach efficiencies as high as 80%—depending on the operation temperature. These characteristics make TPV cells a promising alternative for energy harvesting. Proposing new ways to improve their design is what motivates this work.

Periodic electromagnetic structures have been intensively studied over the last few decades due to their remarkable properties. One, two, and three dimensional photonic crystals—periodic structures in which the characteristic wavelength is of the same order of magnitude as the period of the structure—have been modeled and implemented in different novel technologies. On the other hand, metamaterials—structures for which the characteristic wavelength is much greater than the characteristic periodicity within the structure—have also been studied numerically and experimentally, and successfully implemented since being proposed by Veselago (Veselago, 1968). Among these periodic structures, gratings are particularly useful in a wide range of applications. Examples of applications include waveguide grating couplers (Taillaert et al., 2006; Xiao, Liow, Zhang, Shum, & Luan, 2013), optical spectrometers (Fortin & McCarthy, 2005), X-ray spectroscopy in space missions (McEntaffer et al., 2013), and thin film tandem solar cells (Solano et al., 2013). Critical to their usefulness, gratings present Wood's anomalies (Wedlockt, 1963)

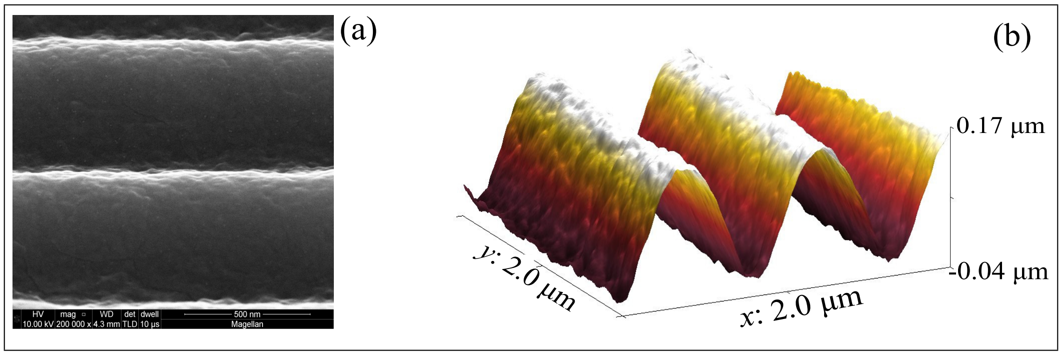

FIGURE 1.1. (a) SEM and (b) AFM images of a sinusoidal grating. The grating was obtained from Richardson gratings, model 53-220H.

allowing, for example, the management of optical properties, such as transmittance, reflectance, and absorptance. As a result, they have been utilized in TPV cells for improving the thermal-electric energy conversion efficiency (Y.-B. Chen & Zhang, 2007; Nguyen-Huu, Chen, & Lo, 2012; Ghanekar, Sun, Zhang, & Zheng, 2017).

In the scientific community, it is commonly accepted that experimentalists must, to the extent possible, provide a measure of the uncertainty in their data. However, the computational science community rarely provides similar estimates for simulation results. Uncertainties remain important in a simulation context, though, because these simulations are typically attempting to represent a physical system, which inherently has uncertainties related to input parameters (e.g., geometry, material, parameters, etc). For this reason, most analyses of gratings are based on idealized and simplified representations. For example, one typically assumes that the surfaces of the gratings are smooth and that the structure is perfectly periodic. In practice, these assumptions are not perfectly satisfied due to random fluctuations. Let us consider the following example. Manufacturing processes lead to some imperfections or variability in the products. These imperfections are random and, to a certain extent, it is not possible to fully eliminate them. In Fig. 1.1 measured SEM and AFM images of a grating surface are shown. In both cases it can be noticed that even though the grating is manufactured to exacting tolerances it still exhibits surface roughness. One branch of mathematics, called Uncertainty Quantification (UQ), seeks to provide powerful tools to quantify this sort of randomness. However, in many cases these tools are computationally too expensive to be used routinely. Providing a reliable and fast tool to quantify the impact of surface random perturbations on important properties of gratings, such as diffraction efficiency, would be valuable in the design and analysis of grating–based components as the case of TPV devices.

One of the main components of a TPV cell is the selective emitter. These components are intended to emit thermal radiation that matches the PV cell response in order to improve the conversion efficiency. To tune the emittance of the emitters, periodic structures have demonstrated enormous potential. Despite a considerable body of the extensive literature dedicated to their theoretical and experimental analysis as well as simulations, further improvements can be made, for example, by considering different materials and geometries that can facilitate the manufacturing of TPV devices. Management of the thermal emittance of gratings to improve the spectral matching between the emitter and PV cell is the second motivation of this thesis.

In this thesis, two different goals have been raised. On the one hand, we demonstrate the formulation and implementation of algorithms able to quantify the impact of surface roughness on grating efficiency. On the other hand, this work explores ways to improve the energy conversion efficiency of TPV cells, by simulating different grating-based thermal emitters and understanding the new phenomena that arise under different configurations. The primary scope of this work is numerical, providing key details of the simulations and design guidelines, although connections to experimental results are also considered in order to validate the developed approaches.

1.2. Goals

To provide direction to the research, two over-arching goals are proposed. The first of these is to quantify the impact of random surface perturbations on the performance of gratings, including practical figures of merit such as diffraction efficiency. The second goal centers around the development and use of mathematical tools to improve the efficiency of TPV devices by managing the thermal emittance spectrum of gratings-based thermal emitters.

1.2.1. Impact of Surface Perturbations on Grating Performance

The following specific sub-tasks have been performed:

(i) Develop a model based on the Method of Moments (MoM) to obtain the scattered electromagnetic field from a perfectly conducting grating and to calculate the grating efficiency;

(ii) Develop a model based on shape derivatives to quantify surface perturbations;

(iii) Using the models developed above, apply the MoM formalism to the case of transverse electric polarized incident radiation to quantify the impact of surface perturbations on the grating efficiency;

(iv) Analyze and evaluate the limitations of the proposed models, as well as their advantages for computational efficiency, accuracy, etc.

1.2.2. Spectrally Selective Thermal Emitters for Thermophotovoltaics

For the second research thrust, the proposed research included the following tasks:

(i) Evaluate the optical properties, such as transmittance, reflectance, and absorptance in metallic gratings incorporating dielectric layers, based on the rigorous coupled wave analysis method to improve thermal emittance for TPV applications;

(ii) Calculate the emittance spectrum under different conditions, including polarization effects;

(iii) Study the nature of the improvements of thermal emittance through numerical simulations and theoretical considerations;

(iv) Optimize the geometry of the proposed thermal emitters through the implementation of a genetic algorithm (GA);

(v) Quantify the efficiency of selective thermal emitters;

(vi) Analyze the limitations of the approach, and benchmark against prior theoretical and experimental reports.

1.3. Thermophotovoltaic (TPV) Cells

1.3.1. Principles

TPV cells operate under the same basic principles as conventional photovoltaic cells, namely, they transform incident electromagnetic radiation into DC electrical power. The key differentiation between conventional PV solar cells and TPV cells is the intended radiation source and spectrum. While PV cells generally target solar radiation and consequently light in the visible and near infrared, TPV cells use a hot thermal emitter as the source of energy, and thus work much further into the infrared. Thermophotovoltaic cells have a range applications due to their flexibility. For example, solar concentrators (Bermel et al., 2016; Coutts, 1999) and microgenerators (Bermel et al., 2010; W. R. Chan et al., 2013, 2015) are illustrated in Fig. 1.2. In addition, TPVs are promising for powering deep-space probes, and for power generation without moving parts (e.g. for quiet operation). As is well-known, the energy of photons must be greater than the electronic band gap (E_g) of the cell. Materials used in TPV cells therefore are typically made using much lower band gap materials than are solar PV cells. TPV cells using materials such as GaSb ($E_g = 0.72$ eV) (Ungaro, Gray, & Gupta, 2015), $In_{0.53}Ga_{0.47}As$ ($E_g = 0.74$ eV) (Zhou, Sakr, Sun, & Bermel, 2016), and $Ga_{0.82}In_{0.18}As_{0.16}Sb_{0.84}$ ($E_g = 0.55$ eV) (Dashiell et al., 2006) have been considered.

The reason why TPV cells are typically made with materials having band gaps between 0.5 and 0.8 eV comes from the relationship between the blackbody emission law (Wien's law) and the photovoltaic effect. This is illustrated in Fig. 1.3. Since the source of radiation for TPV cells is a heated thermal emitter, typically to temperatures on the order of 1500 K, the peak spectral irradiance according to Wien's law is approximately 1.9 μm (0.65 eV). As can be seen in Fig. 1.3, however, the emission spectrum is quite broad and with much of the total energy carried by photons with energies well below the peak. This makes realizing an

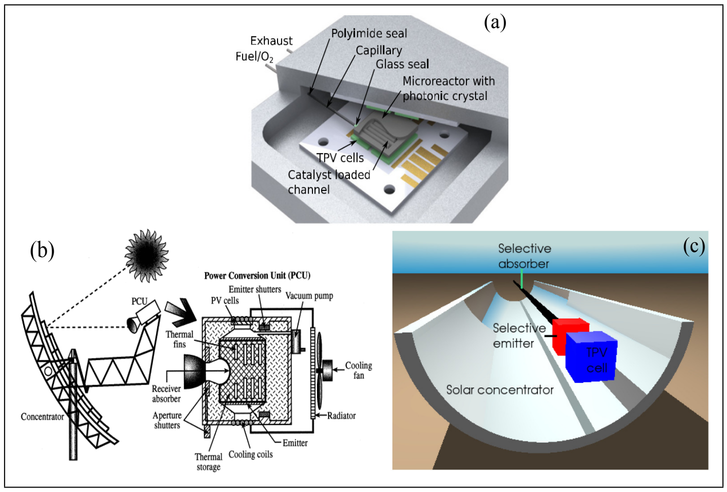

FIGURE 1.2. Example applications of TPV cells: (a) a microgenerator (W. R. Chan et al., 2013), (b) a solar power TPV system (Coutts, 1999), and (c) a parabolic concentrator (Bermel et al., 2016).

efficient TPV cell with blackbody radiation very difficult. One of the keys for improving TPV energy conversion efficiency is more sophisticated spectral control to tailor the emission spectrum to allow efficient absorption. This can be achieved by using periodic structures, such as metamaterials (Deng, Wang, Gao, & Yang, 2014; H. Wang, Chang, Yang, & Wang, 2016) and photonic crystals (Rinnerbauer & Lenert, 2014; Celanovic, O'Sullivan, Jovanovic, Qi, & Kassakian, 2004) to engineer the emission spectrum (Celanovic, 2006).

1.3.2. Components

In order to design and optimize a TPV system, an understanding of the main components of a TPV device and how they interact is needed. Figure 1.4 shows the major components schematically. A source of heat, shown in pink in Fig. 1.4, is the prime source of energy. This can be derived from combustion, an exothermic chemical reaction, radioactive decay, or other physical processes. This heat source, by its nature, typically exhibits a blackbody emission spectrum. To enhance cell performance, this emission spectrum can be "reshaped" to reduce the energy in the long-wavelength "tail" below the TPV band gap (see Fig. 1.3). One approach for this is to absorb the energy from the heat source (using

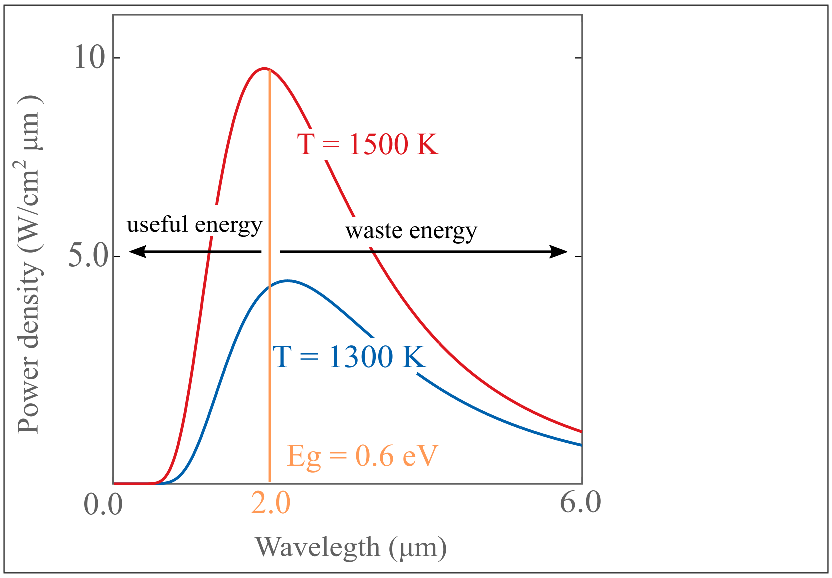

FIGURE 1.3. Spectrum of black body emission at 1300 and 1500 K. The wavelength corresponfing to the peak of the emission is given by Wien's law. A band gap of 0.6 eV is shown to compare it with the emission peak.

an absorber) followed by re-emission using a spectrally-selective emitter (see the light blue boxes in Fig. 1.4)

The main goal of the emitter is to re-emit radiation in a range of frequencies/wavelengths just above the band gap of the PV cell. As stated above, thermal emitters typically operate at high temperatures; as an example, emitters suitable for use with GaSb PV cells ($E_g = 0.72$ eV) require an operating temperature of approximately 1683 K. For this reason, the emitter must be made of high melting point materials. As a result, structures built of refractory metals such as tungsten (Yeng et al., 2012), tantalum (Rinnerbauer et al., 2013), and molybdenum (Zhou, Chen, & Bermel, 2015) have been proposed and analyzed.

The PV cell performs the conversion from the incident thermal radiation into electricity. Each component of the TPV cell has been evaluated as a function of the cell band gap. As mentioned above, some common materials used in TPV designs are GaSb (Celanovic et al., 2004; Deng et al., 2014; Yong, Sid-ahmed, & Ming, 2014; Babiker, Shuai, Sid-Ahmed, & Xie, 2014), InGaAs (Tan et al., 2014; Sinharoy et al., 2005; Su, Fay, Sinharoy, Forbes, & Scheiman, 2007), and InGaAsSb (Nam et al., 2014). In addition, in practice a filter is often

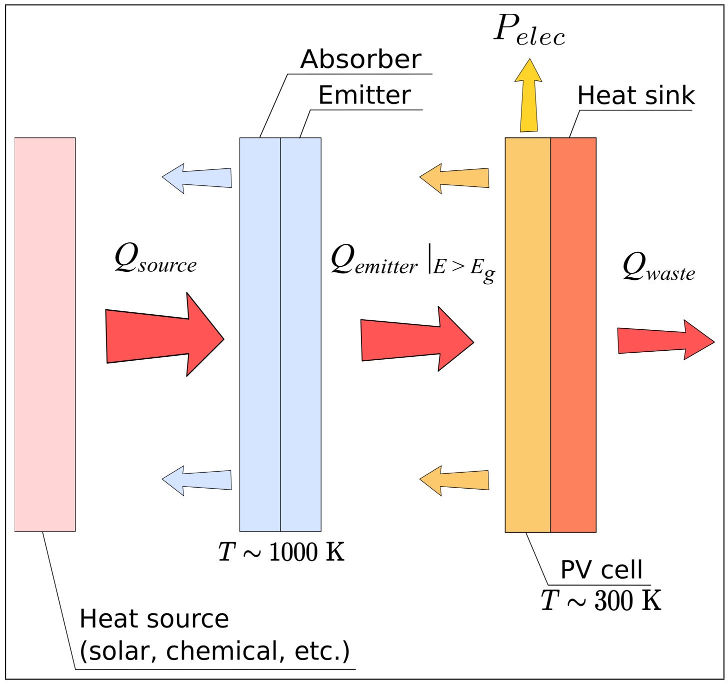

FIGURE 1.4. Components of a TPV cell: Heat source (pink), absorber and emitter (light blue), PV cell (yellow), and the heat sink (orange). Also noted are typical magnitudes for temperatures of each component.

placed between the emitter and the PV cell in order to recycle below band gap photons and to prevent the cell from absorbing photons that greatly exceed the band gap, and a heat sink is used to ensure the temperature of the cell does not rise too much (since cell reverse current increases with temperature, lowering conversion efficiency) (Mbakop, Djongyang, & Raidani, 2016).

1.3.3. Efficiency

The maximum efficiency attainable by a TPV cell is given by the well-known Carnot efficiency, which is given by $\eta = 1 - T_{low}/T_{high}$. The theoretical limit for TPV conversion has been calculated to be 85 % (Harder & Würfel, 2003). It has been shown theoretically that for solar TPV (STPV) under the right conditions— no optical losses, only radiative recombination in the solar cell, and full concentration of the incident sunlight on a black absorber—STPV energy conversion can exceed the Shockley-Queisser limit (Rephaeli &

TABLE 1.1. Reported energy conversion efficiency for TPV and STPV cells

Work	Description	PV cell	Efficiency	Year	Ref.
Simulation	STPV	InGaAs	6.93 %	2005	(Sinharoy et al., 2005)
Sim./Exp.	STPV	InGaAs/InAsP	7.8 %	2007	(Su et al., 2007)
Sim./Exp.	STPV	InGaAsSb	10 %	2014	(Nam et al., 2014)
Experimental	STPV	InGaAsSb	5.8 %	2014	(Lenert et al., 2014a)
Experimental	STPV, 2483 suns	GaSb	6.2 %	2015	(Ungaro et al., 2015)
Experimental	PhC	Si	1.18 %	2015	(Yeng et al., 2015)
Simulation	PhC	Si	6.40 %	2015	(Yeng et al., 2015)
Simulation	Metamaterials	InGaAsSb	10 %	2016	(H. Wang et al., 2016)
Simulation	Spectral optimization	c-Si	44.32 %	2017	(Rabady, 2017)

Fan, 2009; Zhou et al., 2015). However, actual reported efficiencies to date are well below these theoretical limits. In Table 1.1 a sampling of simulation and experimental TPV studies and their energy conversion efficiencies is shown. As can be observed, there is considerable scatter among the results due to different designs, operating conditions, and material choices. However, one can see that efficiency of 10% or less is typical, unless careful spectral optimization is performed.

1.4. Fundamentals of Electromagnetism

The main focus of this thesis is on electromagnetic modeling for scattering problems, particularly from periodic structures. We start with Maxwell's equations, which describe how the electric and magnetic fields are related as well as the interaction between electromagnetic fields and matter.

1.4.1. Maxwell's Equations and Constitutive Relations

In their non-relativistic, macroscopic, and differential form, Maxwell's equations are given by (Sheng & Song, 2012):

$$\nabla \cdot \mathbf{D} = \rho, \tag{1.1}$$

$$\nabla \cdot \mathbf{B} = 0, \tag{1.2}$$

$$\nabla \times \mathbf{E} = -\frac{\partial \mathbf{B}}{\partial t}, \tag{1.3}$$

$$\nabla \times \mathbf{H} = \mathbf{J} + \frac{\partial \mathbf{D}}{\partial t}, \tag{1.4}$$

where $\mathbf{E}$ and $\mathbf{D}$ are the electric field intensity (Vm^{-1}) and electric displacement (Cm^{-2}), respectively, $\mathbf{H}$ is the magnetic field intensity (Am^{-1}) and $\mathbf{B}$ is the magnetic flux density (Wbm^{-2}). In addition, $\mathbf{J}$ is the volume current density (Am^{-2}) and ρ is the free charge density. The interaction between electromagnetic fields and matter can be described by the constitutive relations:

$$\mathbf{D} = \varepsilon \mathbf{E}, \tag{1.5}$$

$$\mathbf{B} = \mu \mathbf{H}, \tag{1.6}$$

$$\mathbf{J} = \sigma \mathbf{E}. \tag{1.7}$$

In these equations, ε, μ, and σ stands for permittivity (Fm^{-1}), permeability (Hm^{-1}), and electrical conductivity (Sm^{-1}), respectively.

This set of differential equations requires a set of boundary conditions, which are given by the continuity of the electric and magnetic fields at interfaces. By applying Maxwell's equations to a thin control volume surrounding an interface between two different media—called media 1 and 2—we obtain the following boundary conditions (Sheng & Song, 2012;

G. Chen, 2005)

$$\begin{aligned} \hat{n} \cdot (\mathbf{D}_2 - \mathbf{D}_1) &= \rho_s, & (1.8) \\ \hat{n} \times (\mathbf{E}_2 - \mathbf{E}_1) &= 0, & (1.9) \\ \hat{n} \cdot (\mathbf{B}_2 - \mathbf{B}_1) &= 0, & (1.10) \\ \hat{n} \times (\mathbf{H}_2 - \mathbf{H}_1) &= \mathbf{J}_s. & (1.11) \end{aligned}$$

Equations (1.8) and (1.11) establish that the difference between perpendicular components of the electric displacement and the magnetic fields must be equal to the charge density (ρ_s) and surface current density ($\mathbf{J}_s$) across the interface, respectively. Meanwhile, Equations (1.9) and (1.10) enforce the continuity of parallel and perpendicular components of the electric field and the magnetic flux, respectively. In this work, we are interested in finding the electromagnetic fields in the frequency space in order to analyze their spectral behavior. Threfore, we are going to assume a time-harmonic fields ($e^{i\omega t}$). With this assumption, Maxwell's equations can be written in the frequency domain form as:

$$\begin{aligned} \nabla \cdot \mathbf{D} &= \rho, & (1.12) \\ \nabla \cdot \mathbf{B} &= 0, & (1.13) \\ \nabla \times \mathbf{E} &= -i\omega \mathbf{B}, & (1.14) \\ \nabla \times \mathbf{H} &= \mathbf{J} + i\omega \mathbf{D}. & (1.15) \end{aligned}$$

In addition to the boundary conditions (1.8)–(1.11) , for scattering problems—where the domain is unbounded—a condition when $r \to \infty$ is required. This the the so-called Silver–Müller radiation condition (Sheng & Song, 2012; Chandler-Wilde, 1995) and it is given by the following limit:

$$\lim_{r \to \infty} r \left(\nabla \times \begin{pmatrix} \mathbf{E} \\ \mathbf{H} \end{pmatrix} + ik\hat{r} \begin{pmatrix} \mathbf{E} \\ \mathbf{H} \end{pmatrix} \right) = 0, \tag{1.16}$$

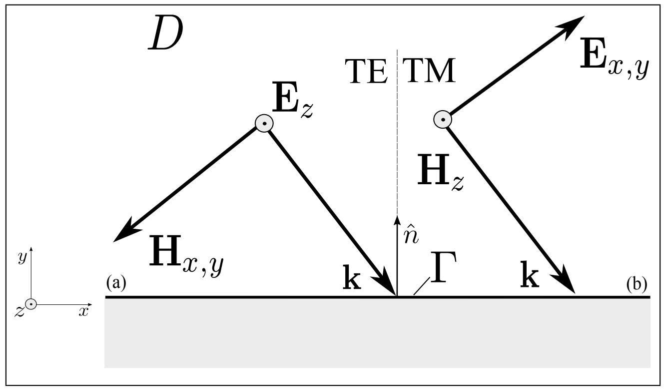

FIGURE 1.5. Description of the (a) transverse electric (TE) and (b) transverse magnetic polarizations (TM) of a plane propagating in a direction ($\mathbf{k}$) with the $x - y$ plane in a domain D and impinging on a surface Γ.

where $i := \sqrt{-1}$, k is the wavenumber defined as $k := \omega/c$, and ω and c are the angular frequency and the speed of light in the media, respectively.

1.4.2. Transverse Electric and Transverse Magnetic Problems

Part of this thesis is focused on scattering from perfect electric conductor (PEC) surfaces. On a PEC surface, the tangential component of the electric field as well as the normal component of the magnetic field must vanish. In general, scattering from a PEC surface under TE or TM radiation is known as a *Dirichlet* or *Neumann* problem, respectively. It is not hard to show the relation between the TE (also TM) radiation and the Dirichlet (also Neumann) boundary condition. In the case of TE radiation, since the electric field must vanish at the surface ($\Gamma := \partial D$, Fig. 1.5) we have:

$$u = 0 \quad \text{on } \Gamma, \tag{1.17}$$

which is the Dirichlet boundary condition. For the case of the TM radiation, let us assume that u represents the z-component of the magnetic field, whose polarization is pointing out the plane of incidence (Fig.1.5 (b)). In this case, it can be shown that the z-component of the magnetic field must satisfy

$$H_z = \frac{-ik_y}{k^2 - k_x^2}\left(\nabla_t H_z\right), \tag{1.18}$$

where ∇_t is the tangential gradient, and k_x and k_y are the x and y components of the wavevector, $\mathbf{k}$. In addition, since $\hat{n} \cdot \mathbf{H} = 0$ (PEC condition), where $\hat{n}$ is a normal unitary vector (Fig. 1.5), we have:

$$\hat{n} \cdot \mathbf{H} = \hat{n} \cdot H_z \hat{z} = \frac{-ik_y}{k^2 - k_x^2} \left(\hat{n} \cdot \nabla_t H_z \right) = 0, \tag{1.19}$$

where $\hat{n} \cdot \nabla_t H_z =: \partial_n H_z$ is the normal derivative and

$$\partial_{\mathbf{n}} H_z = 0 \quad \text{on } \Gamma, \tag{1.20}$$

which is the Neumann boundary condition.

1.4.3. Scalar Equations for Electromagnetic Fields

Solving Maxwell's equations in their vectorial form can become cumbersome depending on the nature of the problem. For this reason, simplifications are made in order to handle fields in a more straightforward way through a scalar formulation. This assumption leads to the frequency domain Helmholtz equation.

In the general case, electromagnetic fields at a constant given time t, depend on the position x, y, and z. However, if we want to obtain the electric field propagating in a direction lying on an infinite (unbounded) $x-y$ plane and assume isotropic media, constant phase, then one can see that the electric field is constant on x and y. This defines the transverse electric (TE) polarization ($E_x = E_y = 0$) as shown in Fig. 1.5 (a). Alternatively, we can assume similar conditions for the magnetic field, which leads to the transverse magnetic (TM) polarization ($H_x = H_y = 0$) as shown in Fig. 1.5 (b). Solutions for arbitrary excitation can be expressed as a superposition of these two basis forms. With these simplifications, we can then write the problem in terms of a scalar equation—defined on the semi-infinite domain D, according to Fig. 1.5— given by Helmholtz equation for both TE and TM cases.

$$\Delta u + k^2 u = 0 \quad \text{in } D, \tag{1.21}$$

where u can represent either the z-component of the electric or magnetic field, whose polarization is pointing out of the plane of incidence—plane $x - y$ in Fig. 1.5.

1.4.4. Optics of Solids

Electromagnetic waves interact with matter, and this interaction can be used to design and engineer novel devices, such as phtovoltaic (PV) and thermophotovoltaic (TPV) cells, photodiodes, etc. Electromagnetic waves can propagate in vacuum, whose properties are given in terms of the permittivity (ε_0) and permeability (μ_0). When an electromagnetic wave penetrates into a media different than vacuum, the propagation characteristics change due to the constituent atoms, electrons, etc. present inside the media. Atoms and electrons can drastically alter the behavior of light inside a media, for example, by decreasing the phase velocity (Grant, 1969).

1.4.4.1. Propagation of Light in Dielectrics and Metals

In a non-conductive medium, electrons are bonded to the atoms present in that medium. In addition, electrons can be moved away from equilibrium, resulting in a polarization effect. This behavior can be describe as a harmonic oscillator model, for which it is possible to find resonances. The presence of these resonances translates to large variations of medium refraction index and high optical absorption for frequencies close to those resonances. In addition, it is well known that the index of refraction is given by $n = \sqrt{\varepsilon}$ where, in general, $\varepsilon \in \mathbb{C}$. Therefore, the general form of the refraction index is given by $\mathcal{N} = n + i\kappa$, where κ is the extinction coefficient. Moreover, due to the fact that not all electrons are identically bonded, the general description is given as a sum of several oscillators as

$$\mathcal{N}^2 = 1 + \frac{Ne^2}{m\varepsilon_0} \sum_{j=1}^{N} \frac{f_j}{\omega_j - \omega^2 - i\Gamma_j \omega}, \tag{1.22}$$

where f_j is the oscillator strength, Γ_j is the damping constant—related to the lifetime as $1/\Gamma_j$—and N the number of oscillators with frequency ω_j. For light propagation in conductive media, such as metals, one common model is the Lorentz–Drude model. This model plays a crucial role in the study of light-matter interaction in different fields such as polarizers (Nguyen-Huu et al., 2011) and nanophotonics simulations (Gallinet, Butet, & Martin, 2015). It is based on a spring-damper model, which represents the restoring forces due to charged ions when an external electromagnetic field is applied. The complex dielecric constant in this model is written as (Grant, 1969)

$$\varepsilon_r(\omega) = 1 - \frac{\Omega_p^2}{\omega(\omega - i\Gamma_0)} + \sum_{j=1}^{N} \frac{f_j \omega_p^2}{(\omega_j^2 + i\omega\Gamma_j)}, \tag{1.23}$$

where ω_p is the plasma frequency, and Ω_p is the plasma frequency associated with intraband transitions with oscillator f_0 and damping constant Γ_0. The first two terms on the right hand side of equation (1.23) represent the intraband effects or free electrons and it is known as the Drude model. On the other hand, the third term in (1.23), the sum of oscillators, represents the interband effects, known as bound electron effects (Rakic, Djurisic, Elazar, & Majewski, 1998).

1.4.4.2. Surface Plasmon Polaritons

Plasmons are collective oscillations of free electrons in a plasma. In particular, surface plasmons (SPs) are coherent electron oscillations that appear at the interface between a dielectric and a metal. When a SP is coupled with an incident photon, the resulting excitation is called a surface plasmon polariton (SPP). The resulting surface wave consists of both the charge motion in the metal as well as the evanescent electromagnetic wave in the dielectric or metal. The simplest geometry that sustains SPP is shown in Fig. 1.6 (a). If we consider the dielectric permittivity $\varepsilon_d \in \mathbb{R}^+$, for example air, then the conditions for the existence of these surface waves can be obtained by examining the dispersion relation:

$$k_x^2 = k_0^2 \frac{\varepsilon_d \varepsilon_m}{\varepsilon_d + \varepsilon_m}, \tag{1.24}$$

where k_x is the surface component of the wavevector and ε_d and ε_m are the (possibly complex) permittivities of the dielectric and the metal, respectively. Normal components of the wavevector are obtained by using $k_0^2 = k_z^2 + k_x^2$, where k_0 is the vacuum wavenumber. Then, for each media (d and m), we obtain:

$$k_{z,d}^2 = k_0^2 \frac{\varepsilon_d^2}{\varepsilon_d + \varepsilon_m}, \quad \text{and} \tag{1.25}$$

$$k_{z,m}^2 = k_0^2 \frac{\varepsilon_m^2}{\varepsilon_d + \varepsilon_m}. \tag{1.26}$$

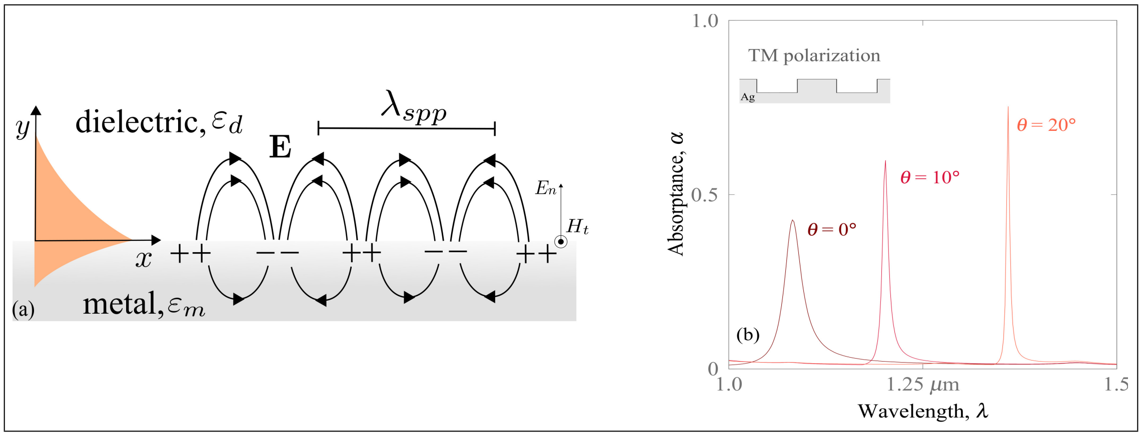

FIGURE 1.6. (a) Schematic diagram illustration of SPP excitation. The fields shown shown are for TM polarized light; E_n is the normal electric field and H_t is the tangential magnetic field, which coincides with the z axis. (b) Absorptance of a Ag square grating for different angles of incidence $\theta = 0°$, $10°$, and $20°$.)

With these relations, it is possible to find the constraints for the existence of surface waves. The first requirement is that $k_x \in \mathbb{R}^-$ and the second $k_{z,i}$ is imaginary for $i = m, d$. These two conditions can be simultaneously fulfilled if $\varepsilon_m \in \mathbb{R}$ and $\varepsilon_m < -\varepsilon_d$. In real metals, however, there will be attenuation of the waves along the surface, due to the imaginary part of the dielectric constant. Nevertheless, in most good conductors at optical frequencies $\text{Re}(\varepsilon_m) < 0$ and $|\text{Im}(\varepsilon_m)| \ll |\text{Re}(\varepsilon_m)|$. Therefore, surface waves at the metal-dielectric interface can exist. A qualitative illustration of these surface waves is shown in Fig. 1.6 (a). The externally applied (optical) electric field induces a polarization inside the material. This polarization contributes to the total electric field, generating a collective oscillation between the electron plasma and the electromagnetic field. The dispersion relation for SPPs lies below that of free space. Therefore, a way to couple light in free space to the SPPs is by augmenting the photons with additional momentum. In particular, gratings are an effective way to excite SPP, since they provide the required additional momentum due to their periodicity. For example, Fig. 1.6 (b) shows the absorptance of an Ag square grating. It can be noticed the existence of absorptance peaks for different angles of incidence ($0°$, $10°$, and $20°$) generated through the excitation of SPPs.

This coupling of the incident photons to surface waves enables one to engineer the optical properties of the surface, such as the reflectance and transmittance. This can be understood simply by considering power flow; if a surface wave is excited it carries energy along the surface with it. Thus the reflectance is reduced, producing a peak in transmittance. It is also possible enhance the absorptance above that of the native material properties, which can be valuable in applications such as solar cells. For simplicity, the examples shown here have been restricted to the case of a single interface between two materials. However, there are other ways to excite SPPs, including more complex multilayer structures, the Otto configuration ((Maier, 2008), p.42), or metal nanoparticles ((Toropov & Shubina, 2015), p.39).

1.4.5. Metal-Insulator-Metal Resonators (MIM)

Energy confinement can be used as an alternative option to excite SPPs, particularly in multilayer systems consisting of alternating metals and dielectrics. SPPs in such systems can be excited at each interface, when the thickness of two adjacent layers is smaller than the decay length of the interface mode. Furthermore, multilayers able to excite SPPs are also capable of energy localization below the diffraction limit (Maier, 2008). In particular, MIM resonators have gained attention since they are able to couple internal and external SPPs, resulting in excitation of a magnetic polariton (MP) (Xuan & Zhang, 2014). These type of quasiparticles represent a strong coupling between a magnetic resonance inside the structure and an external electromagnetic field (Zhao, 2016). For readers interested in further details, we refer to (Maier, 2008; Enoch & Bonod, 2012) and references therein.

1.5. Grating Equation, Diffraction Modes, and Efficiency

Gratings are periodic structures that can be periodic in one or two dimensions. For example, Fig. 1.7 shows a sinusoidal—also called holographic— grating with period Λ and height h, where an incident wave with angle of incidence θ_i impinges on the structure. Due to its periodicity, the reflected wave is diffracted in different modes $l = \ldots, 1, 0, -1, \ldots$

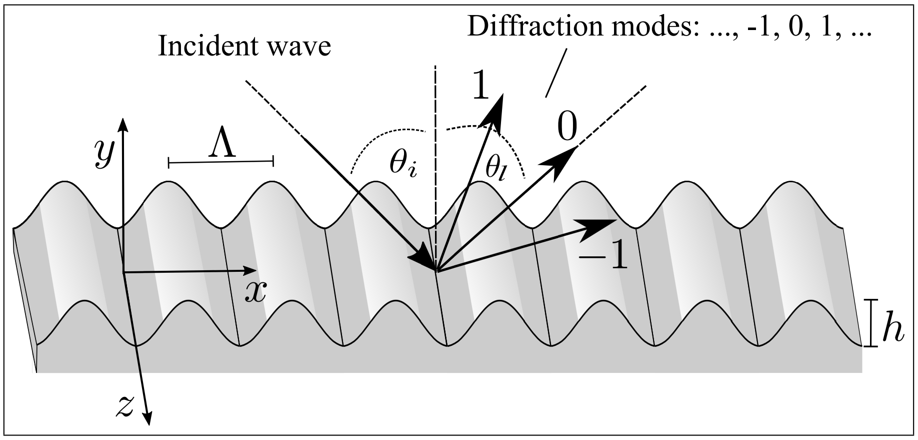

FIGURE 1.7. One-dimensional sinusoidal or holographic grating with period Λ and depth h. The shaded area depicts regions with refraction index, n_m; the region above the grating has a refractive index of n_i. An incident plane wave with angle of incidence θ_i is shown along with the angle three different modes of diffraction $l = -1, 0$, and 1.

with their respective angle of diffraction, θ_l. The direction of the diffracted waves, l, are called modes.

When electromagnetic fields interact with periodic structures, they take on the periodicity of the host structure. Due to this periodicity, an incident wave can be expressed as the superposition of spatial harmonics. The directions of these harmonics—or modes—are described by the grating equation, which is the most fundamental equation for the study of gratings:

$$k_{x,l} = k_{x,i} - lK_x \tag{1.27}$$

Equation 1.27 is also known as the phase matching condition, because it captures the requirement that the tangential component of the wavevector, k_x , must be continuous. Here, $k_{x,l}$ is the tangential component of the wavevector for a certain diffracted mode (l) and $k_{x,i}$ is the tangential component of wavector for the incident medium (i). In addition, $K_x = 2\pi/\Lambda$ is the x-component of the wavevector of the grating and $l \in \mathbb{Z}$. Equation 1.27 can be recast in a more useful form, given in terms of the incident angle, θ_i , and the wavelength, λ (Fig. 1.7). Thus, the angles of the diffracted modes, θ_l (their directions) are related to the incident wavelength and the grating period by:

$$n_j \sin(\theta_l) = n_i \sin(\theta_i) - l\frac{\lambda}{\Lambda}. \tag{1.28}$$

Here n_i is the index of refraction of the incident medium and n_j for $j = i, m$ is the index of refraction of the incident medium (i) or the grating material (m) as shown in Fig. 1.7. This equation represents one of the fundamental ways to study gratings and their fundamental properties such as Wood's anomalies (Wood, 1902). There are two kinds of these anomalies. The first kind, explained by Lord Rayleigh (Rayleigh, 1907), occurs at the wavelengths where diffracted orders appear or disappear. On the other hand, the second kind of anomaly—produced only for the transverse magnetic (TM, also called p) polarization—are the SPP described above. The explanation of SPPs was given by Fano (Fano, 1941). SPPs are excited in metallic gratings due to the momentum conservation between the incident light, the SPP, and the grating periodicity.

Efficiency is an important consideration for any engineered system. For a grating, the absolute efficiency is defined as the percentage of the incident monochromatic radiation on the grating that is diffracted into the desired order/mode. It is determined by both the grating's cross sectional profile (i.e. the shape of the grooves) and the grating's periodicity (Thorlabs, 2017). One configuration that is particularly important since it corresponds to the maximum grating efficiency is the Littrow configuration (Erwin G. Loewen & Popov, 1997). In this configuration, the reflected mode with $l = 1$ (Eq. (**??**)) is parallel to the incident wave vector. As a result, the grating acts as a spectrally-selective mirror. The grating equation gives the condition for the Littrow configuration by setting $\theta_i = \theta_l$, which yields:

$$n_i \sin(\theta_i) = \frac{\lambda}{\Lambda}. \tag{1.29}$$

1.6. Numerical Methods for Scattering Problems

As a consequence of the importance of scattering problems for science and technology, a range of numerical methods have been developed to calculate the scattered electromagnetic fields; the finite differences in time domain (FDTD), the finite element method (FEM), the method of moments (MoM), and the rigorous coupled wave analysis (RCWA) are the most popular. In this section, MoM, FEM, and RCWA—the frequency-domain approaches—are briefly discussed, since these methods are used as the basis for the work reported here. In the case of FDTD, interested readers are referred to (Jin, 2010; Kahnert, 2003; Gallinet et al., 2015) and references therein. Figure 1.8, shows the general description of the electromagnetic scattering problem. In this case D also represents an infinite domain and $\Gamma := \partial D$ represents the boundary of the illuminated (scattering) object. Further, D^c represents the complement of the domain D, which in this case stands for the domain inside the object. The fields $\mathbf{E}^i$ and $\mathbf{H}^i$ represent the incident electromagnetic waves and $\mathbf{E}^s$ and $\mathbf{H}^s$ the scattered ones. In addition, $\hat{n}$ is a unitary vector normal to the surface Γ and ε and μ are the material properties.

1.6.1. Finite Element Method (FEM)

The finite element method (FEM) is used to find approximate solutions to both ordinary and partial differential equations. It is based on a weak form of the differential equation, where the solution is approximated by a set of functions using, for example, the Galerkin method (see appendix A). The FEM requires the discretization of the entire space, for instance, the entire volume of a waveguide. Even though this is helpful and intuitive in some applications, this requirement can impose some limitations for unbounded problems such as electromagnetic or acoustic scattering. Scattering problems require infinite domains; therefore, some tricks, such as absorbing boundary conditions (ABC), perfectly matched layers (PML) (Jin, 2010), or FEM-BEM coupling (Johnson & Nedelec, 1980) are necessary. Another important impact that arises from the need to consider a mesh over the entire domain is the large number of degrees of freedom (DOF) that this entails. This implies a large associated linear system. Even though the number of DOF can be large, the

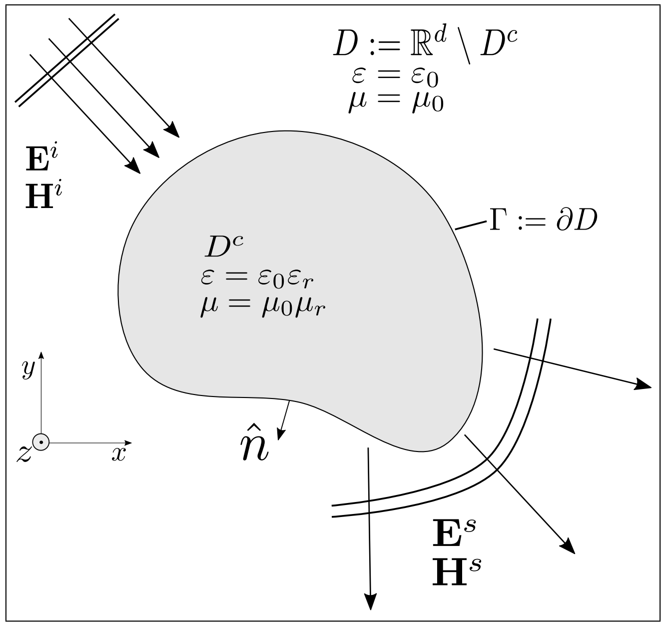

FIGURE 1.8. Description of the electromagnetic scattering problem. D is the unbounded domain in d-dimensions ($d = 1, 2, 3$), ε and μ are the permittivity and permeability, respectively, where the subscript 0 stands for vacuum and r for relative. The domain D^c is the complement of D, which represents the domain inside the scattering object, whose surface is defined by Γ with a normal unitary vector $\hat{n}$. Finally, $\mathbf{E}$ and $\mathbf{H}$ are the electric and magnetic fields, respectively, where the superscripts i and s stand for incident and scattered field, respectively.

associated matrix is sparse because typically elements only interact with their neighbors. This sparsity makes it easier to solve.

To show how the FEM works, let us consider Helmholtz equation in 1D (1.21) subject to Dirichlet boundary conditions (1.17). We can choose a set of basis functions to approximate the electric field as

$$u(\mathbf{r}) \approx u_M(\mathbf{r}) = \sum_{i=1}^{M} c_i \varphi_i(\mathbf{r}) \tag{1.30}$$

where $\mathbf{r}$ is the position vector and φ_i, $i = 1, 2, \ldots, M$ are basis functions. Part of the versatility of the FEM, and the mesh-based approximation methods in general is the variety of basis functions that can be adopted to approximate the solution with different accuracies and computational performance. The discretization or the basis functions considered to approximate the electromagnetic fields can take different forms (Jin, 2003; Sheng & Song, 2012; Johnson, 1987). Using Green's first identity (Appendix B), we can obtain a linear system given by:

$$\sum_{i=1}^{N} c_i \Big(\langle \nabla \varphi_i(\mathbf{r}), \nabla \varphi_j(\mathbf{r}') \rangle + k^2 \langle \varphi_i, \varphi_j \rangle \Big) = \int_\Gamma f \varphi_j d\Gamma, \quad j = 1, 2, \ldots, N. \tag{1.31}$$

where the right hand side, in general, depends on the boundary conditions and the characteristics of the functions φ. This system allows us to calculate coefficients c_i, which approximate the field u.

1.6.2. Method of Moments (MoM)

The method of moments—also called boundary elements method (BEM)—is based on the field representation in terms of two integral potentials called *single layer* (SL) and *double layer* (DL). In this thesis, we are considering scalar field problems, which means that representation of a field u in terms of those potentials in the domain D (shown in Fig. 1.8) is given by:

$$u(\mathbf{r}) = (\mathsf{SL}\partial_\mathbf{n} u)(\mathbf{r}) + (\mathsf{DL}u)(\mathbf{r}), \quad \forall\, \mathbf{r} \in D. \tag{1.32}$$

In its expanded form, the last equation can be written in terms of the derivatives of both the Green's function and the field u as follows (Buffa & Hiptmair, 2003; Sauter & Schwab, 2011)

$$u(\mathbf{r}) = \int_\Gamma G(\mathbf{r}, \mathbf{r}') \partial_\mathbf{n} u(\mathbf{r}') d\Gamma(\mathbf{r}') + \int_\Gamma \partial_{\mathbf{n}'} G(\mathbf{r}, \mathbf{r}') u(\mathbf{r}') d\Gamma(\mathbf{r}'), \quad \mathbf{r} \in D \text{ and } \mathbf{r}' \in \Gamma. \tag{1.33}$$

The normal derivative of u in the first term in the right-hand side is evaluated on the boundary Γ (usually known as the Neumann trace). On the other hand, the value of the field u in the second term of the right hand side is also evaluated on the boundary Γ (usually known as the Dirichlet trace). The formulation for the Dirichlet problem (as well as the Neumann problem) can be written in terms of both the SL and the DL potentials. In this section, and considering the context required for the next chapters, we intend to give a brief explanation of the formulation based on the SL potentials. For interested readers, others formulations can be found in (Steinbach, 2008; Sauter & Schwab, 2011) and references therein.

For the scalar Helmholtz's equation (Eq. (1.21)), the scattered electric field polarized in the TE direction can be represented as (Sauter & Schwab, 2011)

$$u^s(x) = (\mathsf{SL}\partial_{\mathbf{n}} u)(x) = \int_\Gamma G(x,x')\partial_{\mathbf{n}} u(x') d\Gamma(x'), \quad x' \in \Gamma \text{ and } x \in D. \tag{1.34}$$

Here G is the Green's function associated with the problem, $\partial_{\mathbf{n}} u(x)$ is the normal derivative of the field u, which in this case is related to the current density through $J_s = i\partial_{\mathbf{n}} u$. Based on this formulation, and using the Galerkin method (Appendix A), it is possible to write down a linear system to find the coefficients c_i that approximate the surface current density, such that

$$J_s(\mathbf{r}) \approx \sum_{i=1}^{N} c_i \varphi_i(\mathbf{r}), \tag{1.35}$$

where φ_i, with $i = 1, 2, \ldots, N$ is an orthogonal basis set of functions. Therefore,

$$\sum_{i=1}^{N} c_i \langle \mathsf{SL}\varphi_i(\mathbf{r}), \varphi_j(\mathbf{r}')\rangle = \langle u^i(\mathbf{r}), \varphi_j(\mathbf{r}')\rangle, \quad j = 1, 2, \ldots, N, \tag{1.36}$$

where $\langle \cdot, \cdot \rangle$ represents the inner product. As can be noticed from the integral formulations given above, the Green's functions are the keystone of these representations. In the case of Helmholtz's equation in free space for a 2D problem, the Green's function is given in terms of Hankel functions (Jin, 2010) by

$$G(\mathbf{r}, \mathbf{r}') = \frac{i}{4} H_0^{(1)}(k|\mathbf{r} - \mathbf{r}'|), \tag{1.37}$$

where $H_0^{(1)}$ are the zero-th order Hankel functions of the first kind. The Green's function for a one-dimensional periodic array can be easily derived (Tsang, Kong, Ding, & Ao, 2001) by using the Floquet-Bloch condition $u(x + \Lambda) = e^{ik_x\Lambda} u(x)$, which allows us to write the Green's function as a sum of modes

$$G^p(\mathbf{r}, \mathbf{r}') = \frac{i}{4} \sum_{m=-\infty}^{\infty} e^{ik_x m\Lambda} H_0^{(1)}(k\sqrt{(x - x' - m\Lambda)^2 - (y - y')^2}) \tag{1.38}$$

This form of the Green's function involves an infinite sum over the Floquet modes and, in general, exhibits poor convergence or contains singularities. For example, when $\theta > 0$, this series has a non-decaying component, which translates to poor convergence. Moreover, due to the Hankel function it possesses a logarithmic singularity when $\mathbf{r} = 0$, i.e., when the observer is in the same location as source (on-plane condition). To deal with slow convergence, spectral forms of the Green's function have been considered (Petit, 1980):

$$G^p(\mathbf{r}, \mathbf{r}') = \frac{i}{2\Lambda} \sum_m \frac{e^{ik_{x,m}(x-x')+ik_{y,m}|y-y'|}}{k_{y,m}}, \tag{1.39}$$

where $k_{x,m}$ and $k_{y,m}$ are wavevector components for a one-dimensional periodic array. In this case, the situation is different; the Green's function possesses singularities for each $k_{y,m} = 0$, which occurs for the grazing anlgle, $\theta = \pi/2$ since $k_{y,m} = \sqrt{k - k_{x,m}}$. In addition, if $y = y'$ the summation converges slowly and a large value of m is required to obtain convergence. For this reason, several techniques devoted to improve the convergence and deal with singularities have been investigated (Bruno & Haslam, 2009; Bruno, Lyon, Pérez-Arancibia, & Turc, 2016; Bruno, Shipman, Turc, & Venakides, n.d.; Chandler-Wilde & Graham, 2009; Desanto, Erdmann, Hereman, & Misra, 1998).

1.6.3. Rigorous Coupled Wave Analysis

For certain classes of problems, more specialized approaches can be beneficial. To evaluate scattering from periodic structures, rigorous coupled wave analysis (RCWA) is especially well suited (Moharam & Gaylord, 1981; Li, 1996; Chateau & Hugonin, 1994; J. & G., n.d.). The RCWA is a method that gives an exact solution of Maxwell's equations for flat surfaces; for more complex geometries its accuracy depends on the number of diffraction orders in the expansion of the fields.

Let us consider a time harmonic ($e^{i\omega t}$) and linearly polarized incident wave with electric field $\mathbf{E}^i$ and wavevector $\mathbf{k}^i$ (Fig. 1.9), whose components are given by:

$$\begin{aligned}
k_x^i &= k_0 n_1 \sin(\theta)\sin(\phi) \\
k_y^i &= k_0 n_1 \cos(\theta) \\
k_z^i &= k_0 n_1 \sin(\theta)\cos(\phi),
\end{aligned}$$

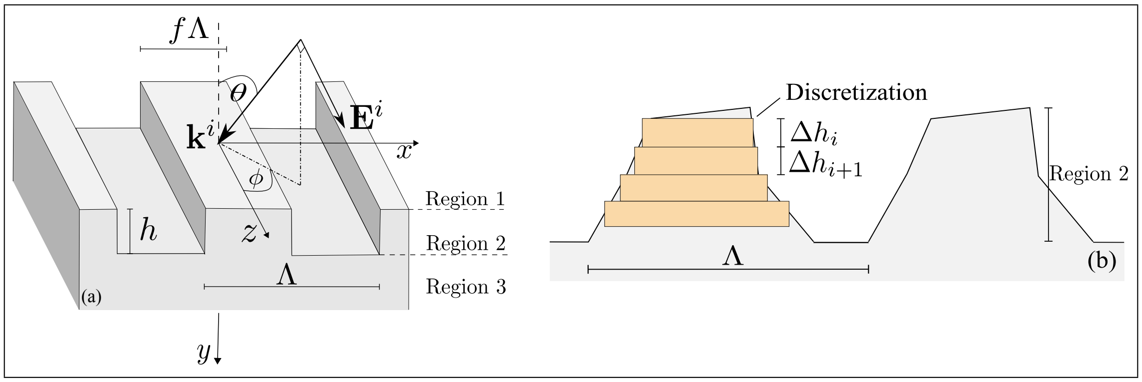

FIGURE 1.9. Representation of the rigorous coupled wave analysis (RCWA) method. (a) The domain is separated into three different regions (the incident electric field ($\mathbf{E}^i$) with wavevector $\mathbf{k}^i$ are also illustrated). (b) Discretization of complex geometries using rectangles

where n_j with $j = 1, 2, 3$ is the refractive index of each region (1, 2, and 3, respectively) and it is related to the permittivity through $n_i = \sqrt{\varepsilon_i}$ for $\mu_i = 1$. In region 1 (Fig.1.9), the electric field is given, as usual, as a sum of the incident and reflected fields by

$$\mathbf{E}_1(\mathbf{r}) = \mathbf{E}^i e^{i\mathbf{k}^i\cdot\mathbf{r}} + \sum_{m,n} \mathbf{E}^r_{mn} e^{i(k_{x,m}x + k_{z,n}z - k^r_{y,mn}y)}, \tag{1.40}$$

where $k_{x,m} = k^i_x + 2\pi m/\Lambda_x$ and $k_{z,m} = k^i_z + 2\pi m/\Lambda_y$. The z components of the wave vectors are determined by $k^r_{y,mn} = \sqrt{k_1^2 - k^2_{x,m} - k^2_{z,n}}$, which is real when $\varepsilon_1 k_{0^2} \geq k^2_{x,m} + k^2_{z,n}$ and imaginary if $k_0^2 < k^2_{x,m} + k^2_{z,n}$. In region 2, the electromagnetic fields are represented as Fourier series, which depends on the period of the structure. In the general case, the structure can be periodic in x and y, but in the cases considered here, structures are only periodic in x as shown in Fig. 1.9 (a). To simulate more complicated structures, it is possible to discretize the region 2 in layers as is shown in Fig. 1.9 (b). In this case, the permittivity tensor takes the form:

$$\bar{\varepsilon}_i := \begin{pmatrix} \varepsilon_{i,x} & 0 & 0 \\ 0 & \varepsilon_{i,y} & 0 \\ 0 & 0 & \varepsilon_{i,z} \end{pmatrix} \tag{1.41}$$

Then, the electric and magnetic fields can be written as:

$$\mathbf{E}_2(\mathbf{r}) = \sum_{m,n} \psi^e_{m,n}(y) e^{i(k_{x,m}x + k_{z,n}z)}, \tag{1.42}$$

$$\mathbf{H}_2(\mathbf{r}) = i\sqrt{\frac{\varepsilon_0}{\mu_0}} \sum_{m,n} \psi^h_{m,n}(y) e^{i(k_{x,m}x + k_{z,n}z)}, \tag{1.43}$$

where the fields $\psi^e_{m,n}$ and $\psi^h_{m,n}$ can be related to the permittivity tensor (Eq. 1.41) using Maxwell's equations (1.4) and (1.3). It is also possible to write an equation for the region 3

$$\mathbf{E}_3(\mathbf{r}) = \sum_{m,n} \mathbf{E}^t e^{i(k_{x,m}x + k_{z,n}z + k^t_{y,m,n}y)}, \tag{1.44}$$

where k^t_z is the z-component of the transmitted wavevector. This equation depends in general on polarization and the transmitted propagating waves. Finally, the coefficients given in the representations of the electromagnetic fields in each region can be determined applying the boundary conditions. For a detailed description of the RCWA method and its matrix formulation we refer to (Zhao, 2016; Soifer, 2017) and references therein.

1.7. Numerical Methods for Uncertainty Quantification (UQ)

All mathematical models and numerical simulations of the types considered here can be used to represent phenomena in the real world. In general, to build a mathematical and, consequently, a computational model, it is necessary to make simplifications and idealizations. However, this can lead to imprecision in the model predictions. For instance, in an engineering design and analysis context, one typically assumes that the relevant physics is known and that the boundary conditions or other constraints of the problem are known in an exact or analytical way. In reality, however, these input parameters are often not perfectly known. Uncertainty quantification (UQ) gives us tools to deal with these sorts of uncertainties, thereby allowing us to obtain a better model description of the world. A succinct description of UQ is given by the U.S. Department of Energy (Higdon et al., 2006).

UQ studies all sources of error and uncertainty, including the following: systematic and *stochastic measurement error; ignorance; limitations of theoretical models; limitations of numerical representations of those models; limitations of the accuracy and reliability of computations, approximations, and algorithms; and human error. A more precise definition is UQ is the end-to-end study of the reliability of scientific inferences.*

A good introduction is also given in (Sullivan, 2015) and references therein. One especially important application of UQ in the area of numerical simulations is to understand and quantify the impact of variations or imprecision in the structure (i.e. the geometry) or material properties within a system being simulated. Mathematically, this is equivalent to the input parameters of the system being imperfectly known. An increasingly popular approach is to model such parameters as random variables (Harbrecht, 2010, 2014). For this reason, UQ is taking an increasingly important role in simulations, since it allows one to make better predictions, perform more sophisticated analyses, and ultimately arrive at better designs. In Fig. 1.10 a schematic example is presented. Experimental results (solid triangles), predictions by numerical simulations not including UQ methods (red continuous line), and UQ predictions (standard deviation in orange continuous lines and the mean in dashed lines) are put together for comparison. It can be noticed that the experimental values lie inside the predicted uncertainty range (standard deviation) and that the mean predicted by the UQ model is not necessarily equal to either the simulation results or the experiments.

1.7.1. Methods for UQ

Uncertainty quantification methods have been increasing popularity; therefore, several methods and modifications to improve their performance, i.e., convergence, accuracy, etc. have been studied and proposed. Here the two considered approaches of this work, Monte Carlo and deterministic approaches, are briefly explained. In addition, since the implementation of a deterministic approach requires some non-conventional mathematical tools, a brief introduction on sparse grids as well as the the shape derivative are given in Sections 1.7.1.3 and 1.7.1.4, respectively.

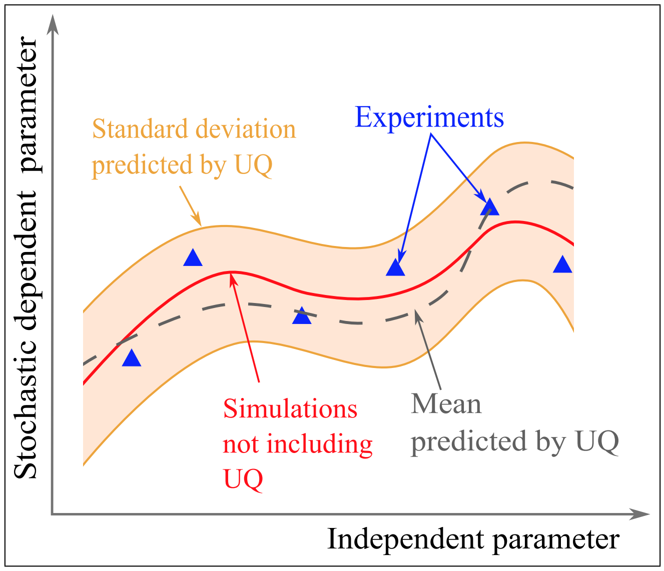

FIGURE 1.10. Cartoon illustration of uncertainty quantification (UQ). It can be noticed that the results of simulations, experiments and UQ predictions are not necessarily equal. UQ can predict a range or bounds on the expected results through, for example, the standard deviation.

1.7.1.1. Monte-Carlo method

The Monte Carlo (MC) method is tremendously popular and it has been applied to practically every area of research in science and engineering, for example, electromagnetism (Matthew N O Sadiku, 2009), fluid mechanics (Han et al., 2012), MOSFET device simulations (Ezaki, Werner, & Hane, 2003), just to name a few. This method revolves around the idea of generating a vast number of randomly generated samples to then calculate the statistical moments, i.e., mean, variance, skewness, etc.

The most general way of describing the MC approximation is by considering a function $g(y) : \mathbb{R}^d \to \mathbb{R}^d$, where y is characterized by a probability density. The function g is a quantity of interest that can be, for example, a solution from FEM or MoM. Once we have generated a set of samples $y^{(i)},\ i = 1, 2, , \ldots, M$, it is straightforward to approximate the mean by:

$$I \approx I_M = \frac{1}{M} \sum_{j=1}^{M} g(y^{(j)}), \tag{1.45}$$

where I is the exact value of the mean and I_M is an approximation using M randomly generated samples. It is also easy to prove that $\mathbb{E}[I_M] = I$ (an unbiased estimator). In the case of variance, we have:

$$\text{Var}[I_M] = \frac{1}{M^2} \sum_{j=1}^{M} \mathbb{E}[g(y^{(j)}) - I^2]. \tag{1.46}$$

The MC method is computationally expensive due to the fact that its convergence is slow. Moreover, the convergence is even slower when the variance of the problem is high. However, one of the advantages of the MC method is that the convergence does not depend on the dimensionality of the problem. To improve the convergence of the MC methods, some approaches based on variance reduction have been investigated. For example, stratified sampling (Keramat & Kielbasa, 1997; Owen, 2013), latin hypercube (Stein, 1987), and quasi MC (L'Ecuyer & Lemieux, 2005).

1.7.1.2. Deterministic approaches

As an alternative to the MC methods, some deterministic approaches have been proposed. In particular, approaches that are related to this work are the cases of random surface perturbations, where Poisson's equation with Dirichlet boundary conditions (Harbrecht, Schwab, & Schneider, 2006; Dambrine, Greff, Harbrecht, & Puig, 2014), Robin and Neumann boundary conditions (Harbrecht, 2014), and Maxwell's equations (Jerez-Hanckes & Schwab, 2016) equations have been investigated. Knowing the stochastic source, one can write down a set of tensorized differential equations to approximate the different statistical moments, such as mean and variance, with no generation of random samples as is the case of MC methods. For example, let us consider the following operator equation:

$$\mathcal{A}g = f, \tag{1.47}$$

where $\mathcal{A}$ is a linear bounded operator defined over a Hilbert space V such that $\mathcal{A} : V \to V'$, where V' is its dual. We are interested in computing the statistical moments of a randomly dependent solution g. To define them, we need the q-fold tensor product of a Hilbert space

X, defined as:

$$X^{(q)} = \underbrace{X \otimes X \ldots \otimes X}_{q-\text{times}} \tag{1.48}$$

Therefore, the q-moment is defined as:

$$\mathcal{M}^{(q)} g = \mathbb{E}[\underbrace{g \otimes g \ldots \otimes g}_{q-\text{times}}] = \int_{\omega \in \Omega} \underbrace{g(\omega) \otimes g(\omega) \ldots \otimes g(\omega)}_{q-\text{times}} dP(\omega) \tag{1.49}$$

If we have the tensor product of the operator $\mathcal{A}$, which maps $\mathcal{A}^{(q)} : V^{(q)} \to (V')^{(q)}$ we can write

$$\mathcal{A}^{(q)} g^{(q)} = f^{(q)}, \tag{1.50}$$

where $g^{(q)} = g \otimes \ldots \otimes g$ and $f^{(q)} \in L^1(V')^{(q)}$, which implies

$$\mathcal{A}^{(q)} \mathcal{M}^{(q)} g = \mathcal{M}^{(q)} f. \tag{1.51}$$

This equation provides a way to compute the moments of g in a deterministic way, avoiding the generation of random samples. Theorems about these results as well as their proofs can be found in (von Petersdorff, Schwab, von Petersdorff, & Schwab, 2006; Schwab & Gittelson, 2011). Since they are based on tensor products to find higher statistical moments, sparse tensor approximations are considered in order to deal with the curse of dimensionality.

1.7.1.3. Sparse Grids

Sparse grids are a special discretization technique which allow us to cope with the curse of dimensionality, i.e., the exponential dependence of conventional approaches on the dimension d (Gertsner & Griebel, 2008). They are based on hierarchical bases and a sparse tensor product construction. Sparse grids have been successfully implemented in FEM and BEM to solve different kinds of problems in different fields such as electromagnetism (Jerez-Hanckes & Schwab, 2016; Liu, Gao, & Hesthaven, 2011), turbulence models (Tran, Webster, & Zhang, 2016), dynamic models in economy (Johannes & Simon, n.d.) among others. The underlying idea of sparse grids was developed by Smolyak (Smolyak, 1963), who first implemented this technique for numerical integration. To give an idea on how sparse approximations work, let us start by considering a set hierarchical increment spaces W_l (Fig. 1.11)

$$W_l := \text{span}\{\phi_{l,j}, j \in \mathcal{I}_l\}, \tag{1.52}$$

where the index set $\mathcal{I}_l$ is defined as

$$\mathcal{I}_l := \{j \in \mathbb{N} : 1 \leq j \leq 2^l - 1, j \text{ odd}\}. \tag{1.53}$$

These increment spaces satisfy the relations

$$V_l = \bigoplus_{j \leq l} W_j. \tag{1.54}$$

Therefore, given an approximation space of resolution l, the spaces W_l are the complement of the next resolution level $l+1$, which can be expressed as

$$V_{l+1} = V_l \oplus W_l. \tag{1.55}$$

Figure 1.11 (a) shows a representation of the approximation spaces for $l = 3$. It is shown how the W_j spaces are contained in V_l. When computing tensor products, if all possible combinations of the basis functions $\varphi_{l,j}$ are considered, we obtain a dense approximation. This kind of approximation suffers from the curse of dimensionality since the number of degrees of freedom increases exponentially as the dimension, d, increases. However, it is possible to choose a number of basis functions of V_l, for example as shown in Fig. 1.11 (b), where combinations of basis functions with small support or contribution are not included. Then a sparse approximation of level l can be defined as:

$$\hat{V}_l := \bigoplus_{\mathbf{l}_1 \leq l+d-1} W_{\mathbf{l}}, \tag{1.56}$$

where $|\mathbf{l}|_1 := \sum_{t=1}^{d} l_t$ with a multi-index $\mathbf{l} := (l_1, l_2, \ldots, l_d) \in \mathbb{N}^d$ and direction $t = 1, 2, \ldots, d$. On the other hand, a full or dense approximation of level l can be expressed as

$$V_l := \bigoplus_{\mathbf{l}_\infty \leq l} W_{\mathbf{l}}, \tag{1.57}$$

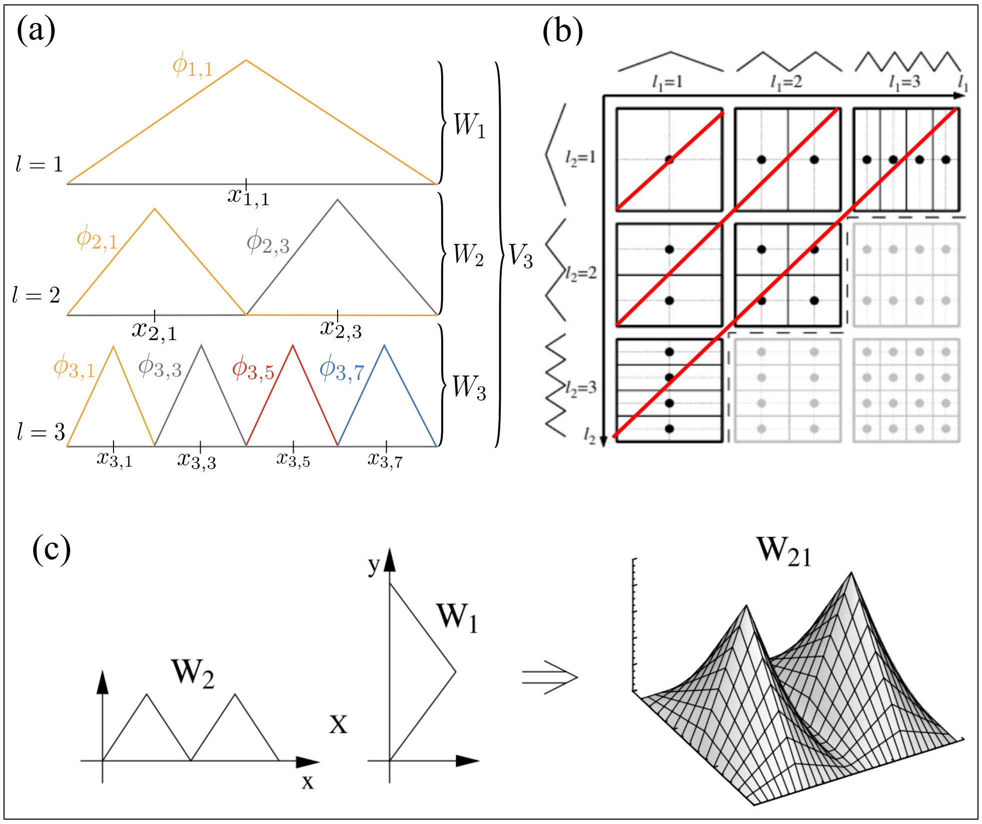

FIGURE 1.11. Representations of sparse grids. (a) shows three different levels for spaces W_1, W_2, and W_3 as well as V_3 as well as their elements $\phi_{j,l}$. (b), shows the construction of a sparse grid for two-dimensional subspaces from a dense approximation by choosing W_j spaces (black). The dense grid is formed considering the gray boxes. Finally, (c) shows the tensor product between two elements W_1 and W_2 from (Bungartz & Griebel, 2004).

where $|\mathbf{l}|_\infty := \max_{1 \leq t \leq d} l_t$. Sparse approximations consider only a subset of functions of V_l (Fig. 1.11). The advantage of sparse grids is that it allows us to construct approximation spaces where the same number of points of a given grid leads to a higher order of accuracy. For details on proofs and convergence we refer to the reader to (Bungartz & Griebel, 2004) and references therein.

1.7.1.4. Shape Derivative

In this work, we intended to study geometric variations of a domain D into a perturbed domain D_ϵ due to stochastic perturbations. For this purpose, the definition of a different kind of derivative, able to quantify those changes, is necessary and where the so-called shape derivative is well suited. A rigorous definition and study of the shape derivative can be found in (Sokolowski & Zolesio, 1992) and example applications in (Markus Kollmann, 2008). The shape derivative can be defined as a pointwise limit

$$\dot{u} := \lim_{\epsilon \to 0} \frac{u_\epsilon - u}{\epsilon}, \tag{1.58}$$

where u is a quantity in a reference or unperturbed domain and u_ϵ is the same quantity, but obtained from a the perturbed domain, D_ϵ. It can be shown that the shape derivative can be applied to solve boundary value problems (BVP) for perturbed domains in the case of Dirichlet and Neumann boundary conditions (Harbrecht, 2014; Harbrecht et al., 2006). In general to find the shape derivative, it is necessary to solve an associated BVP with a special set of boundary conditions, which can be derived by defining and taking the derivative of an associated functional.

1.8. Quantifying Small Perturbations

In Chapter 2, we solve the electromagnetic scattered field from a PEC grating with small random surface perturbations by solving the Helmholtz equation with a Galerkin method (See Appendix A) and using Haar's wavelets as the hierarchical bases (Steinbach, 2008). To quantify small perturbations, we solve the adjunct problem of the shape derivative with a prescribed Dirichlet boundary condition. This boundary condition can be found by the derivation of a functional (also called Eulerian derivative) related to the weak form of the Helmholtz's equation. It can be shown that the same type of boundary condition can be found using a Taylor expansion as is customary in the small perturbation methods (SPM). For readers interested in further details as well as derivations for other BVP, such as the TM (or Neumann) problem, etc., we refer to (Potthast, 1996b, 1996a; Hiptmair & Li, 2013, 2017) and references therein. On the other hand, for a more detailed description about the SPM, we refer to (Tsang et al., 2001; Shin & Kong, 1984; Kong, 1986).

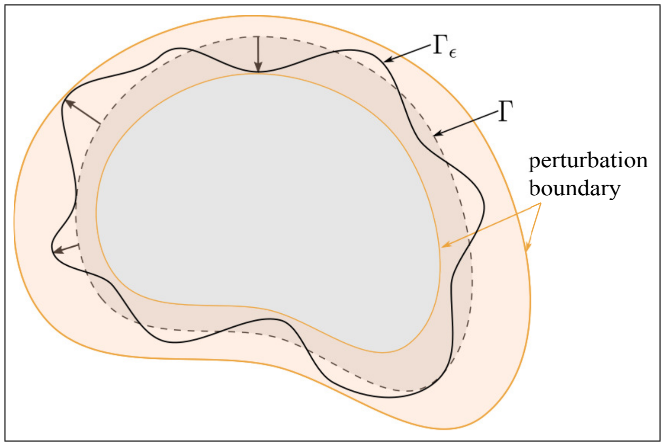

FIGURE 1.12. Representations of of a perturbed surface, where the perturbations are given as a function of the normal unitary vector to the surface. Γ and Γ_ϵ represent the unperturbed and perturbed domains, respectively.

1.8.1. Shape Derivative for Dirichlet BVP

Let us consider the Helmholtz equation subject to Dirichlet boundary conditions:

$$-\Delta u - k^2 u = f \quad \text{in } D \tag{1.59}$$

$$u(D) = z(\Gamma) \quad \text{on } \Gamma \tag{1.60}$$

First, let us find the associated problem for the shape derivative by multiplying 1.59 by a test function $\varphi \in C^\infty(D)$ such that $\partial_{\mathbf{n}}\varphi = 0$; applying the Green theorem (Appendix B) results in

$$\int_D (\nabla u \cdot \nabla \phi - k^2 u\phi) dD = \int_D f\phi dD. \tag{1.61}$$

Let us call the terms on the left and right hand sides as J_l and J_r, with shape derivatives dJ_l and dJ_r, respectively. We can obtain these derivatives by using the formulas in (Sokolowski & Zolesio, 1992)

$$dJ_l = \int_D ([\nabla u \dot{\cdot} \nabla\varphi] - k^2[u\dot{\varphi}])dD + \int_\Gamma (\nabla u \cdot \nabla\varphi - k^2 u\varphi)\langle \mathbf{U}, \hat{n}\rangle d\Gamma. \tag{1.62}$$

Note that the second term on the right hand side is a boundary term; therefore, its derivative is different from one over the domain. This boundary term possesses an inner product between a the unitary normal vector to the surface and the vector field $\mathbf{U} := \epsilon\kappa\hat{n}$ given in terms of the perturbation, ϵ and a smooth—and in general stochastic— function κ. In addition, $\dot{\varphi}(\Gamma, \mathbf{U}) = \partial_{\mathbf{n}} \mathbf{U} \cdot \hat{n}$. Equation (1.62) can be simplified

$$dJ_l = \int_D \nabla \dot{u} \cdot \nabla \varphi - k^2 \dot{u} \varphi dD + \int_\Gamma (\nabla u \cdot \nabla \varphi - k^2 u \varphi) \langle \mathbf{U}, \hat{n} \rangle d\Gamma \qquad (1.63)$$

Following the same procedure for the right hand side term, and comparing the volumetric and boundary terms, we get

$$\int_D \nabla \dot{u} \cdot \nabla \varphi - k^2 \dot{u} \varphi dD \;=\; \int_D f' \varphi dD, \qquad (1.64)$$

$$\int_\Gamma (\nabla u \cdot \nabla \varphi - k^2 u \varphi) \langle \mathbf{U}, \hat{n} \rangle d\Gamma \;=\; \int_\Gamma f \varphi \langle \mathbf{U}, \hat{n} \rangle d\Gamma. \qquad (1.65)$$

Following the same procedure used above for the boundary condition (1.60), we obtain

$$\int_\Gamma \dot{u} \varphi d\Gamma + \int_\Gamma (\partial_{\mathbf{n}}(u\varphi) + \varkappa u \varphi) \langle \mathbf{U}, \hat{n} \rangle d\Gamma = \int_\Gamma \dot{z} \varphi + \varkappa z \varphi \langle \mathbf{U}, \hat{n} \rangle d\Gamma. \qquad (1.66)$$

For the last step, it is necessary to note that the shape derivative is being applied over a function defined on a boundary and, therefore, a new term called the mean curvature $\varkappa := \mathrm{div}_\Gamma \hat{n}$ appears in the derivations of the functionals. Then, applying the boundary conditions (1.60), we get

$$\int_\Gamma \dot{u} \varphi + \partial_{\mathbf{n}} u \varphi \langle \mathbf{U}, \hat{n} \rangle d\Gamma = \partial \dot{z} \varphi d\Gamma. \qquad (1.67)$$

which in its strong form becomes:

$$\dot{u} = \dot{z} - \partial_{\mathbf{n}} u \langle \mathbf{U}, \hat{n} \rangle, \qquad (1.68)$$

which is the general form of the boundary condition for the shape derivative. This form is valid for both Poisson and Helmholtz equations as well as flat and periodic surfaces. Equation (1.68) can be expressed in terms of the electric field and the surface perturbation, assuming that $z = f = 0$ and that the total field is given in terms of the incident and scattered fields as $u = u^i + u^s$; therefore,

$$\dot{u}^s(\mathbf{r}) = -\epsilon \kappa(\mathbf{r}) \partial_{\mathbf{n}} (u^i + u^s)(\mathbf{r}) \quad \mathbf{r} \in \Gamma. \qquad (1.69)$$

1.8.2. Small Perturbation Method (SPM)

As we mentioned above, by using a Taylor expansion we can derive the first order correction to the scattered field from a perturbed surface. To do so, let us consider the Taylor expansion for the total field, $u = u^i + u^s$, around the surface Γ with normal perturbations with respect to the domain given by $\mathbf{U}$:

$$u(\mathbf{r} + U(\mathbf{r})) = u(\mathbf{r}) + \mathbf{U}(\mathbf{r})\nabla u(\mathbf{r}) + \mathcal{O}(h^2),\ \mathbf{r} \in \Gamma, \tag{1.70}$$

and the expansion of the scattered field, u^s, as:

$$u^s(\mathbf{r}) = u^s_{(0)}(\mathbf{r}) + \epsilon u^s_{(1)}(\mathbf{r}) + \epsilon^2 u^s_{(2)}(\mathbf{r}) + \cdots +,\ \mathbf{r} \in \Gamma, \tag{1.71}$$

where $u^s_{(0)}$ is the scattered field from the unperturbed domain and $u^s_{(i)}$ with $i = 1, 2, \ldots$ are the corrections to the field due to the perturbations. Taking equation (1.70) to first order and applying PEC boundary conditions on the perturbed surface, $\mathbf{r} + \mathbf{h}(\mathbf{r}, \omega)$, with $\mathbf{r} \in \Gamma$, yields

$$u(\mathbf{r}) \approx -\mathbf{U}(\mathbf{r})\nabla u(\mathbf{r}),\ \mathbf{r} \in \Gamma, \tag{1.72}$$

which can be written as:

$$u^i(\mathbf{r}) + u^s(\mathbf{r}) \approx -\mathbf{U}(\mathbf{r})\nabla(u^i + u^s)(\mathbf{r}),\ \mathbf{r} \in \Gamma. \tag{1.73}$$

Then, using (1.71) up to first order:

$$u^i(\mathbf{r}) + u^s_{(0)}(\mathbf{r}) + \epsilon u^s_{(1)}(\mathbf{r}) \approx -\mathbf{U}(\mathbf{r})\nabla(u^i + u^s)(\mathbf{r}),\ \mathbf{r} \in \Gamma \tag{1.74}$$

we conclude that

$$\epsilon u^s_{(1)}(\mathbf{r}) \approx -\mathbf{U}(\mathbf{r})\nabla(u^i + u^s)(\mathbf{r}),\ \mathbf{r} \in \Gamma, \tag{1.75}$$

which can be written as:

$$u^s_{(1)}(\mathbf{r}) \approx -\kappa(\mathbf{r})\mathbf{n}_0 \cdot \nabla(u^i + u^s)(\mathbf{r}),\ \mathbf{r} \in \Gamma. \tag{1.76}$$

Using the definition of the normal derivative $\partial_{\mathbf{n}} := \hat{n} \cdot \nabla$, equation (1.76) leads to the boundary condition (1.69). Therefore, the shape derivative as described above can be interpreted as a first order correction. The Taylor expansion and the shape derivative boundary condition are the keystones when quantifying small random perturbations by deterministic approaches as we will see in Chapter 2.

1.9. Summary of Contributions

By pursuing the research goals outlined previously, several new and original contributions have been obtained. Among them, we expect that the most significant are the development and demonstration of a reliable and fast numerical approach to quantify the impact of surface perturbations on gratings, and the exploration of new thermal emitter designs using *high-k* materials such as hafnia to improve spectral emittance performance.

1.9.1. Impact of Surface Perturbations on Grating Performance

(i) Implementation of the MoM for periodic structures using hierarchical bases to solve the Helmholtz's equation subject to perfect electric conductor boundary conditions

(ii) Quantification of small random surface perturbations through a fast deterministic approach based on sparse tensor approximations

(iii) Show the applicability of the proposed method through the calculation of the grating's diffraction efficiency

1.9.2. Gratings for Spectrally Selective Thermal Emitters for Thermophotovoltaics

(i) Provide paths to improve the thermal emittance by using easy to fabricate periodic structures by the excitation of different resonance phenomena to reach high thermal emittance with high melting point materials obtaining almost polarization insensitivity

(ii) Optimization of the tungsten grating with dielectric materials, reaching very high emittance with almost polarization insensitivity and weak dependence of the angle of incidence

1.10. Thesis Structure

The purpose of this thesis is to improve the design of TPV cells through numerical simulations. As mentioned, two research thrusts have been investigated. In following chapters, the main results as well as details will be given. In Chapter 2, we present the study the impact of surface random perturbations on electromagnetic scattering from perfectly reflecting gratings. We developed a method based on the shape Taylor expansion to quantify these perturbations and we successfully applied the approach to quantify the effect on the grating efficiency. In Chapter 3, an application of gratings to TPV energy conversion is studied. We used tungsten gratings with hafnia layers to improve the thermal emittance due to the excitation of surface plasmon polariton, magnetic polaritons, and cavity resonances. We show that by exciting these resonances, the emitter presents peaks of almost perfect emittance for both TE and TM polarizations. To complement the study on selective thermal emitters, in Chapter 4 we study the optimization of tungsten-hafnia gratings through a genetic algorithm. In this study, we compare the grating selective emitter with one based on a multilayer resonator, showing that in both cases it is possible to reach very high hemispherical thermal emittances with weak dependence of the angle of incidence. Finally, in Chapter 5, a review of the main results and conclusions is given as well as possible paths and guidelines for future research according to the results that have been obtained in the previous chapters.

2. QUANTIFYING THE IMPACT OF SURFACE RANDOM PERTURBATIONS ON REFLECTIVE GRATINGS[1]

2.1. Introduction

Gratings are ubiquitous in optical and electromagnetic systems due to their remarkable properties. For example, they can be used to excite surface plasmon polaritons (SPPs) or waveguide resonances (WR), which allow for the engineering of thermal emission in energy conversion devices such as thermophotovoltaic (TPV) cells (Y.-B. Chen & Zhang, 2007; D. Chan, Soljačić, & Joannopoulos, 2006). Perfectly reflective gratings are also well known for their applications to spectroscopy (Loewen & Popov, 1997),(Fortin & McCarthy, 2005). Gratings can act as polarizers as they are sensitive to transverse electric (TE) and transverse magnetic (TM) polarizations (Shiraishi, Higuchi, Muraki, & Yoda, 2016). Thus, a large body of literature is dedicated to their analysis and simulation. Yet, most works assume an ideal deterministic shape, generally neglecting the effects of roughness or geometric *uncertainty* that the surface in reality may portray.

Roughness can be produced, for example, by manufacturing processes. Though generally small, these shape distortions can undermine a grating's performance. Consequently, robust engineering design must accurately account for such shape randomness. Providing an efficient tool for this purpose motivates the present work.

Due to the random nature of the perturbations, it is necessary to formulate the problem in terms of stochastic parameters. The most popular method employed for solving stochastic partial differential equations (SPDEs) is Monte-Carlo (MC) simulation (Matthew N O Sadiku, 2009). MC methods compute statistical moments—mean, variance, and so on—by simply taking large numbers of realizations or samples of the underlying random shapes to then solve the related boundary value problems and compute the statistics directly. This entails generating a large quantity of geometrical meshes (Khankhoje & Cwik, 2014), with the ensuing increase in computational burden and slow convergence rates. As an alternative to MC methods, the so-called analytical methods such as Kirchhoff approximation (KA) and small perturbation method (SPM) have been studied (Tsang et al., 2001). The work of Shin *et al.* (Shin & Kong, 1984) based on KA and Yueh *et al.* (Yueh, Shin, & Kong, 1988) based on SPM have addressed the problem of random perturbations on gratings. Recently, studies of multilayer structures have extended the applicability of the SPM (H. Wang et al., 2016; Sanamzadeh, Ts Deterministic approaches for SPDEs have recently been proposed to avoid the calculation of a set of samples (von Petersdorff et al., 2006; Bieri, Andreev, & Schwab, 2009; Harbrecht et al., 2006). These approaches revolve around the idea that if the randomness comes from known source terms and the operators are deterministic, then tensorized deterministic equations for the statistical moments can be obtained. In this approach, efforts are directed towards developing efficient computational frameworks for the tensor systems, in comparison to MC simulations.

In this work, we seek to compute the expected value and second statistical moments of fields scattered by a perfect electric conductor (PEC) grating with random surface perturbations. Assuming sufficiently small perturbations with respect to a nominal deterministic periodic shape, we perform a first-order shape Taylor expansion wherein perturbations are stochastic. One can show that the first shape derivative also satisfies a volume problem for the same partial differential operator, but with a different boundary term over the nominal domain (Potthast, 1996b). It can be shown that the shape derivative approach is mathematically equivalent to the SPM. However, the former allows to straightforward calculation of the expected value and the variance of the scattered field by knowing the mean and two-point correlation of the boundary perturbation field, while this is not straightforward in the SPM formulation.

As is customary, we reduce volume problems to ones cast over boundaries by establishing integral equations using suitable Green's functions. This dimension reduction diminishes considerably the number of degrees of freedom (DOFs) required to solve the problem in comparison to volume methods and avoids the implementation of fictitious boundaries (Jin, 2010). This basic approach has been recently developed for full 3D Maxwell scattering (Jerez-Hanckes & Schwab, 2016; Hiptmair, Jerez-Hanckes, & Schwab, 2013), but to our knowledge the application to periodic structures, such as gratings, remains an open problem.

The rest of the chapter is organized as follows: in Section 2.2, we define the scattering problem, shape derivatives and random perturbations as well as the the shape Taylor expansion. Boundary reduction for the scattering problem is described in Section 2.2.3 with boundary integral equations explained in Section 2.2.4. Section 2.3 introduces the definition of the tensorized equations for the second moment. In Section 2.4, we present related variational formulations and full and sparse discretizations. Galerkin MC simulations used for validating the proposed deterministic approach are described in Section 2.5. Section 2.6 presents numerical validation, convergence analysis and numerical examples including grating efficiency computations. Lastly, main conclusions are summarized in Section 2.7.

2.2. Model Problem

As shown in Figure 2.1, we consider a PEC grating with surface $\tilde{\Gamma} \times \mathbb{R}$ where $\tilde{\Gamma} \in \mathbb{R}^2$ is parametrized by a Λ-periodic mapping $\mathbb{R} \ni t \to (t, y(t))$, i.e. $y(t+\Lambda) = y(t)$. This defines the infinite open domain of propagation $\tilde{D} \times \mathbb{R} \subset \mathbb{R}^3$ as the upper half-space above the grating. We assume this volume to be free space, characterized by the impedance $\eta_0 = \sqrt{\mu_0/\varepsilon_0}$ and phase velocity $c = 1/\sqrt{\varepsilon_0 \mu_0}$, where ε_0 and μ_0 are the permittivity and permeability of vacuum, respectively. Due to the periodicity of the grating, we denote by Γ and D the surface and volume associated with a single period, respectively.

We decompose the electric and magnetic fields—denoted by $\mathbf{E}$ and $\mathbf{H}$, respectively—in cartesian coordinates (x, y, z). Although both transverse electric (TE) and transverse magnetic (TM) polarizations are possible, for the sake of brevity we only consider the TE case ($E_x = E_y = H_z = 0$). Furthermore, we assume time-harmonic excitations with angular frequency ω_0. Thanks to the z-invariance of the grating, the problem is further reduced to that of finding the total electric field space component E_z on a perpendicular plane to the grating:

$$u(\mathbf{r}) := E_z(\mathbf{r}), \quad \mathbf{r} \in \tilde{D} \subset \mathbb{R}^2, \tag{2.1}$$

satisfying the homogeneous Helmholtz equation:

$$\Delta u + k^2 u = 0 \quad \text{in } \tilde{D}, \tag{2.2}$$

and a homogenous Dirichlet boundary condition. The wavenumber $k := \omega_0/c$ yields a wavelength $\lambda = 2\pi/k$. By linearity, the total wave can be decomposed as $u = u^i + u^s$, where u^i and u^s are the incident and scattered waves, respectively. Without loss of generality, we consider incident plane waves (PW), i.e.

$$u^i = E_0 e^{-\imath \mathbf{k}_i \cdot \mathbf{r}}, \quad \mathbf{r} \in \tilde{D}, \tag{2.3}$$

with incident wavevector $\mathbf{k}_i = (k_x, k_y) = (k \sin\theta_i, k\cos\theta_i)$, where θ_i is the impinging angle. The amplitude E_0 can then be calculated through the Poynting vector ($\mathbf{S} = \mathbf{E} \times \mathbf{H}$), which for TE waves leads to the following relation for power (Jin, 2010):

$$P = \frac{E_0^2 \Lambda \cos\theta_i}{2\eta_0}. \tag{2.4}$$

As PWs satisfy (2.2), we seek the scattered field u^s such that

$$\Delta u^s + k^2 u^s = 0 \quad \text{in} \quad \tilde{D}, \tag{2.5}$$

$$u^s = -u^i \quad \text{on} \quad \tilde{\Gamma}, \tag{2.6}$$

$$y^{1/2}(\partial_y - \imath k)u^s \to 0 \quad \text{as } y \to \infty. \tag{2.7}$$

In this case, the periodicity and infinite length of the grating prevents the use of standard Sommerfeld radiation conditions (Kirsch, 1993) Equivalently, we can write down the boundary value problem for a quasi-periodic field u^s over D (Petit, 1980):

$$\Delta u^s + k^2 u^s = 0 \quad \text{in} \quad D, \tag{2.8}$$

$$u^s = -u^i =: g \quad \text{on} \quad \Gamma, \tag{2.9}$$

$$u^s(x+\Lambda, y) = e^{\imath k_x \Lambda} u^s(x,y) \quad \text{and} \tag{2.10}$$

$$u^s = \sum_{n\in\mathbb{Z}} u_n e^{i\mathbf{K}_n \cdot \mathbf{r}}, \quad y > \|y\|_\infty, \tag{2.11}$$

2.2.1. Small Random Shape Perturbations

As it will be shown in Section 3.1, we will consider wave scattering from small random perturbations of a nominal, sufficiently regular reference domain D_0 associated to a grating

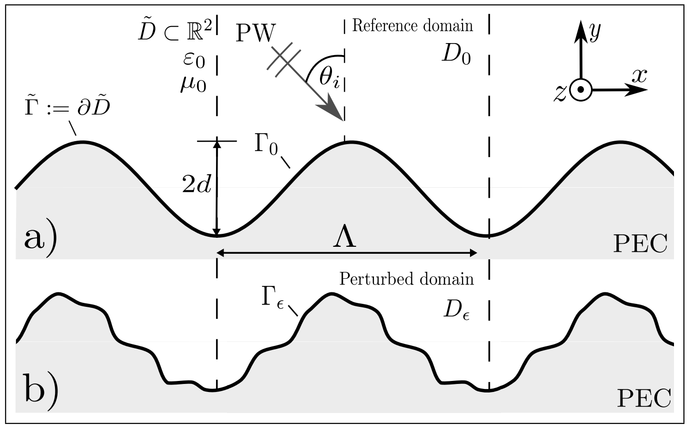

FIGURE 2.1. One-dimensional perfect electric conductor grating with periodicity in the x-direction, Λ, and angle of incidence θ_i defined with respect to the y-axis. The height of the grooves is $2d$. (a) shows the semi-infinite domain, $\tilde{D}$ its boundary $\tilde{\Gamma}$, the reference domain defined over one period, D_0, and its boundary, Γ_0. (b), shows a perturbed domain, D_ϵ, and its boundary, Γ_ϵ.

period Λ (Fig. 2.1). Without loss of generality, let us define perturbed surfaces

$$\Gamma_\epsilon := \{\mathbf{r} + \epsilon\kappa(\mathbf{r})\mathbf{n}_0(\mathbf{r}) : \mathbf{r} \in \Gamma_0\}, \quad 0 < \epsilon \ll 1, \tag{2.12}$$

where $\mathbf{n}_0$ is the outward unitary normal to Γ_0 and $\kappa \in \mathbb{R}$ is a bounded amplitude over Γ_0. The perturbed domain over a period, denoted by D_ϵ, is defined as the upper plane to Γ_ϵ for $x \in (0, \Lambda)$. Observe that the domain D_ϵ and D_0 match, except for a region relatively close to the grating surface.

In order to introduce shape randomness, we first set a standard probability space $(\Omega, \Sigma, \mathbb{P})$, where Ω is the sample space with elements $\omega \in \Omega$, Σ is a *σ-algebra*, and $\mathbb{P}$ is a probability measure. With this, we define random fields by further assuming a known random amplitude $\kappa(\mathbf{r}, \omega)$. We require the amplitude to be bounded from above and below, i.e.

$$\max_{\omega\in\Omega} |\kappa(\mathbf{r}, \omega)| < C, \quad C > 0, \quad \forall\, \mathbf{r} \in \Gamma_0. \tag{2.13}$$

Let us define the amplitude's first and second statistical moments as:

$$\mathbb{E}[\kappa](\mathbf{r}) \ := \ \int_{\Omega} \kappa(\mathbf{r},\omega) d\mathbb{P}(\omega), \tag{2.14}$$

$$\text{Cor}[\kappa](\mathbf{r},\mathbf{q}) \ := \ \int_{\Omega} \kappa(\mathbf{r},\omega)\kappa(\mathbf{q},\omega) d\mathbb{P}(\omega), \tag{2.15}$$

where $\mathbf{r}$, $\mathbf{q}$ lie on Γ_0. We further assume $\mathbb{E}[\kappa] = 0$ so that only centered perturbations are considered. Explicitly, for $\epsilon \ll 1$ and $k\epsilon \ll 1$, we set the randomly perturbed surface with respect to Γ_0:

$$\Gamma_\epsilon(\omega) := \{\mathbf{r} + \epsilon\kappa(\mathbf{r},\omega)\mathbf{n}_0(\mathbf{r}) : \mathbf{r} \in \Gamma_0, \omega \in \Omega\}, \tag{2.16}$$

so that $\mathbb{E}(\Gamma_\epsilon) = \Gamma_0$. We define perturbed domains $D_\epsilon(\omega)$ as described before. Even though the surface Γ_ϵ is periodic, which means that the random perturbations are also periodic, this is not a serious limitation, since it is possible to perform simulations over several periods.

2.2.2. Shape Taylor Expansion

The scattered field u^s_ϵ over $D_\varepsilon(\omega)$ must solve the same volume periodic problem (2.8)–(2.11) with a Dirichlet boundary condition equal to $g_\epsilon(\omega)$. Since the perturbations are small, we make use of a shape Taylor expansion. This entails evaluation of the shape derivative (Sokolowski & Zolesio, 1992; Harbrecht et al., 2006), defined as

$$\dot{u}^s(\mathbf{r},\omega) := \lim_{\epsilon\to 0} \frac{u^s_\epsilon(\mathbf{r},\omega) - u^s_0(\mathbf{r})}{\epsilon}, \quad \mathbf{r} \in D_0 \cap D_\epsilon(\omega), \tag{2.17}$$

where u^s_0 is the scattered solution over the nominal domain D_0. In this definition, $\dot{u}^s$ can be interpreted as the infinitesimal variation of the electric field due to the grating surface variations. Moreover, $\dot{u}^s$ satisfies the reference problem equations (2.8), (2.10), (2.11), over D_0 with a different right-hand side for the boundary condition (2.9) (Harbrecht et al., 2006). The boundary value problem satisfied by the shape derivative is (Sokolowski &

Zolesio, 1992):

$$\Delta \dot{u}^s + k^2 \dot{u}^s = 0 \qquad \text{in} \quad D_0, \tag{2.18}$$

$$\dot{u}^s = -\kappa(\cdot, \omega)\mathbf{n}_0 \cdot \nabla(u_0^s + u^i) \qquad \text{on} \quad \Gamma_0, \tag{2.19}$$

$$+ \text{ conditions (2.10), (2.11)} . \tag{2.20}$$

Hence, instead of computing u_ϵ in the perturbed domain, we will consider the first order approximation:

$$u_\epsilon^s(\mathbf{r}, \omega) = u_0^s(\mathbf{r}) + \epsilon \dot{u}^s(\mathbf{r}, \omega) + \mathcal{O}(\epsilon^2), \ \mathbf{r} \in D_0 \cap D_\epsilon(\omega), \tag{2.21}$$

and $\omega \in \Omega$. Observe that u_0^s is purely deterministic, while the shape derivative $\dot{u}^s$ depends on ω through the boundary condition term $\kappa(\mathbf{r}, \omega)$. Moreover, by construction one can show that

$$\mathbb{E}\left[\dot{u}^s\right](\mathbf{r}) = 0, \quad \mathbf{r} \in D_0, \tag{2.22}$$

since the expectation of (2.19) yields a zero boundary condition, implying a field equal to zero by unique solvability (Harbrecht et al., 2006). It can be shown that the boundary condition given for the shape derivative is the same as for SPM.

2.2.3. Boundary Reduction

Using (2.21), to approximate u_ϵ^s we require u_0^s and $\dot{u}^s$, both of which satisfy the same Helmholtz equation over D_0 differing solely in Dirichlet conditions. At the same time, both problems are set on an unbounded domain, which is why we resort to the use of boundary integral formulations. This requires the computation of a fundamental solution of the volume problem as will be shown.

In particular, our method is based on the so-called *indirect formulation* (Sauter & Schwab, 2011; Steinbach, 2008): for any scattered field u^s, we can write

$$u^s(\mathbf{r}) = (\mathsf{SL}\zeta)(\mathbf{r}), \quad \mathbf{r} \in D_0, \tag{2.23}$$

where SL is the single layer potential given as the convolution of the quasi-periodic Green's function, G^p, and a surface density ζ, in our case unknown:

$$(\mathsf{SL}\zeta)(\mathbf{r}) := \imath k\eta_0 \int_{\Gamma_0} G^p(\mathbf{r},\mathbf{r}')\zeta(\mathbf{r}')d\Gamma(\mathbf{r}'), \quad \mathbf{r} \in D_0. \tag{2.24}$$

Hence, the same representation can be used for u_0^s and $\dot{u}^s$. In fact, in Section 2.2.4 we show it suffices to find a suitable ζ rendering u_0^s and then obtain $\mathbf{n}_0 \cdot \nabla(u_0^s + u_0^i)$ on Γ_0 to derive an equation for $\dot{u}^s$. With this definition, the integral equation defined on D_0 can be written as:

$$\imath k\eta_0 \int_{\Gamma_0} G^p(\mathbf{r},\mathbf{r}')\zeta(\mathbf{r}')d\Gamma(\mathbf{r}') = -u^i(\mathbf{r}) \; \mathbf{r} \in D_0. \tag{2.25}$$

The quasi-periodic Green's function must satisfy the 2D Helmholtz equation for 1D quasi-periodicity:

$$(\Delta + k^2)G^p = \delta(y) \sum_{n=-\infty}^{\infty} \delta(x - n\Lambda)e^{\imath k_x m\Lambda}. \tag{2.26}$$

The solution of (2.26) has the spectral representation (Tsang et al., 2001):

$$G^p(\mathbf{r},\mathbf{r}') = \frac{\imath}{2\Lambda} \sum_{n=-\infty}^{\infty} \frac{e^{\imath k_{x,n}(x-x') + \imath k_{y,n}|y-y'|}}{k_{y,n}}, \tag{2.27}$$

where

$$k_{x,n} = k\sin\theta_i + 2n\pi/\Lambda, \; n \in \mathbb{Z}, \quad \text{and} \tag{2.28}$$

$$k_{y,n} = \begin{cases} \sqrt{k^2 - k_{x,n}^2} & \text{if } k^2 \geq k_{x,n}^2, \\ \imath\sqrt{k_{x,n}^2 - k^2} & \text{if } k^2 < k_{x,n}^2 \end{cases}. \tag{2.29}$$

Since this representation of G^p is known to converge slowly when $|y - y'|$ is small (Bruno & Haslam, 2009), we consider the following alternative:

$$G^p(\mathbf{r},\mathbf{r}') = \frac{\imath}{4}H_0^{(1)}(k\|\mathbf{r} - \mathbf{r}'\|) + \tilde{G}(\mathbf{r},\mathbf{r}'), \tag{2.30}$$

where $H_0^{(1)}$ is the Hankel function of first kind and $\tilde{G}$ is a smooth function whose formula can be found in (Bruno & Haslam, 2009). This representation is well behaved close to its singular points. Moreover, it also allows a straightforward extraction of its singular component: singular integrals in (2.24) can be computed semi-analytically while regular parts are integrated via Gauss-Legendre quadrature.

2.2.4. Boundary Integral Equations

By taking the values on the boundary of (2.24), we define the weakly singular ($\mathcal{V}$) boundary integral operator, $\mathcal{V}$, as $\mathcal{V}\zeta(\mathbf{r}) := \mathsf{SL}\zeta(\mathbf{r})$ with $\mathbf{r}$ on Γ_0 (Sauter & Schwab, 2011; Steinbach, 2008). With this, we can derive the first kind Fredholm integral equation for the scattered field u_0^s:

$$u^s(\mathbf{r}) = (\mathcal{V}\zeta)(\mathbf{r}) = g_0(\mathbf{r}), \quad \forall\, \mathbf{r} \in\ \Gamma_0, \tag{2.31}$$

using the boundary condition (2.9) with $\epsilon = 0$. Equation (2.31) is known as the Electric Field Integral Equation (EFIE) (Jin, 2010) given by:

$$\imath k\eta_0 \int_{\Gamma_0} G^p(\mathbf{r}, \mathbf{r}')\zeta(\mathbf{r}')d\Gamma(\mathbf{r}') = -u^i(\mathbf{r})\ \mathbf{r} \in \Gamma_0, \tag{2.32}$$

where $\zeta : \Gamma_0 \to \mathbb{C}$ is the surface current density. Notice that ζ is extended quasi-periodically over $\tilde{\Gamma}$. For a PEC surface $\zeta = \mathbf{n}_0 \cdot \nabla(u^s + u^i)$ on Γ_0, which allows the straightforward evaluation of (2.19). After solving (2.31), a similar equation holds for the shape derivative, i.e. there exists a $\dot{\zeta}(\mathbf{r}, \omega) : \Gamma_0 \times \Omega \to \mathbb{C}$ such that:

$$(\mathcal{V}\dot{\zeta})(\mathbf{r}, \omega) = \kappa(\mathbf{r}, \omega)\zeta(\mathbf{r}), \quad \forall\, \mathbf{r} \in \Gamma_0, \text{ and} \tag{2.33}$$

$$\dot{u}^s(\mathbf{r}, \omega) = (\mathsf{SL}\dot{\zeta})(\mathbf{r}, \omega), \quad \forall\, \mathbf{r} \in D_0. \tag{2.34}$$

As in the case of (2.32), we can write (2.33) as follows:

$$\begin{aligned} &\imath k\eta_0 \int_{\Gamma_0} G^p(\mathbf{r}, \mathbf{r}')\dot{\zeta}(\mathbf{r}')d\Gamma(\mathbf{r}') = \\ &\kappa(\mathbf{r}, \omega)\mathbf{n}_0 \cdot \nabla(u^s + u^i)\ \mathbf{r} \in \Gamma_0. \end{aligned} \tag{2.35}$$

Observe that while (2.31) has a deterministic right-hand side (2.33) has an stochastic one. Throughout this manuscript, the following convention has been adopted: vectors are written in bold text, e.g. the position vector $\mathbf{r}$, potentials in sans-serif font, e.g. the single layer potential SL, operators in calligraphic font, e.g. the weakly singular operator $\mathcal{V}$, and all functions and variables (discrete and continuous) in normal font, e.g. the grating profile $y(t)$ or the quasi-periodic Green's function G^p.

2.3. Deterministic Tensor Equations

Our main goal is to obtain the first two statistical moments for the scattered field u^s_ϵ: namely, the field's expected value and covariance. In general, p-order moments are given by:

$$\begin{aligned} \mathcal{M}^p u &:= \mathbb{E}[u \otimes \ldots \otimes u] \\ &:= \int_{\omega \in \Omega} u(\omega) \otimes \ldots \otimes u(\omega) d\mathbb{P}(\omega), \end{aligned} \tag{2.36}$$

for $p \in \mathbb{N}$. Hence, first and second moments are denoted by $\mathcal{M}^1 u = \mathbb{E}[u]$ and $\mathcal{M}^2 u =$ Covar$[u]$, respectively. For a complex-valued random field $u(\omega)$, the variance and pseudo-variance (Neeser & Massey, 1993) are

$$\text{Var}[u] := \mathbb{E}[(u - \mathbb{E}[u]) \overline{(u - \mathbb{E}[u])}], \tag{2.37}$$

$$\text{PVar}[u] := \mathbb{E}\left[(u - \mathbb{E}[u]) (u - \mathbb{E}[u])\right], \tag{2.38}$$

with overline denoting complex conjugation.

2.3.1. Abstract Setting

We follow the theory described in (von Petersdorff et al., 2006; Harbrecht et al., 2006) where full proofs and details are presented. Given a probability space $(\Omega, \Sigma, \mathbb{P})$ and a separable Hilbert space H with dual H', we define a random source $f(\omega) \in H'$ and a deterministic linear operator $\mathcal{A} : H \to H'$. We then consider the operator equation for $h(\omega) \in H$:

$$\mathcal{A} h(\omega) = f(\omega) \quad \omega \in \Omega. \tag{2.39}$$

Taking moments (2.36) of the equation above, we can deduce

$$\mathcal{A}\mathcal{M}^1 h = \mathcal{M}^1 f, \tag{2.40}$$

$$(\mathcal{A}\otimes\mathcal{A})\mathcal{M}^2 h = \mathcal{M}^2 f. \tag{2.41}$$

Since the Helmholtz operator $\Delta + k^2$, for k constant, is linear and deterministic, it fulfills the conditions prescribed to derive equations (2.40) and (2.41) (von Petersdorff et al., 2006).

2.3.2. Application to Periodic Helmholtz Scattering

Based on the first-order approximation (2.21) and due to the fact that $\mathbb{E}[\dot{u}^s] = 0$, the mean scattered field, $\mathbb{E}[u^s_\epsilon]$, can be approximated by the solution of the unperturbed grating:

$$\mathbb{E}[u^s_\epsilon] = u^s_0 + \mathcal{O}(\epsilon^2) \quad \text{on } D_0, \tag{2.42}$$

which, for $\epsilon \ll 1$, can be well approximated by the first term u^s_0 after solving the deterministic boundary integral equation (2.31). The first-order formulation does not conserve power, since when calculating the expected value of the Poynting vector, terms containing the mean shape derivative and its complex conjugate, or the incoherent power, do not vanish. It is possible to obtain a second order approximation (that does strictly conserve power) by setting the boundary conditions of Eq. (2.19) properly (Harbrecht et al., 2006).

Recalling that $\mathbb{E}[\kappa] \equiv 0$, one can show that the variance $\mathrm{Var}[u^s_\epsilon]$ of the randomly perturbed domain solution, for a first order approximation, satisfies:

$$\mathrm{Var}[u^s_\epsilon](\mathbf{r}) = \epsilon^2 \mathbb{E}[\dot{u}^s(\mathbf{r},\cdot)\overline{\dot{u}^s(\mathbf{r},\cdot)}] + \mathcal{O}(\epsilon^3), \quad \mathbf{r} \in D_0. \tag{2.43}$$

Using (2.22), we retrieve the relation:

$$\begin{aligned}\mathrm{Var}[\dot{u}^s](\mathbf{r}) &= \mathbb{E}\left[(\dot{u}^s - \mathbb{E}[\dot{u}^s]) \cdot \overline{(\dot{u}^s - \mathbb{E}[\dot{u}^s])}\right](\mathbf{r}) \\ &= \mathbb{E}[\dot{u}^s(\mathbf{r},\cdot) \otimes \overline{\dot{u}^s(\mathbf{q},\cdot)}]\big|_{\mathbf{r}=\mathbf{q}} \\ &= \mathrm{Cor}[\dot{u}^s](\mathbf{r},\mathbf{q})\big|_{\mathbf{r}=\mathbf{q}}\end{aligned} \tag{2.44}$$

It is worth mentioning that $\mathbf{r}$ and $\mathbf{q}$ are both position vectors used to denote correlation variables. In contrast, $\mathbf{r}$ and $\mathbf{r}'$ in (2.24) are both position vectors used to denote an observer and a source of the electromagnetic field, respectively. As in (2.41), we can derive $\mathrm{Cor}[\dot{u}^s](\mathbf{r},\mathbf{q})$ as the solution of the volume tensor deterministic equation:

$$(\Delta + k^2) \otimes (\Delta + k^2)\mathrm{Cor}[\dot{u}^s] = 0 \quad \text{in } D_0 \times D_0, \tag{2.45}$$

$$\mathrm{Cor}[\dot{u}^s] = \mathrm{Cor}[\kappa]\left(\zeta \otimes \overline{\zeta}\right), \quad \text{on } \Gamma_0 \times \Gamma_0, \tag{2.46}$$

$$\begin{aligned}(e^{\imath k_x \Lambda} \otimes e^{\imath k_x \Lambda})\mathrm{Cor}[\dot{u}^s](\mathbf{r},\mathbf{q}) &= \\ \mathrm{Cor}[\dot{u}^s](x_r + \Lambda, y_r, x_q + \Lambda, y_q),\end{aligned} \tag{2.47}$$

$$\mathrm{Cor}[\dot{u}^s](\mathbf{r},\mathbf{q}) = \sum_{n,n' \in \mathbb{Z}} U_{n,n'} e^{i(\mathbf{K}\cdot\mathbf{r} + \mathbf{K}'\cdot\mathbf{q})}, \tag{2.48}$$

By employing the integral formulation (2.34) and linearity, the tensorized SL potential representation is

$$\mathrm{Cor}[\dot{u}^s](\mathbf{r},\mathbf{q}) = (\mathsf{SL} \otimes \overline{\mathsf{SL}})M_V(\mathbf{r},\mathbf{q}), \tag{2.49}$$

where $M_V(\mathbf{r},\mathbf{q}) : \Gamma_0^{(2)} \to \mathbb{C}$ is a bivariate surface density with $\Gamma_0^{(2)} := \Gamma_0 \times \Gamma_0$. Consequently, following (2.33) we must solve the tensor integral equation defined on the boundary $\Gamma_0^{(2)}$:

$$(\mathcal{V} \otimes \overline{\mathcal{V}})M_V = \mathrm{Cor}[\kappa]\left[\zeta \otimes \overline{\zeta}\right], \tag{2.50}$$

which can be explicitly written as:

$$\begin{aligned}-k^2\eta_0^2 \int_{\Gamma_0^{(2)}} G^p(\mathbf{r},\mathbf{r}')\overline{G^p(\mathbf{q},\mathbf{q}')}M_V(\mathbf{r}',\mathbf{q}')d\Gamma^{(2)}(\mathbf{r}',\mathbf{q}') &= \\ \mathrm{Cor}[\kappa][\zeta \otimes \overline{\zeta}],\end{aligned} \tag{2.51}$$

where $\int_{\Gamma^{(m)}} := \int_{\Gamma^{(1)}} \cdots \int_{\Gamma^{(m)}}$. The derivation for the calculation of pseudo-variance is analogous and is omitted here for the sake of brevity. In this case, the associated bivariate surface density satisfies

$$(\mathcal{V} \otimes \mathcal{V})M_{PV} = \mathrm{Cor}[\kappa]\left[\zeta \otimes \zeta\right]. \tag{2.52}$$

2.4. Variational Formulation and Discretization

In what follows, we present variational formulations for the mean scattered field and shape derivative covariance. Our approximation method for both equations is based on the Method of Moments (MoM) (Jin, 2010), also known as Boundary Element Method (Sauter & Schwab, 2011), with hierarchical piecewise constant functions (Haar wavelets) (Steinbach, 2008) as the discretization basis. This basis is chosen to mitigate the so-called *curse of dimensionality*, typical in uncertainty quantification methods (von Petersdorff et al., 2006; Bieri et al., 2009). Indeed, direct tensorization of the approximation basis increases the number of DOFs from N to N^2. By using a hierarchical basis, we can naturally perform a sparse approximation for the tensor quantities (2.50) and (2.52) with DOFs growing as $O(N \log N)$ thereby achieving a more efficient calculation. Hence, we will compare *sparse* versus *full* tensor approximations. Finally, we present the derivation for the variance M_V, as similar steps apply to computation of pseudo-variance.

2.4.1. Variational Formulations

The variational formulation for the first moment or mean field u_0^s is derived from (2.31) as follows:

$$\langle \mathcal{V}\zeta, w\rangle_{\Gamma_0} = \langle g_0, w\rangle_{\Gamma_0} \text{ or,} \tag{2.53}$$

$$\begin{aligned} \int_{\Gamma_0} w(\mathbf{r}) \int_{\Gamma_0} G^p(\mathbf{r}, \mathbf{r}')\zeta(\mathbf{r}')d\Gamma(\mathbf{r}')d\Gamma(\mathbf{r}) = \\ - \int_{\Gamma_0} w(\mathbf{r}) u^i(\mathbf{r}') d\Gamma(\mathbf{r}) \end{aligned} \tag{2.54}$$

where w are test functions and $\langle u, w\rangle_{\Gamma_0}$ is a duality pairing. For the density M_V in (2.50), the tensorized variational form is obtained:

$$\langle (\mathcal{V} \otimes \overline{\mathcal{V}}) M_V, W\rangle_{\Gamma_0^{(2)}} = \langle \text{Cor}[\kappa] \left(\zeta \otimes \overline{\zeta}\right), W\rangle_{\Gamma_0^{(2)}}, \tag{2.55}$$

which can be written in an expanded form as:

$$
\begin{aligned}
-k^2\eta_0^2 \int_{\Gamma_0^{(2)}} W(\mathbf{r},\mathbf{q}) \int_{\Gamma_0^{(2)}} G^p(\mathbf{r},\mathbf{r}')\overline{G^p(\mathbf{q},\mathbf{q}')}\times \\
M_V(\mathbf{r}',\mathbf{q}')d\Gamma^{(2)}(\mathbf{r}',\mathbf{q}')d\Gamma^{(2)}(\mathbf{r},\mathbf{q}) = \\
\int_{\Gamma_0^{(2)}} W(\mathbf{r},\mathbf{q})\mathrm{Cor}[\kappa][\zeta\otimes\overline{\zeta}]d\Gamma^{(2)}(\mathbf{r},\mathbf{q}),
\end{aligned}
\tag{2.56}
$$

where W is a real bivariate test function and ζ is the solution of (2.53). It should be noted that the tensor duality product is just the multiplication of individual duality products. Therefore, if separable, tensor duality components can be written as linear combinations of one-dimensional tensor products, i.e.

$$
\langle v_1 \otimes v_2, w_1 \otimes w_2 \rangle_{\Gamma_0\times\Gamma_0} = \langle v_1, w_1\rangle_{\Gamma_0}\langle v_2, w_2\rangle_{\Gamma_0}. \tag{2.57}
$$

Hence, in the following, we will approximate M and W by tensor products of independent functions defined over Γ_0.

2.4.2. Discretization and Sparse Approximation

Haar wavelets are defined by first introducing the function (Steinbach, 2008):

$$
\phi(\xi) = \begin{cases} 1 & \text{if } 0 < \xi \leq 1/2, \\ -1 & \text{if } 1/2 < \xi \leq 1, \\ 0 & \text{otherwise.} \end{cases} \tag{2.58}
$$

All basis functions are generated by using a change of variables from $[0,\Lambda]$ to $[0,1]$. Scaling functions $\tilde{\psi}_j^l$ are given by:

$$
\tilde{\psi}_j^l(t) = \begin{cases} 1 \quad \text{if } j = 1 \text{ and } l = 0, \\ 2^{l/2}\phi(2^l t - (j-1)) \quad \text{otherwise,} \end{cases} \tag{2.59}
$$

with levels $l = 0,\ldots,L$, $L \in \mathbb{N}$ being the maximum approximation refinement level, and $j = 1,\ldots,2^l$. To compute the boundary integrals of (2.53), we require the Jacobian of the parametrization in $t \in [0,\Lambda]$ as $\mathsf{J}(t) = \sqrt{x'(t)^2 + y'(t)^2}$. The definition of the following modified discretization basis, allows for the elimination of $\mathsf{J}(t)$ from the boundary integrals

$$\psi_j^l(t) := \frac{\tilde{\psi}_j^l(t)}{\mathsf{J}(t)}, \quad l = 0, 1, \ldots, L, \text{ and } j = 1, \ldots 2^l. \tag{2.60}$$

Then, the approximation of a univariate surface density ζ in (2.53) through a hierarchical basis with a maximum refinement level L, denoted $P_1^L\zeta$, is written as:

$$P_1^L\zeta(t) := \sum_{l=0}^{L}\sum_{j=1}^{2^l} a_j^l \psi_j^l(t), \quad t \in [0, \Lambda]. \tag{2.61}$$

As we need to model oscillatory wave behavior, a minimum or a base level $L_0 \in \mathbb{N}$, dependent on the wavenumber k, is necessary before observing asymptotic convergence.

For the tensorized equation (2.50), the *dense* approximation of M_V is computed in terms of tensorized basis functions:

$$P_2^L M_V(t, s) := \sum_{l_1=0}^{L}\sum_{l_2=0}^{L}\sum_{j_1=1}^{2^{l_1}}\sum_{j_2=1}^{2^{l_2}} \mathrm{A}_{j_1,j_2}^{l_1,l_2} \psi_{j_1}^{l_1}(t)\psi_{j_2}^{l_2}(s), \tag{2.62}$$

where $\mathrm{A}_{j_1,j_2}^{l_1,l_2}$ are unknown coefficients. Hence, tensorization increases the DOFs from N to N^2 and again we enforce the minimum resolution level $0 < L_0 \leq L$ in each direction. Therefore, in order to compute the second moment efficiently it is necessary to introduce a sparse approximation. Following Schwab & von Petersdorff (von Petersdorff et al., 2006) or Hiptmair *et al.*, (Hiptmair et al., 2013), we define the index set:

$$\mathcal{I}(L_0, L) := \{0 \leq l_1, l_2 \leq L : 0 \leq l_1 + l_2 \leq L + L_0\}$$

with which the sparse approximation of M_V is given by

$$\hat{P}_2^L M_V(t, s) := \sum_{(l_1,l_2)\in\mathcal{I}(L_0,L)}\sum_{j_1=1}^{2^{l_1}}\sum_{j_2=1}^{2^{l_2}} \hat{\mathrm{A}}_{j_1,j_2}^{l_1,l_2} \psi_{j_1}^{l_1}(t)\psi_{j_2}^{l_2}(s), \tag{2.63}$$

with $\hat{\mathrm{A}}_{j_1,j_2}^{l_1,l_2}$ as unknown coefficients. This particular choice reduces the number of DOFs from N^2 to $\mathcal{O}(N \log N)$.

As is customary in MoM approximations, for the first moment test functions w are chosen as ψ_j^l. Combining (2.53) and the discretization in (2.61), the following linear system is obtained:

$$\sum_{l=0}^{L}\sum_{j=1}^{2^l} a_j^l \mathrm{V}_{j,j'}^{l,l'} = b_{j'}^{l'}, \quad l' = 0, \ldots, L,\ j' = 1, \ldots, 2^{l'}. \tag{2.64}$$

The entries of this matrix and the right-hand side can be computed as $(\mathrm{V}_{j,j'}^{l,l'}) := \left\langle \mathcal{V}\psi_j^l, \psi_{j'}^{l'} \right\rangle_{\Gamma_0}$, and $(b_{j'}^{l'}) = \langle g_0, \psi_{j'}^{l'} \rangle_{\Gamma_0}$, respectively. For the case of the covariance, applying a full (2.62) or sparse (2.63) approximation to (2.55), the matrix can be easily computed by multiplying $\mathrm{V}_{j_1,j_1'}^{l_1,l_1'}$ $\mathrm{V}_{j_2,j_2'}^{l_2,l_2'}$, where $l_1', l_2' = 0, \ldots, L$, and $j_1', j_2' = 1, \ldots 2^{\{l_1', l_2'\}}$ for the dense case or $(l_1', l_2') \in \mathcal{I}(L_0, L)$ for the sparse one. The right-hand sides for both dense and sparse approximations depend on the approximation of $P_1^L \zeta$ in (2.61) as

$$\begin{aligned}\mathrm{B}_{j_1',j_2'}^{l_1',l_2'} = \iint_{\Gamma_0^{(2)}} & \mathrm{Cor}[\kappa](t,s) \\ \times P_1^L \zeta(t) \overline{P_1^L \zeta(s)} & \psi_{j_1'}^{l_1'}(t) \psi_{j_2'}^{l_2'}(s) d\Gamma(t) d\Gamma(s).\end{aligned} \tag{2.65}$$

Further computational efficiency is achieved by employing the combination technique (Harbrecht, Peters, & Siebenmorgen, 2013). This allows for the parallel calculation of $2(L - L_0) + 1$ independent linear systems of order $\mathcal{O}(N)$ instead of a large $\mathcal{O}(N \log N)$ system. Finally, the goal of this work is to solve (2.54) to obtain the surface current density, ζ, and (2.56) to obtain the density function, M_V, (or M_{PV} in the case of pseudo-variance). With them, it is possible to reconstruct the mean and variance fields. This can be applied to compute the mean and variance of the grating efficiency (Section 2.6.4).

2.5. Galerkin Monte-Carlo Approximation

Monte-Carlo simulation has been extensively used for electromagnetism (Sy, van Beurden, Michielsen, Vaessen, & Tijhuis, 2010) in combination with different numerical schemes such as the Finite Element Method (FEM) (Ozgun & Kuzuoglu, 2013) or MoM (Ohnuki, Chew, & Hinata, 2005) in order to solve SPDEs. Moreover, various techniques have been implemented in order to speed up MC simulations (Khankhoje & Cwik, 2014; Yang & Du, 2014). In this work, to compare and validate the first and second statistical moments obtained via sparse and dense tensor deterministic equations, MC simulations were performed (von Petersdorff et al., 2006). To achieve this, we consider J realizations for domains $D_\epsilon(\omega_j)$, with $\omega_j \in \Omega$, $j = 1, \ldots, J$, uniformly distributed. The expected convergence rate for the MC method is $\mathcal{O}(J^{-1/2})$ (von Petersdorff et al., 2006); therefore, a large number of realizations is required to obtain a given precision.

The boundary of each domain is given by $\Gamma_\epsilon(\omega_j) := \partial D_\epsilon(\omega_j)$ for $j = 1, \ldots, J$. These domains are generated by considering the function $\kappa(\cdot, \omega) \in C^\infty[0, \Lambda]$ and (2.16). Then, we solve (2.31) variationally J-times, i.e.

$$\langle \mathcal{V}\zeta(\omega_j), w \rangle_{\Gamma_\epsilon(\omega_j)} = \langle g_\epsilon(\omega_j), w \rangle_{\Gamma_\epsilon(\omega_j)}, \; j = 1, \ldots, J. \tag{2.66}$$

The expanded form of this equation is given by (2.54), integrating over randomly generated surfaces, $\Gamma(\omega_j)$. For each realization, the scattered field is obtained by applying the SL operator to the solution of (2.66), i.e.

$$u^s_\epsilon(\mathbf{r}, \omega_j) = \mathsf{SL}\zeta(\mathbf{r}, \omega_j), \mathbf{r} \in D_\epsilon(\omega_j), \; j = 1, \ldots, J. \tag{2.67}$$

The mean field is directly obtained by computing:

$$\mathbb{E}[u^s_\epsilon](\mathbf{r}) \approx \frac{1}{J} \sum_{j=1}^{J} u^s_\epsilon(\mathbf{r}, \omega_j), \quad \mathbf{r} \in \bigcap_{j=1}^{J} D_\epsilon(\omega_j). \tag{2.68}$$

Once the expected value in (2.68) is obtained, as well as the scattered field for each random surface $\Gamma(\omega_j)$, the variance of the scattered field can be directly approximated as:

$$\mathrm{Var}[u^s_\epsilon](\mathbf{r}) \approx \frac{1}{J} \sum_{j=1}^{J} (u^s_\epsilon(\omega_j) - \mathbb{E}[u^s_\epsilon]) \overline{(u^s_\epsilon(\omega_j) - \mathbb{E}[u^s_\epsilon])}. \tag{2.69}$$

Similar steps hold for the pseudo-variance.

2.6. Validation and Numerical Results

To validate our model we performed several simulations and examples. As a first step, we calculated the surface current density, given by ζ in the MoM approximation, with a simulation based on FEM using COMSOL Multiphysics 5.1 (Comsol, 2015) and compared it to our results. Next, the MC method described above was implemented to validate the mean and variance fields as well as the grating efficiency.

For the aforementioned purposes as well as for providing convergence tests, a nominal sinusoidal grating geometry is considered:

$$\mathbf{r}(t) = (x(t), y(t)) = \left(t, 2d\cos\left(\frac{2\pi t}{\Lambda}\right)\right) \quad t \in [0, \Lambda], \tag{2.70}$$

which defines Γ_0.

Finally, it should be mentioned that all linear systems for both the first and second moment were directly solved by using a LAPACK subroutine (Anderson et al., 1992).

2.6.1. Boundary Elements Validation

MoM solutions are checked by analyzing two different gratings. Firstly, a case with zero angle of incidence for which the wavelength is greater than the period was used. Secondly, a case with an angle of incidence other than zero for which the wavelength is lower than the period was evaluated. The simulations performed with COMSOL consider $\sim 10^6$ DOFs, while the MoM simulations consider a level of refinement of $L = 9$ (512 DOFs). Both cases show an almost perfect match (Fig. 2.2).

2.6.2. Stochastic Simulation Validation

We now compare the deterministic approach with the MC method. The construction of the perturbed domain is given in terms of Fourier series. Set a number of modes $N_n = 5$. Then, for $C_{i,n}(\omega_j)$, $i = 1, 2$ and $j = 1, \ldots, J$, uniformly distributed in $[-\sqrt{3}, \sqrt{3}]$, build

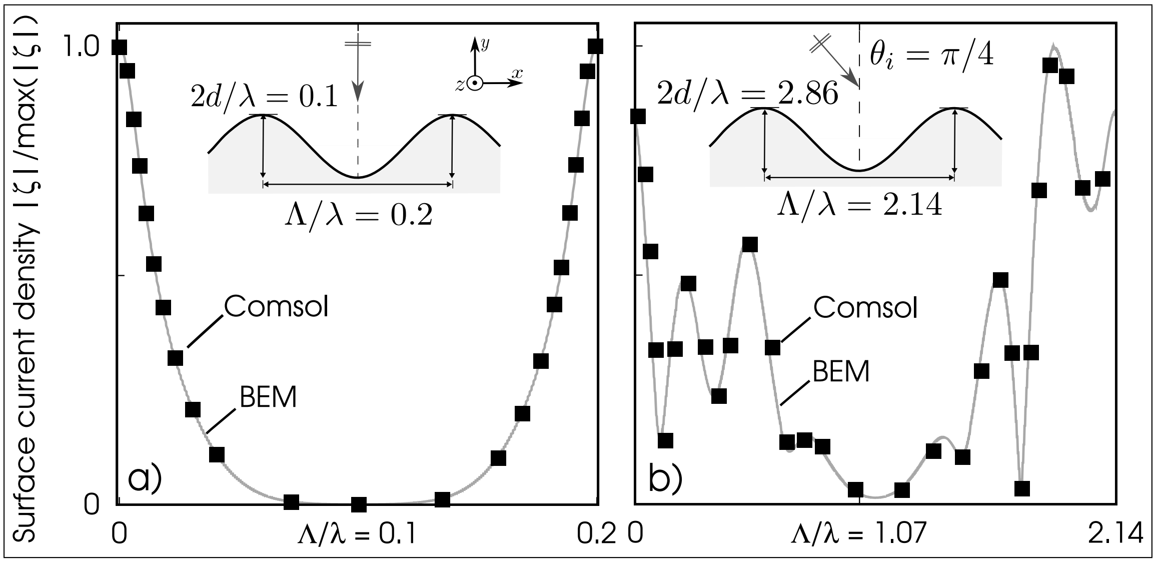

FIGURE 2.2. Comparison of the normalized surface current densities for MoM validation. The simulation parameters for the first case (a) are $\theta_i = 0$, $\Lambda/\lambda = 0.2$, and $2d/\lambda = 0.1$. For the second case (b) $\theta_i = \pi/4$, $\Lambda/\lambda = 2.14$, and $2d/\lambda = 2.86$. In the insets, the simulated grating geometries (2.70) are shown.

$\kappa(t, \omega_j) \in C^\infty[0, \Lambda]$ as

$$\kappa(t, \omega_j) = \sum_{n=1}^{N_n} C_{1,n}(\omega_j) \sin\left(\frac{2\pi n t}{\Lambda}\right) + C_{2,n}(\omega_j) \cos\left(\frac{2\pi n t}{\Lambda}\right). \tag{2.71}$$

The formulation for the rough sinusoidal profile considered here differs from that in (Shin & Kong, 1984) and (Yueh et al., 1988), in which the surface perturbations are treated as a random Gaussian process. Instead, we consider uniformly distributed Fourier coefficients so as to guarantee the small perturbation assumption. This perturbation field allows for the calculation of the correlation function and their integrals easily, since

$$\begin{aligned}\mathrm{Cor}[\kappa](t, s) = \sum_{n=1}^{N_n} &\sin\left(\frac{2\pi n t}{\Lambda}\right) \sin\left(\frac{2\pi n s}{\Lambda}\right) \\ &+ \cos\left(\frac{2\pi n t}{\Lambda}\right) \cos\left(\frac{2\pi n s}{\Lambda}\right).\end{aligned} \tag{2.72}$$

We considered $L = 6$ (64 DOFs) and a perturbation of $\epsilon = 0.001$, which corresponds to 1% of the amplitude. For this example, $J = 5000$ realizations were performed to obtain convergence of the mean and variance fields. Comparing the MC simulation with the deterministic approach, the calculated variance error is approximately 3.2% for distances greater than λ. Moreover, when $y < 2d$ the error is approximately 4% with a peak of 6.5 % (Fig. 2.3).

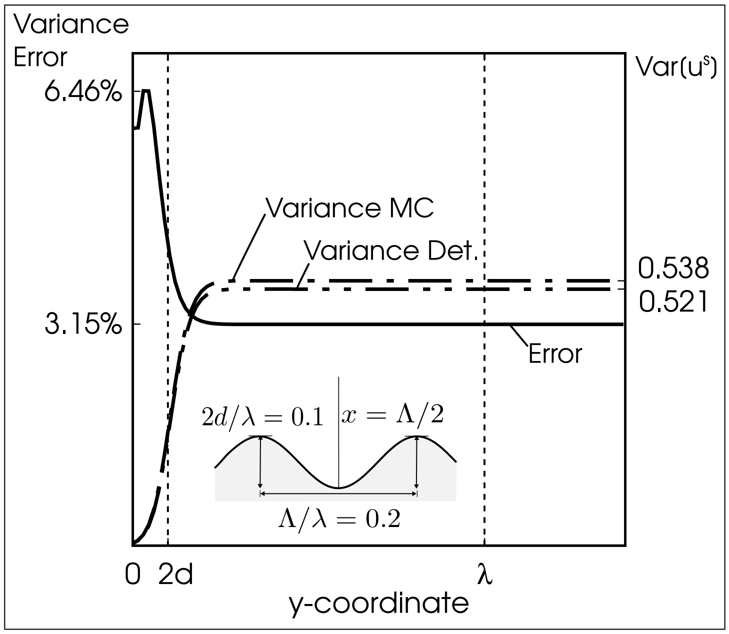

FIGURE 2.3. Normalized variance of the scattered field (u^s) for both MC method and the deterministic sparse approach, and the error between the fields as a function of the y coordinate for $x = \Lambda/2 = 0.1$. The simulation parameters are: $\theta_i = 0$, $2d/\lambda = 0.1$, and $\Lambda/\lambda = 0.2$ (Fig. 2.2). The maximum discretization level is $L = 6$ (3072 DOFs for the sparse approximation) for both methods.

2.6.3. Convergence

We now study the convergence rates of the deterministic method for both statistical moments by calculating the errors for different values of the wavenumber, k, and angle of incidence, θ_i. Moreover, all errors were quantified by using the relative L^2-norm of the densities and considering a dense maximum refinement level of $L = 11$ (4.2×10^6 DOFs) as the "overkill" solution (denoted as M_{11} in Table 2.1).

We obtained a convergence rate of 1.0 for mean field as expected for the cases described (see inset of Fig. 2.4). For the second moment, the dense approximation presents a convergence rate of 0.50 for two different wavenumbers, $k = 6$ and 42, with $\theta_i = 0$ and $\pi/3$, respectively. Notice that in the case of sparse approximation a base level $L_0 = 5$ (1024 DOFs) is necessary before obtaining convergence (see Fig. 2.4). For the sparse approximation, we obtained convergence rates that behave as $\mathcal{O}(N^{-1}\log N)$, implying faster convergence with increasing number of DOFs (see Table 2.1).

One of the advantages of our approach is the reduction in computational time. For one of our numerical examples (Fig. 2.3), the total time required to obtain both the mean and variance field is roughly 607 s for a 10 AMD Opteron cluster (2.8 GHz). Meanwhile, with the MC method the required time took approximately ~ 68 hours.

TABLE 2.1. Sparse Approximation Convergence Rates, $k = 42$

L	DOFs	$\|M_{11} - M_L\|_{L^2}$	rate
5	1024	0.5402	–
6	3072	0.2880	0.57
7	8192	0.1470	0.69
8	20480	0.0773	0.70
9	49152	0.0409	0.73
10	114688	0.0217	0.75

2.6.4. Variance and Mean of the Grating Efficiency

Gratings exhibit a diffraction efficiency measured as a function of wavelength, period, diffraction order, and polarization. The efficiency can be obtained by defining the scattered field for a region in $y > \max\{y(t)\}$, denoted by u_+^s, in terms of propagation modes in the far-field, which is known as the Rayleigh expansion (Petit, 1980):

$$u_+^s = \sum_{n=-\infty}^{\infty} c_n e^{\imath \mathbf{K}_n \cdot \mathbf{r}}, \tag{2.73}$$

where $\mathbf{K}_n := (k_{x,n}, k_{y,n})$ with $k_{x,n}$ and $k_{y,n}$ defined in (2.28) and (2.29), respectively, and

$$c_n = \frac{\imath}{2\Lambda k_{y,n}} \int_\Gamma e^{-\imath \mathbf{K}_n \cdot \mathbf{r}'} \zeta(\mathbf{r}') d\Gamma(\mathbf{r}'). \tag{2.74}$$

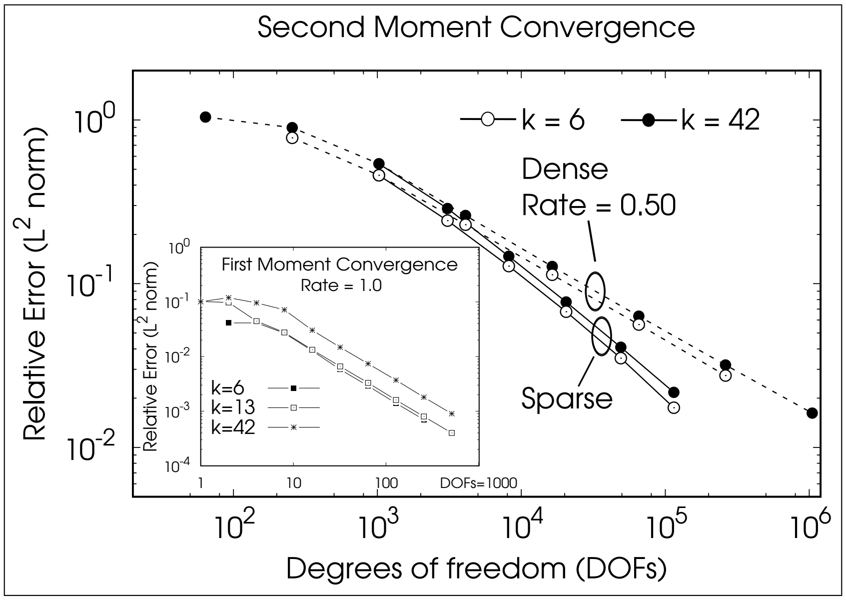

FIGURE 2.4. Convergence of sparse and full covariance approximations in relative L^2-norm for wavenumbers $k = 6$ and 42 with $\theta_i = 0$ and $\pi/3$, respectively. Convergence rates are equal to 0.5 for the dense case. For the sparse approximation, rates are improved as the number of DOFs increases (Table 2.1). In the inset, the convergence of first moment for the three simulated wavenumbers $k = 6$, 13, and 42 with $\theta_i = 0$, $\pi/4$, and $\pi/3$, respectively is shown. In each case, convergence is equal to one as expected.

Then, the efficiency of the n-th mode is defined as:

$$e_n = \frac{\mathrm{Re}(k_{y,n})}{k_y} |c_n|^2. \tag{2.75}$$

In the far field, evanescent modes (Re$(k_{y,n}) = 0$) do not contribute to the scattered field and are, consequently, disregarded. In view of this formulation, where the Rayleigh coefficients are obtained directly from ζ, the sum of the propagating modes is equal to one, conserving power. By considering the expected value, the variance, pseudo-variance, their related densities, and the shape Taylor expansion we can find closed form expressions to calculate the expected value of the grating efficiency as well as its variance. Let us consider $e_n(\omega)$ and $c_n(\omega)$, the grating efficiency and Rayleigh coefficient for the n-th mode on the perturbed domain $\Gamma_\epsilon(\omega)$ defined as in (2.16). Then, the expected value of the grating efficiency can be approximated at order $\mathcal{O}(\epsilon^2)$ as the nominal efficiency:

$$\mathbb{E}[e_n] = \frac{\text{Re}(k_{y,n})}{k_y}\mathbb{E}[c_n\overline{c_n}] \approx \frac{\text{Re}(k_{y,n})}{k_y}|c_n|^2. \tag{2.76}$$

For the variance of the efficiency, we have

$$\text{Var}[e_n] = \left(\frac{\text{Re}(k_{y,n})}{k_y}\right)^2 \text{Var}[c_n\overline{c_n}]. \tag{2.77}$$

Therefore, we must consider:

$$\text{Var}[c_n\overline{c_n}] = \mathbb{E}[(c_n\overline{c_n})^2] - (\mathbb{E}[c_n\overline{c_n}])^2, \tag{2.78}$$

which at $\mathcal{O}(\epsilon^3)$ can be obtained as follows:

$$\text{Var}[c_n\overline{c_n}] \approx \frac{1}{(2\Lambda k_{y,n})^4}\int_{\Gamma_0^{(4)}} e^{-\imath\mathbf{K}_n\cdot\mathbf{Q}} Z(\mathbf{R})d\Gamma^{(4)}(\mathbf{R}), \tag{2.79}$$

where $\Gamma_0^{(4)} := \Gamma_0^{(2)} \times \Gamma_0^{(2)}$. In this case $\mathbf{Q} = \mathbf{r} - \mathbf{r}' + \mathbf{q} - \mathbf{q}'$, $\mathbf{R} = (\mathbf{r}, \mathbf{r}', \mathbf{q}, \mathbf{q}')$, and

$$\begin{aligned} Z(\mathbf{R}) = \quad & \epsilon^2[M_V(\mathbf{r},\mathbf{r}') \otimes \zeta(\mathbf{q}) \otimes \overline{\zeta(\mathbf{q}')} \\ + \quad & M_{PV}(\mathbf{r},\mathbf{q}) \otimes \overline{\zeta(\mathbf{r}')} \otimes \overline{\zeta(\mathbf{q}')} \\ + \quad & M_V(\mathbf{r},\mathbf{q}') \otimes \overline{\zeta(\mathbf{r}')} \otimes \zeta(\mathbf{q}) \\ + \quad & \overline{M_V(\mathbf{r}',\mathbf{q})} \otimes \zeta(\mathbf{r}) \otimes \overline{\zeta(\mathbf{q}')} \\ + \quad & \overline{M_{PV}(\mathbf{r}',\mathbf{q}')} \otimes \zeta(\mathbf{r}) \otimes \zeta(\mathbf{q}) \\ + \quad & M_V(\mathbf{q},\mathbf{q}') \otimes \zeta(\mathbf{r}) \otimes \overline{\zeta(\mathbf{r}')}], \end{aligned} \tag{2.80}$$

where $Z(\mathbf{R}) : \Gamma_0^{(4)} \to \mathbb{C}$.

For a holographic grating with medium modulation [2] $\mu = 0.2$, and a Littrow mounting—where the angle of incidence is equal to the diffracted angle for a chosen mode—we calculated the efficiency for the mode $n = 1$. The predicted efficiency is compared with the one reported experimentally, for a Richardson grating (model 53-220H) (Palmer & Loewen, 2014) as well as validated with MC simulation for one wavelength ($\lambda/\Lambda = 0.52$) and a

[2] $0.15 < \mu = \text{groove height}/\text{groove spacing} < 0.25$

perturbation equal to 1% of the amplitude. Our approach matches very well with the reported data (Fig. 2.5) as well as with the MC simulation. The predicted expected value and standard deviation ($\sigma = \sqrt{\text{Var}}$) are $\mathbb{E}[e_1] = 0.43229$ and $\sigma = 0.01107$, respectively. Meanwhile, the calculated expected value and standard deviation for the MC simulation with a set of 9000 samples are $\mathbb{E}_{MC}[e_1] = 0.43209$ and $\sigma_{MC} = 0.01118$, respectively.

To assess the limitations of our proposed approach, we performed several simulations and compare them with MC (running 2500 samples) for the zero-th mode efficiency (not shown). The variance and mean was obtained using $L = 5$ for both approximations. We found that for medium modulation gratings ($\mu = 0.2$) the error increases as the angle of incidence increases; nevertheless, in all cases the error is less than 1%. On the other hand, the results show that when increasing from medium to high modulation ($\mu = 0.6$) the error also increases. Also, for very deep gratings impinged by small wavelengths, the method fails because the perturbation parameter (fixed as 1% of the amplitude) and the small perturbation assumption, $k\epsilon \sim \epsilon/\lambda \ll 1$, is no longer satisfied.

2.7. Conclusions

A fast deterministic method based on the MoM for simulating TE polarized wave diffraction by randomly perturbed grating surfaces was studied and implemented. Instrumental to this approach is the approximation of the perturbed domain via a shape Taylor expansion. The convergence rate obtained for the mean field by using the MoM and piecewise constant Haar wavelets as basis functions is 1.0. For the second statistical moment, a sparse approximation leads to a system of $\mathcal{O}(N \log N)$ DOFs, while a dense solution is of order N^2. Furthermore, for the dense approximation the rate of convergence is equal to 0.5, while for sparse approximation the convergence rate increases as the number of DOFs increases. Calculations were validated by comparison with FEM and MC simulations; good agreement for the obtained surface densities, mean, and variance of the scattered fields was obtained.

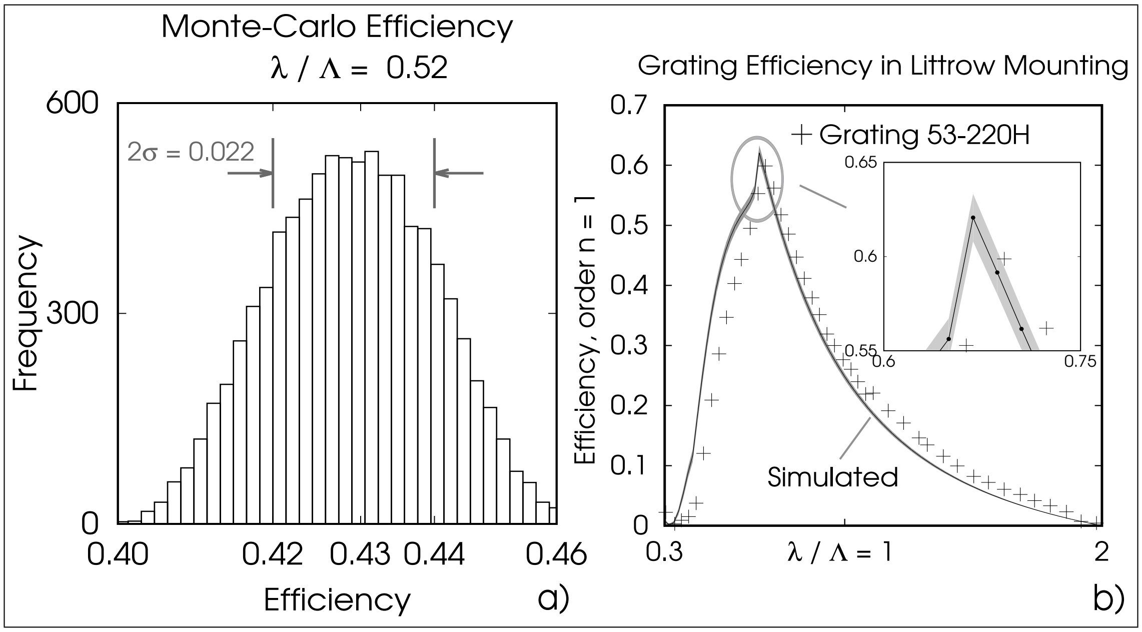

FIGURE 2.5. Efficiency for a sinusoidal grating in Littrow mounting. Histogram for a MC simulation considering $\lambda/\Lambda = 0.52$ (a) and grating efficiency dependence on λ/Λ (b). Theoretical expected value of the grating (continuous line) and the efficiency of a real grating from Richardson (crosses). In the inset, an expanded scale near the peak of the simulated efficiency; the shaded area represents the minimum and maximum values of the standard deviation.

The calculation of the grating efficiency requires the calculation of the surface current density for each wavelength. If the MC method is used to quantify the error produced by shape uncertainty, a large number of sample simulations is required for each wavelength. This generates a huge number of simulations, which leads a tremendous computational cost. In contrast, by using the approach described here, only the solution of the Helmholtz equation and its tensorization for each wavelength is required, reducing the computational cost dramatically. The approach presented in this work can be extended to TM polarization as well as dielectric gratings by considering the associated integral operators and boundary conditions.

3. STUDY OF W/HFO2 GRATING SELECTIVE THERMAL EMITTERS FOR THERMOPHOTOVOLTAIC APPLICATIONS [1]

3.1. Introduction

Thermophotovoltaic (TPV) cells are a promising way to efficiently convert thermal energy into electricity, providing an environmentally-friendly energy source from waste heat or other thermal sources. As just a few examples, TPV cells have been used in solar applications using optical concentration and selective absorbers (Bermel et al., 2016, 2010), portable microgenerators through the incorporation of photonic crystals (W. R. Chan et al., 2015), and hybrid waste-heat converters, combining a TPV cell with solid oxide fuel cells (Liao, Cai, Zhao, & Chen, 2016). The design of TPV cells for a given application is a multi-faceted optimization problem; prior studies include study of the details associated with near-field thermal radiation (Ilic, Jablan, Joannopoulos, Celanovic, & Soljačić, 2012) and global optimization of the system (Nam et al., 2014), as well as experimental development and characterization of TPV devices (Lenert et al., 2014b; Aljarrah, Wang, Evans, Clemons, & Young, 2011; Xu et al., 2014). Detailed reviews of the design and optimization of the key components of TPVs can be found in (Zhou et al., 2016; Pfiester & Vandervelde, 2016) and references therein. TPV cell design relies on two main components: an emitter, which emits thermal radiation at high temperatures, and a photovoltaic (PV) cell that converts this radiation into electricity. Selective emitters are designed to reshape the thermal radiation spectrum, shifting the maximum emittance to a wavelength that matches the absorption characteristics of the PV cell. Since PV cell technology based on semiconductor junctions is mature and well understood, the primary opportunity for further improvement of TPV cell conversion efficiency is the development and optimization of efficient selective emitters.

For conventional TPV cells based on blackbody emission, the emitters must operate at high temperatures. For example, from Wien's displacement law one can see that a blackbody emitter would need to be at 1680 K in order for the peak emittance to match the band gap of a GaSb PV cell ($E_g = 0.72$ eV). For this reason, high melting point materials are required. Consequently, structures built of refractory metals, such as tungsten (Yeng et al., 2012), tantalum (Rinnerbauer et al., 2013), and molybdenum (Zhou et al., 2015) have been proposed and analyzed previously. On the other hand, the use of periodic structures such as metamaterials (Deng et al., 2014; H. Wang et al., 2016) and photonic crystals (Rinnerbauer & Lenert, 2014; Celanovic et al., 2004) has been shown to modify the emittance spectrum of selective emitters. Due to their simplicity and ease of fabrication, gratings are a promising practical option. Chen and Zhang (Y.-B. Chen & Zhang, 2007) studied complex tungsten gratings, and showed that the excitation of surface plasmon polaritons (SPP) can greatly improve the thermal emittance. Nguyen-Huu *et al.* (Nguyen-Huu, Pištora, & Cada, 2016) studied tungsten pyramidal nanogratings that combine structures with low and high filling ratios. This combination was shown to improve the emittance as well as to reduce the sensitivity to the angle of incidence for transverse magnetic (TM) polarization. Song *et al.* (Song, Wu, Cheng, & Zhao, 2015) proposed trilayer metal-insulator-metal (MIM) gratings made of W-SiO_2-W, and Shuai *et al.* (Shuai, Tan, & Liang, 2014) studied more general multilayer metal-dielectric gratings. In both (Song et al., 2015) and (Shuai et al., 2014), perfect emittance at the design wavelength was achieved for TM polarization, through the excitation of SPPs and magnetic polaritons (MP). To achieve improved polarization insensitivity, Nguyen-Huu *et al.* (Nguyen-Huu et al., 2012) evaluated a deep grating that takes advantage of Wood's anomalies (WA) (Erwin G. Loewen & Popov, 1997), cavity resonances (CR), and SPPs. Recently, multilayer W-HfO_2 metamaterial structures have been shown to enable thermal emission control through topological transitions (Dyachenko et al., 2016). In addition, Yeng *et al.* (Yeng et al., 2014) filled a 2D tantalum photonic crystal with SiO_2 or HfO_2, and obtained omnidirectional and polarization insensitive thermal emitters by exploiting CRs. The HfO_2 dielectric in these structures appears promising for TPV applications due to its high melting point (3031 K).

As noted above, both SPPs and MPs have been used to manage and improve the thermal emittance. However, these improvements are only obtained for TM–polarized incident radiation. For general TPV applications, the incident radiation is randomly polarized, and thus both the transverse electric (TE) and TM response are important. However, the strategies used for TM emittance control are not effective for TE; instead, for TE polarization, CRs are required to enhance the thermal emittance. Unfortunately, for gratings able to excite both SPPs and CRs (Nguyen-Huu et al., 2012), the wavelength associated with the emittance peak is typically close to the visible range (0.4–0.8 μm), which translates to very high operating temperatures. Therefore, in order to improve thermal emitters and make them suitable for infrared TPV applications, it is necessary to develop strategies to enable efficient TPV operation at lower emitter temperatures.

In this work, we explore simple structures combining the use of a thin HfO_2 spacer and deep W gratings to achieve high emittance at technologically relevant temperatures. We show that a grating with an embedded HfO_2 layer supports both SPPs and MPs, while the deep grating grooves allow the excitation of CRs. By using rigorous coupled wave analysis (RCWA), two kinds of gratings have been studied. First, a shallow grating designed to excite MPs is evaluated. A peak emittance of 99.9% for $\lambda = 1.73$ μm is obtained for the case of TM polarization, but the performance with TE radiation is appreciable lower. To improve on this performance, a deeper grating that supports CRs is evaluated for TE waves. It is found that by the simultaneous excitation of SPPs, MPs, and CRs it is possible to reach normal thermal emittances of 97.7% and 99.7% for TE and TM waves, respectively, at wavelengths close to $\lambda = 1.65$ μm. These gratings are promising for use with low bandgap PV cells, such as GaSb (0.72 eV) and $In_{0.53}Ga_{0.47}As$ (0.75 eV).

3.2. Emitter Design

Hafnia is a high permittivity oxide that has favorable properties for use in selective emitters. HfO_2 has a very high refractive index ($n \sim 4$) for short wavelengths, and remains almost constant, close to $n = 2$, for wavelengths $\lambda > 0.4$ μm. Moreover, the absorption coefficient—which is related to the imaginary part of the index of refraction—is negligible in the optical and near-IR where TPV systems can be expected to operate (Padma Kumar et al., 2015). In addition, hafnia has a large energy bandgap ($E_g \sim 6$ eV) and, critically for thermal emitters, possesses a very high melting point, 3031 K, which translates to good thermal stability (Kar, 2013). Moreover, its thermal expansion coefficient is compatible with W (Knibbs, 1969)—a key factor when operating at high temperatures. Recently, hafnia layers have been deposited onto photonic crystals to prevent degradation when operated at high temperatures (?, ?; Lee et al., 2013; Stelmakh, Chan, Joannopoulos, Soljacic, & Celanovic, 2016), providing experimental validation of its promise for high temperature applications.

The gratings evaluated here consist of a tungsten substrate, a hafnia spacer layer, and a tungsten grating similar to the structure proposed by Wang and Zhang (L. P. Wang & Zhang, 2012). In addition, to help clarify the physics of operation, a W grating without a HfO_2 spacer layer has also been simulated for comparison. To simulate the selective emitter explored here, Helmholtz's equation is solved by using the RCWA method (Zhang, 2007; Moharam & Gaylord, 1981) in order to find the reflectance (ρ) and transmittance (τ). The absorptance (α) is calculated indirectly by energy conservation using $\alpha = 1 - \rho - \tau$. Finally, the emittance is obtained through Kirchhoff's law, which states that in thermal equilibrium the absorptance is equal to the emittance ($\alpha = \varepsilon$) (Zhang, 2007). To obtain more realistic estimations of thermal emittance for selective emitters operating at high temperatures, we considered a temperature dependent Drude model for tungsten (Minissale, Pardanaud, Bisson, & Gallais, 2017; Alabastri et al., 2013). The properties of HfO_2 are taken from (Padma Kumar et al., 2015). In addition, both the electric and magnetic fields inside the structures are obtained by using the finite element method (?, ?). Two gratings with the same geometry except for their height have been evaluated. First, a shallow grating with a period $\Lambda = 1.1$ μm, thickness $h = 0.1$ μm, and a filling factor $f = w/\Lambda = 0.2$ (with a distance between ridges $a = 0.88$ μm) above a hafnia layer of thickness $d = 0.15$ μm was considered (inset Fig. 3.1(a)). As shown in Fig. 3.1(a), simulations of this structure result in nearly perfect normal emittance, 99.9%, for TM incident radiation. The incorporation of a hafnia spacer significantly improves the emittance, generating a peak at $\lambda = 1.73$ μm, due to MP excitation as explained by the concentration of the magnetic field (Fig. 3.1(b)). However, the emittance in response to TE radiation is modest, with a peak emittance that is both blueshifted to $\lambda = 1.255$ μm, as well as being appreciable lower, close to 88.13%. However, as can be seen in the comparison in Fig. 1(a), the TE and TM responses of the W/HfO_2/W structure are much better than that of a plane W grating.

To develop a polarization–insensitive selective emitter, a deep grating with $\Lambda = 1.1$ μm, $h = 1.0$ μm, $f = 0.2$, $a = 0.88$ μm, and $d = 0.15$ μm, is considered (inset Fig. 3.2(a)). This deep grating produces an emittance peak of 97.7% for TE radiation at $\lambda = 1.614$ μm and 99.7% for TM waves at $\lambda = 1.674$ μm, thereby demonstrating that the polarization sensitivity can be greatly reduced by using the deep grating design in combination with the HfO_2 spacer.

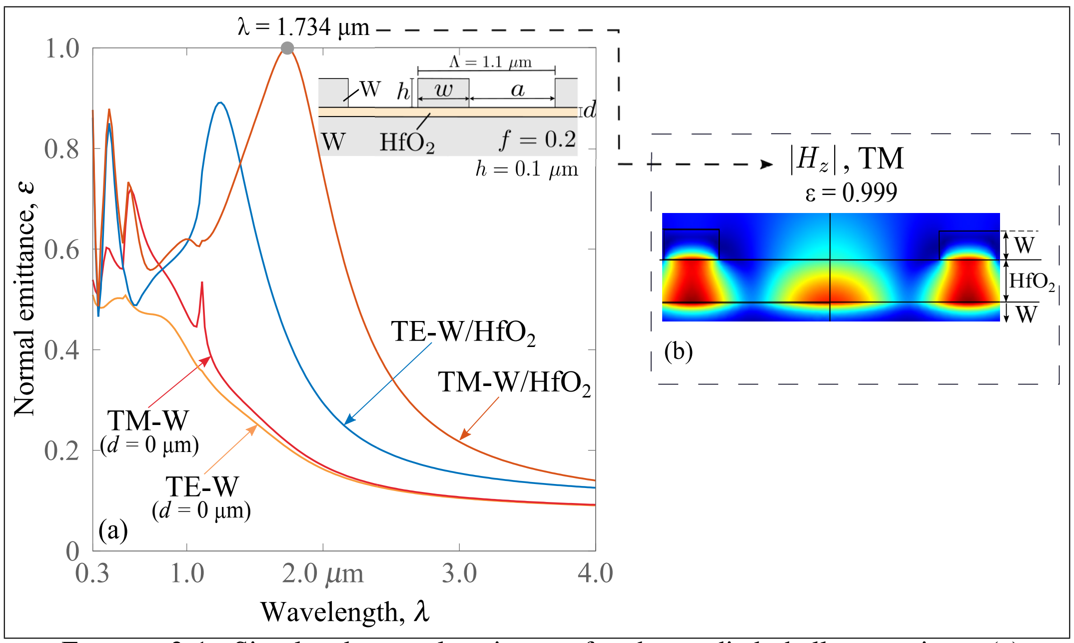

FIGURE 3.1. Simulated normal emittance for the studied shallow grating. (a) Emittance for both TE and TM polarizations for W gratings with and without hafnia spacer layers. The inset shows the geometry of the structure. (b) Magnetic field strength for $\lambda = 1.73$ μm.

To understand the physical origins of these results, we note that it is well-known that metallic gratings can excite SPPs for TM polarization. This excitation is given by the collective oscillation of electrons and photons, due to the perpendicular component of the electric field. On the other hand, for TE incident radiation, the tangential component of the

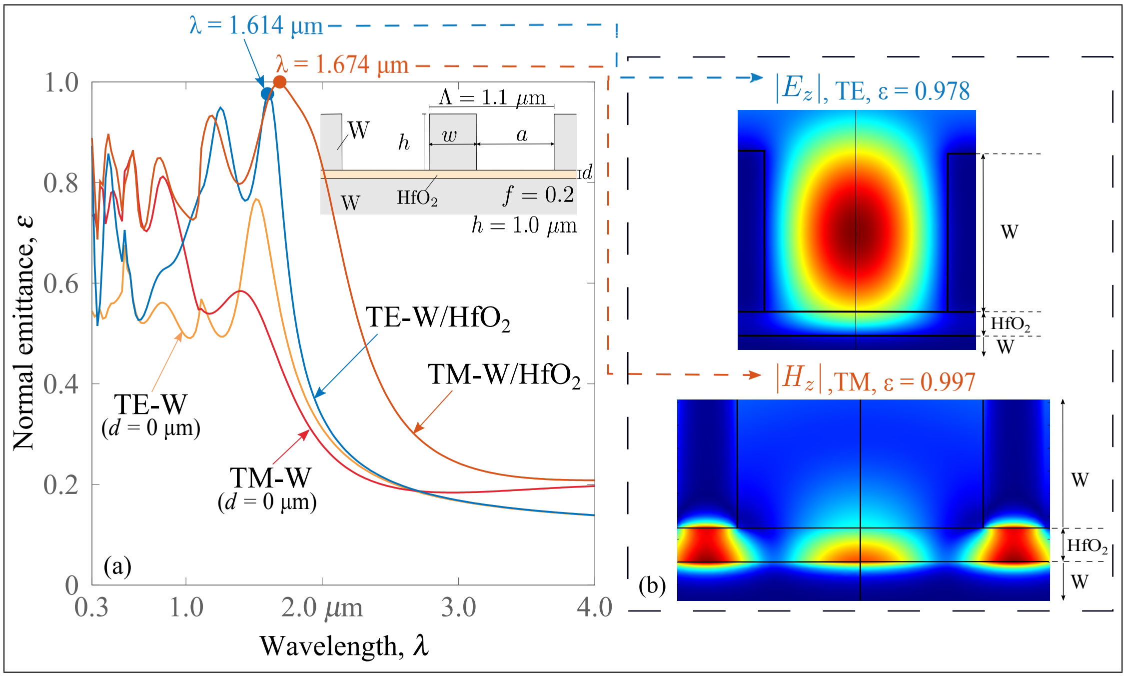

FIGURE 3.2. Simulated normal emittance for the studied deep grating. (a) Emittance for both TE and TM polarizations for W gratings with and without hafnia spacer layers. The inset shows the geometry of the structure. (b) Electric field magnitude for $\lambda = 1.614$ μm and the magnetic field magnitude for $\lambda = 1.674$ μm.

electric field must vanish on the surface (Maier, 2008), and therefore no surface polarization can be produced. For this reason, design of a polarization-insensitive selective emitter requires the use of different mechanisms to control the thermal radiation in each polarization. For TE radiation, CRs in deep gratings are an attractive option. These resonances can be predicted by $\lambda_{mn} = 2/\sqrt{(m/h)^2 + (n/a)^2}$, where by choosing $m = 0$ and $n = 1$ we obtain a maximum wavelength $\lambda_{01} = 2a$ (Borisov, García De Abajo, & Shabanov, 2005). The SPP excitation can be predicted by using the dispersion relation for a metal-dielectric interface, together with momentum conservation $k_x = k_{spp}(\omega) + jK$, where k_x is the horizontal component of the wavevector, $k_x = (2\pi/\lambda)\sin\theta_i$, $k_{spp} = (2\pi/\lambda)\sqrt{\varepsilon_m\varepsilon_d/(\varepsilon_m + \varepsilon_d)}$ is the wavenumber of the surface wave, $K = 2\pi/\Lambda$ is the grating momentum, and j is an integer (Nguyen-Huu et al., 2012). By including a dielectric spacer below the grating, MPs are generated as a result of the coupling between internal and external SPPs (Xuan & Zhang, 2014).

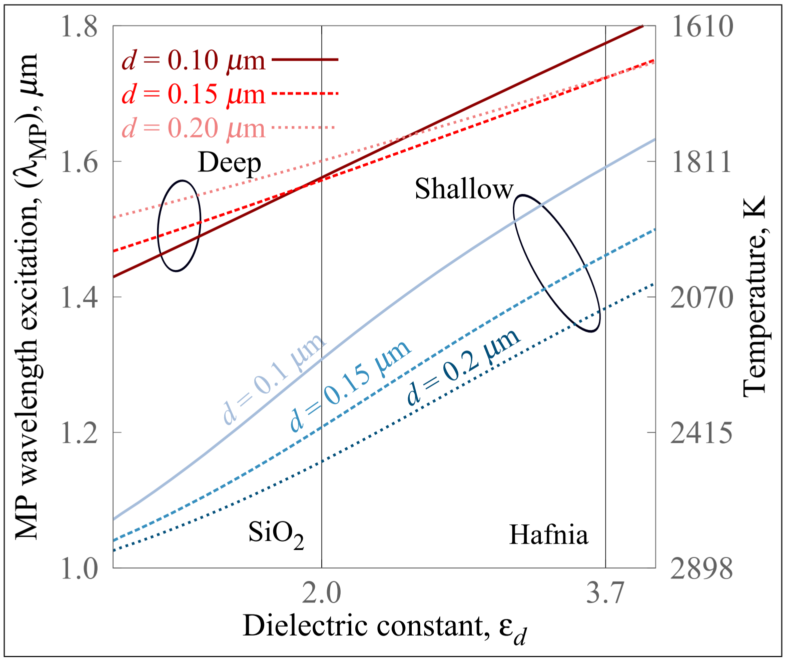

FIGURE 3.3. Excitation wavelength for MPs (λ_{MP}) as a function of spacer dielectric constant for both shallow (blue) and deep (red) gratings, for several spacer thicknesses.

As noted above, the incorporation of a dielectric layer enables the excitation of MPs. Moreover, by using an LC circuit model (L. P. Wang & Zhang, 2012) to predict the excitation wavelength of the MPs (λ_{MP}), it can be shown that when the dielectric constant of this layer is high, as is the case of HfO_2, MPs can be excited at longer wavelengths which allows for lower working temperatures. Figure 3.3 illustrates these trends for deep and shallow gratings as a function of the spacer permittivity.

Regarding the polarization-insensitive deep gratings, emittance enhancement results from the simultaneous excitation of CRs, SPPs, and MPs. By combining these three effects, emittance is improved for wavelengths larger than 1.6 μm for both TE and TM polarizations (Fig. 3.2(a)). The peak for TE polarization at $\lambda = 1.614$ μm (highlighted with the blue dot in Fig. 3.2(a)) is due to CRs as predicted by the slab waveguide cut-off for the TE_{10} mode, λ_{10} (Borisov et al., 2005); as shown in Fig. 3.2 (b), the waveguide mode concentration of the electric field at resonance produces an increase in the absorptance. On the other hand, to understand the phenomena that enhance the emittance in the near IR frequency range, we find that the emittance peak at $\lambda = 1.14$ μm for TM polarization is generated by the excitation of SPPs, according to momentum conservation for radiation in free space above the grating. The emittance peak at $\lambda = 1.674$ μm is due to the excitation of MPs as can be inferred from the long-wavelength TM peak (highlighted by the orange dot in Fig. 3.2(a)). As shown in Fig. 3.2(b), the magnetic field at that wavelength is concentrated in the hafnia layer.

The angular dependence of the directional emittance is presented for both polarizations in Fig. 3.4. For TE incident radiation, the emittance is close to one up to an angle of $\theta = 30°$, but decreases abruptly at larger angles. For the TM case, the emittance peak redshifts from 1.674 μm to 2.47 μm and it is reduced from 99.7% to 58.9% as the angle increases to $\theta = 60°$. The dependence on the angle of incidence is detrimental to the efficiency of a TPV cell, due to the fact that thermal emission is an hemispherical property. Ideally, the structure should present high emittance over as large a range of angles as possible, as well as to maximize the peaks for both TE and TM polarizations.

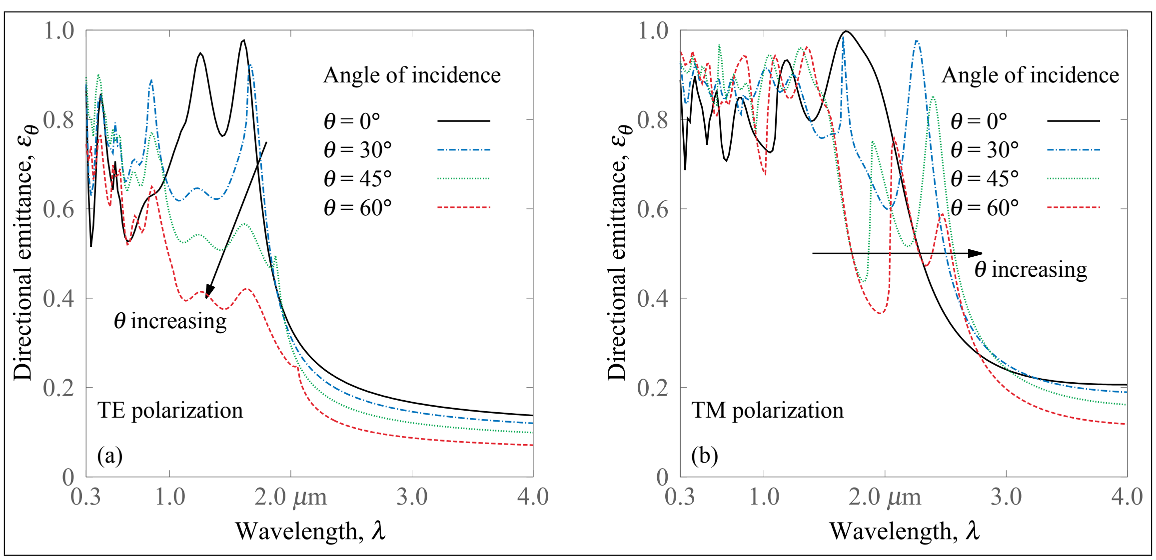

FIGURE 3.4. Directional emittance of the deep grating as a function of the angle of incidence. (a) and (b) show the emittance for different angles of incidence ($\theta = 0°$, $30°$, $45°$, and $60°$) for TE and TM polarizations, respectively.

To evaluate the efficiency performance of the selective emitters, we consider the normal in-band emittance (ϵ_{in}) (Stelmakh et al., 2016) given by:

$$\epsilon_{in,i}(T) = \frac{\displaystyle\int_0^{\lambda_g} \varepsilon_i(\lambda) E_b(T,\lambda) d\lambda}{\displaystyle\int_0^{\lambda_g} E_b(T,\lambda) d\lambda}, \quad i = \text{TE, TM}, \tag{3.1}$$

where $E_b = 2hc^2/[\lambda^5(e^{hc/\lambda k_b T} - 1)]$ is the blackbody thermal radiation, c is the speed of light, h is the Planck's constant, and k_b is the Boltzmann constant. $\varepsilon(\lambda)$ is the normal emittance for either TE or TM polarizations (or denoted as a subscript i =TE, TM). Figure 3.5 shows the normal radiated power for both the shallow grating (Fig. 3.5(a)) and the deep grating (Fig. 3.5(b)). The in-band emittance for the shallow grating in the case of TM polarization, $\epsilon_{in,TM}$, is 77.04%, while as noted above the emittance in response to TE radiation is lower; the normal in-band emittance, $\epsilon_{in,TE}$, is 67.26%. In contrast, for the deep grating case we obtained $\epsilon_{in,TM} = 85.17\%$ and $\epsilon_{in,TE} = 82.25\%$, thereby demonstrating the performance potential of this structure. These in-band emittances were calculated by using $\lambda_g = 1.72$ μm and $\lambda_g = 1.65$ μm for the shallow and deep gratings, respectively, in order to match the thermal radiation peak with the emittance peak obtained for TM radiation. Regarding the operating temperature, the peaks for shallow and deep gratings are approximately 1680 K and 1750 K, respectively. Given the peaks for both shallow and deep gratings, they match well with GaSb (0.72 eV) and $In_{0.53}Ga_{0.47}As$ (0.75 eV) PV cells, respectively.

The in-band polarization–averaged hemispherical emittance was also calculated. For the shallow grating a modest in–band hemispherical emittance of $\epsilon_{in,h} = 57.63\%$ was obtained; the value is low because the performance of the TE radiation is poor. In the case of the deep grating an in–band hemispherical emittance of $\epsilon_{in,h} = 67.66\%$ was achieved. This value is lower than the normal in–band emittance due to the fact that the CRs start disappearing for $\theta > 45°$ and, in the case of TM radiation, the peak is red shifted for wavelengths larger than the bandgap of the PV cell.

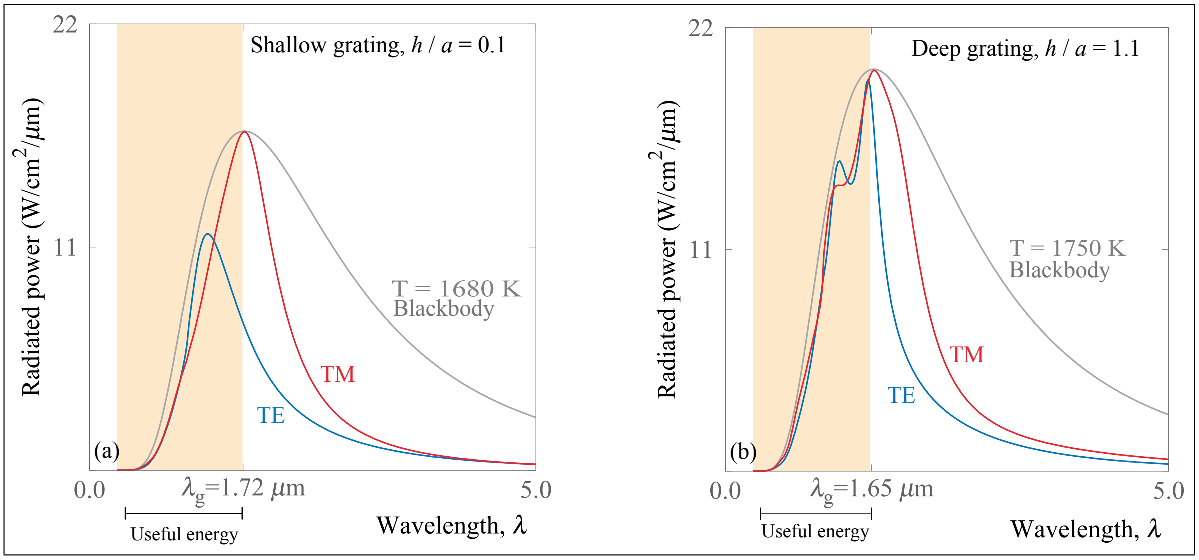

FIGURE 3.5. Thermal radiation for (a) shallow and (b) deep gratings at $T = 1680$ K and $T = 1750$ K, respectively. The blackbody thermal radiation is shown for comparison. An in-band emittance of 88.25% and 85.17% is achieved for the deep gratings for TE and TM polarization, respectively.

3.3. Conclusion

Gratings based on W with and without HfO_2 spacer layers have been explored through numerical simulations. We see that use of an HfO_2 layer can improve the performance of tungsten grating-based selective thermal emitters. The use of shallow gratings results in a maximum emittance of 99.9% at $\lambda = 1.73$ μm, but with appreciable lower TE performance. To improve the polarization insensitivity, a deep grating was investigated. The deep grating exhibits emittance peaks of 97.7% and 99.7% for TE and TM radiation, respectively. The mechanisms responsible for the improvement in the emittance have been explored; it was found that for TM radiation SPPs and MPs play a crucial role, while for the case of TE polarization, CRs are responsible for the high emittance. The peak emittance wavelength for both polarizations, close to $\lambda = 1.65$ μm, requires a working temperature of approximately 1750 K. Both tungsten and hafnia can operate up to this temperature due to their high melting points and material compatibility. The performance of the emitters was evaluated by the normal in-band emittance, obtaining $\epsilon_{in,TM} = 85.17\%$ and $\epsilon_{in,TE} = 82.25\%$ for the deep grating case. In addition, we estimated the hemispherical in–band emittance. The shallow and deep gratings exhibit hemispherical in–band emittances of 57.63% and 67.66%, respectively. The results show that deep gratings with a high dielectric constant spacer are promising alternatives for TPV applications, whose performance can be improved by further optimization.

4. HIGH-TEMPERATURE TUNGSTEN-HAFNIA OPTIMIZED SELECTIVE THERMAL EMITTERS FOR THERMOPHOTOVOLTAIC APPLICATIONS[1]

4.1. Introduction

Thermophotovoltaic (TPV) energy conversion has emerged as a promising approach for harvesting energy from a range of heat sources. For example, recycling waste energy from industrial processes (Utlu & Önal, 2018), conversion of energy from solid oxide fuel cells (Liao et al., 2016), and capture of long-wavelength solar energy are all possible applications of TPV cells (H. Wang et al., 2016; Chirumamilla et al., 2017). The design of a conventional TPV cell relies on two main components: an emitter and a photovoltaic (PV) cell. Careful design of these components is critical to maximize the TPV performance. Among the components of a TPV cell, the emitter is the most amenable to optimization, since reshaping the thermal radiation emission spectrum, significantly enhance performance. Since the radiation from the emitter is captured by the PV cell, it is important to match the emitters radiation spectrum to the optical response of the PV cell. This leads to high emitters temperatures for practical PV cells; for an emitter to match a GaSb PV cell ($E_g = 0.72$ eV), an operating temperature of approximately 1700 K is needed.

Since selective emitters for TPVs must operate at high temperatures, high melting point materials are required. Additionally, to optimize the match between the power spectrum radiated by the emitter and the optical response of the PV cell, several physical phenomena such as surface plasmon polaritons (SPP), magnetic polaritons (MP), and cavity resonances (CR) have been investigated. For example, high temperature tantalum (Ta) and tungsten (W) 2D photonic crystals that exploit CRs have been studied to enhance hemispherical thermal emittance (Nam et al., 2014; Yeng et al., 2014; Chou et al., 2013). In addition, Stelmakh *et al.* studied a 2D photonic crystal with a HfO_2 coating, where it was shown that using a Ta-W alloy enhanced thermo-mechanical properties at high temperatures (Stelmakh et al., 2013). As an alternative to photonic crystals that require high-resolution patterning, planar multilayer stacks made of refractory metals and dielectrics have also been studied numerically and experimentally. For example, asymmetric multilayer stacks of ultra-thin metal-dielectric layers exhibit emittance peaks for both transverse electric (TE) and transverse magnetic (TM) polarizations (Fu, Zhong, Tu, Chen, & Lin, 2016). In this context, metal-insulator-metal (MIM) resonator structures made of W-Al_2O_3-W with an Al_2O_3 protective coating (PC) has been shown to exhibit omnidirectional emittance, polarization-insensitivity, and thermal stability up to temperatures of 1073 K (Chirumamilla et al., 2016). Furthermore, Kim *et al.* investigated W-SiO_2 multilayers, proving that this structure is thermally stable up to 1300 K (Kim, Jung, & Shin, 2017). One-dimensional periodic structures (gratings) made of tungsten (Y.-B. Chen & Zhang, 2007; Nguyen-Huu et al., 2016) or combinations of metallic gratings with dielectric layers (Song et al., 2015; L. P. Wang & Zhang, 2012; Song, Si, Cheng, & Luo, 2016; Shuai et al., 2014; Silva-Oelker, Jerez-Hanckes, & Fay, 2018) have also been intensively studied since they are able to exploit SPPs and MPs, obtaining peaks of near perfect emittance, albeit under resonant conditions. Moreover, high emittance has also been achieved using topological transitions and epsilon-near-zero metamaterials (Dyachenko et al., 2016; Molesky, Dewalt, & Jacob, 2013).

The optimal design for a selective emitter should exhibit high emittance for wavelengths shorter than the one associated with the bandgap of the PV cell ($\lambda < \lambda_g = hc/E_g$), while at the same time having a low emittance for wavelengths longer than the bandgap ($\lambda > \lambda_g$). Previously, Nguyen-Huu *et al.* (Nguyen-Huu et al., 2012) used a genetic algorithm (GA), minimizing a cost function given by the squared error between the structure emittance and an ideal emittance profile to obtain an optimized structure. Similarly, Ghanekar *et al.* (Ghanekar et al., 2017) used a GA and a cost function based on the maximization of the TPV cell output power while limiting waste heat to optimize SiO_2/W gratings with periodicity in one and two dimensions. Yeng *et al.* (Yeng et al., 2014) optimized two-dimensional tantalum structures filled with hafnia by using a multi-level single-linkage method, ultimately obtaining a high hemispherical thermal emittance of nearly 90% for the wavelength range of operation.

While remarkable progress has been achieved in the design of thermal emitters, the most promising structures reported to date rely on complex fabrication techniques, making them difficult to implement in practice. Common challenges include requiring small features that require advanced lithography, or with resulting structures sensitive to either the angle of incidence or polarization.

In this work, two different types of MIM structures with the explicit goal of obtaining high performance while also minimizing fabrication challenges have been explored. The devices consist of a W-HfO_2-W stack and a top hafnia layer that induces resonances, while also acting as a protective coating. These structures are designed to operate at high temperatures and provide high hemispherical thermal emittance. Two structures have been put forward (see Figure 4.1). The first structure is a simple multilayer stack, while the second is a linear one-dimensional grating combined with a multilayer structure. The optimization of the emitters is carried out by using a GA (MATLAB Optimization Toolbox, 2017) coupled to rigorous coupled wave analysis (RCWA) for the emittance calculation (Moharam & Gaylord, 1981). Based on a two-band model (Chubb, 2007)—in which a gray-body emitter is combined with a filter—the GA adjusts the geometrical parameters of the emitter to make it closely track the emittance of an ideal selective emitter. Then, to evaluate the overall effectiveness of the emitter design for TPV applications, the output power and TPV conversion efficiency have been calculated. In these calculations, the measured characteristics of a GaSb PV cell are combined with a GaSb optimized filter (O'Sullivan et al., 2005) (i.e., a filter that reflects photons with energies below the PV cell bandgap) and an energy balance between the emitter and the PV cell. In this way, both the in-band and out-of-band response of the emitter, and realistic properties of the intended PV cell are included in the performance projections. In addition, a sensitivity analysis was also carried out to determine the robustness of the design to manufacturing variation. Wide tolerances on layer thickness can be acceptable in the case of the grating emitter; while changing the nanometer-scale W layer thickness by 150 % results in almost no change (less than 1 %) in either output power or efficiency.

4.2. Design and optimization

Figure 4.1 depicts the two structures considered. For the planar multilayer stack (Fig. 4.1(a)), the thermal emittance is controlled primarily by the thicknesses of the hafnia layers (h_1 and h_3 in Fig. 4.1(a)); the thin W interlayer only weakly influences the performance. On the other hand, for the grating-based structure in Fig. 4.1(b), the emittance is governed by not only the thicknesses of the hafnia layers, but also the grating period (Λ), the grating filling ratio ($f = w/\Lambda$), and the tungsten thickness (h_2).

4.2.1. Thermal emitter design and optimization

A theoretical ideal thermal emitter would emit only photons with energy equal to the bandgap of the PV cell in order to maximize conversion efficiency. However, such a monochromatic emitter is impossible to realize in practice, and physically-realizable narrow-band emitters typically operate with high performance only in specific directions (i.e., they exhibit strong polarization or angle of incidence dependence). In this work, the evaluation of the TPV performance is based on the *two-band model* (Chubb, 2007), in which a gray-body emitter with a reflective highpass filter between the emitter and the PV cell is used to maximize the performance of the TPV cell. For this TPV cell architecture, a thermal emitter that follows the trend of the ideal one exhibits high hemispherical emittance for wavelengths shorter than the bandgap of the PV cell ($\lambda < \lambda_g$) and minimizes emittance otherwise ($\lambda > \lambda_g$). Such a cell maximizes performance because the emitter promotes the generation of photons that are able to generate current in the PV cell, while the filter reflects back all the photons below E_g that are inevitably generated by the emitter and that would otherwise be wasted.

In addition, due to the high operating temperatures required for the emitters, materials used in their design require high melting points (T_m). For this reason, tungsten ($T_m = 3695$

K) as the metal and hafnia ($T_m = 3031$ K) as the dielectric have been considered. Another advantage of both tungsten and hafnia is their thermal expansion compatibility (Knibbs, 1969)—an important consideration when operating at high temperatures.

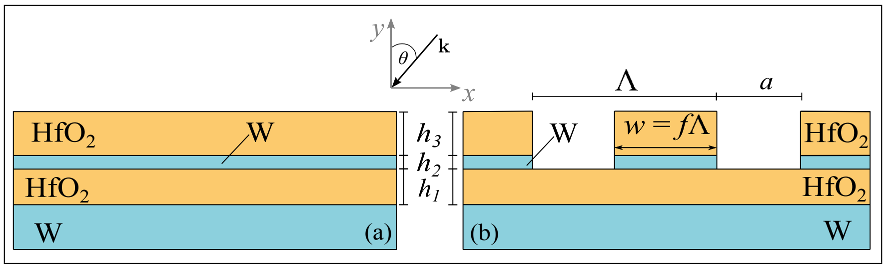

FIGURE 4.1. Structures under study. h_1, h_2, and h_3 are the thicknesses of the hafnia (orange) spacer, the tungsten layer (blue) and the hafnia top layer, respectively. In addition, an optically thick tungsten substrate is assumed. (a) planar multilayer stack structure, (b) grating with a fill factor f, period Λ, and width $w = f\Lambda$.

To estimate the emitter performance, directional emittance is computed by using RCWA. This method calculates the transmittance (τ) and reflectance (ρ) by using a decomposition of the fields into Fourier modes. Once the transmittance and the reflectance are obtained, the absorptance (α) is calculated indirectly by an energy balance: $\alpha = 1 - \tau - \rho$. Then, employing Kirchhoff's law of thermal radiation, the emittance (ε) of the structure is obtained. To model the dielectric constant for W, a temperature dependent Lorentz-Drude model with several oscillators was used (Minissale et al., 2017; Alabastri et al., 2013):

$$\varepsilon_r(\omega, T) = 1 - \frac{f_0 \omega_p^2(T)}{\omega(\omega - \imath\Gamma_0(T))} + \sum_{j=1}^{N} \frac{f_j \omega_p(T)^2}{(\omega_j^2 - \omega^2 + \imath\omega\Gamma_j)}, \tag{4.1}$$

where T is the temperature, ε_r is the relative permittivity, N is the number of oscillators with frequency ω_j, strength f_j and f_0, damping constants Γ_j and Γ_0 (associated with a lifetime $1/\Gamma$), and ω_p is the plasma frequency.

The hemispherical emittance is given by

$$\varepsilon(\lambda) = \frac{1}{\pi} \int_0^{\pi/2} \int_0^{2\pi} \varepsilon'(\lambda, \theta, \phi) \cos(\theta) d\Omega, \tag{4.2}$$

where $d\Omega = \sin(\theta)d\theta d\phi$ is the solid angle, ε' is the directional emittance, and $\cos(\theta)$ represents Lambert's cosine law. By symmetry, the emittance of the multilayer structure is insensitive to polarization and azimuthal angle (ϕ). As a consequence, the hemispherical emittance of the multilayer stack can be obtained as a function of the polar angle (θ) by averaging both the TE and TM polarizations, eq.(4.3). Due to the fact that the gratings are periodic in only one dimension, the emittance can also depend on ϕ. However, it has been shown that for omnidirectional gratings—as is the case of the grating structure optimized in this work—the ϕ dependence is negligible (Herv, Drvillon, Ezzahri, & Joulain, 2018; Marquier, Laroche, Carminati, & Greffet, 2007; Marquier, Arnold, Laroche, Greffet, & Chen, 2008). Therefore, the same simplified form used for the multilayer can be used for the grating emitter:

$$\varepsilon(\lambda) = \int_0^{\pi/2} [\varepsilon'_{TE}(\lambda, \theta) + \varepsilon'_{TM}(\lambda, \theta)] \cos(\theta) \sin(\theta) d\theta, \tag{4.3}$$

where $\varepsilon'_{TE}(\lambda, \theta) = \varepsilon'(\lambda, \theta, \phi = 0)$ and $\varepsilon'_{TM}(\lambda, \theta) = \varepsilon'(\lambda, \theta, \phi = \pi/2)$. This simplification improves the speed of the optimization algorithm since for each evaluation of the cost function it is only necessary to integrate the sum of the TE and TM polarization over the polar angle θ. Although the azimuthal dependence for the grating emittance is weak, differences in emittance due to polarization can be very strong. Therefore, the exploitation of different physical phenomena, such as SPPs, Fabry-Perot (FP) resonances, or CRs for each polarization are required to enhance thermal emittance.

4.2.2. Optimization

A GA (MATLAB Optimization Toolbox, 2017) along with RCWA was used to optimize the geometry of the emitters. The GA starts with an initial population and performs three fundamental operations: selection, crossover, and mutation. These operations enable extraction of the best "genes" (crossover) and add diversity to a population to increase the probability of finding an optimum value of the cost function (mutation) (MATLAB Optimization Toolbox, 2017; Goldberg, 1989). For the optimization reported here, a population size of 300, based on a stochastic uniform selection, and crossover = 0.1 was used. In addition, the cost function, $E(T)$, is taken as the L^2-norm of the difference between the hemispherical emittance (obtained using eq. (4.3)) and the ideal hemispherical emittance ($\varepsilon_{ideal} = 1$ for $0 < \lambda < \lambda_g$ and $\varepsilon = 0$ otherwise, with λ_g corresponding to the GaSb PV cell bandgap ($\lambda_g = 1.72\ \mu$m)).

$$E(T) = \int_0^\infty |\varepsilon(\lambda, T) - \varepsilon_{ideal}(\lambda, T)|^2 d\lambda. \tag{4.4}$$

To ensure the GA converges to physically meaningful solutions, the thicknesses of the hafnia layers were limited to be below quarter wavelength, and the W interlayer was limited by the skin depth (at $\lambda \sim 1.5\ \mu$m). Same thickness constraints were used for the grating design, constraining the period to be below $\lambda_g/2$ to minimize diffraction losses (Yeng et al., 2014).

4.2.3. Efficiency and performance

For the designs reported here, a GaSb PV cell was assumed. To evaluate the performance of the overall TPV cell (i.e., emitter, filter, and PV cell), the output power and TPV efficiency were obtained using an energy balance between the emitter and the cell by assuming no losses (radiative, convection, etc.). The power per unit area incident on the filter, $q_{i,c}$, is given by:

$$q_{i,c}(\lambda, T_e) = \frac{\varepsilon_e(\lambda) E_{b,e}(\lambda, T_e)}{1 - \rho_e(\lambda)\rho_c(\lambda)}, \tag{4.5}$$

where the energy emitted from the PV cell has been neglected since its temperature is much lower than the emitter temperature ($T_{pv} = 300$ K $\ll T_e = 1680$ K). In (4.5),

$$E_{b,e}(\lambda, T_e) = 2\pi hc^2/[\lambda^5(e^{hc/\lambda k_b T_e} - 1)]$$

is the blackbody emissive power at the emitter temperature, with c being the speed of light and k_b is the Boltzmann constant. In addition, ρ_e and ρ_c are the reflectance of the emitter and the cell. The cell reflectance (normal and hemispherical) was obtained based on a Si/SiO_2 multilayer filter structure, which has been optimized for GaSb PV cells (O'Sullivan et al., 2005) in order to pursue a two-band optimum design. The hemispherical emittance of the emitter, ε_e, is obtained using (4.3). Realistic parameters for the PV cell were used

(Bett & Sulima, 2003). The output power density per unit area from the PV cell is

$$\frac{P_{out}}{A} = FFV_{oc}J_{sc}(T_e), \tag{4.6}$$

where FF is the fill factor and V_{oc} is the open-circuit voltage (Bett & Sulima, 2003). J_{sc} is the short-circuit current density, given by

$$J_{sc}(T_e) = e\int_0^\infty \frac{q_{i,c}(\lambda, T_e)\eta_{EQE}(\lambda)\lambda d\lambda}{hc}, \tag{4.7}$$

where η_{EQE} is the external quantum efficiency. The total energy flux entering into the emitter can likewise be calculated from the emitter and cell properties using:

$$Q_{th}(T_e) = \int_0^\infty (1-\rho_c(\lambda))q_{i,c}(\lambda, T_e)d\lambda. \tag{4.8}$$

Finally, the conversion efficiency of the TPV cell can be obtained by using

$$\eta_{TPV}(T_e) = \frac{P_{out}(T_e)}{Q_{th}(T_e)}. \tag{4.9}$$

4.3. Results and discussion

4.3.1. Hemispherical and directional emittance

Used of the GA resulted in determination of the optimal geometry for the two proposed structures. It was found that the optimum planar multilayer emitter design consists of $h_1 = 0.0342$ μm, $h_2 = 0.0072$ μm, and $h_3 = 0.1070$ μm. Similarly, for the grating selective emitter, the optimum design is $h_1 = 0.08702$ μm, $h_2 = 0.0440$ μm, $h_3 = 0.1598$ μm, $\Lambda = 0.5032$ μm, and $f = 0.3548$. Figure 4.2 shows a comparison of the normal and hemispherical emittance (Fig. 4.2 (a) and (b), respectively) for both the planar and grating emitter. For reference, the emittance of a planar W emitter, as well as the ideal emittance, and the Si/SiO_2 bandpass filter reflectance considered in the design (O'Sullivan et al., 2005) are also shown. Since the emittance in gratings is sensitive to polarization, both TE and TM polarizations are shown in Fig. 4.2 (a). It can be seen that in the case of the grating emitter the TM normal emittance is high, above 99%, for wavelengths between 0.82 to 1.28 μm; however, the TE normal emittance is lower with a peak of 84% close to $\lambda = 1.0$

μm. On the other hand, the planar multilayer stack's normal emittance is also high with a peak of 91% close to $\lambda = 1.1$ μm. The filter normal emittance has also been plotted to highlight the portion of the emittance that is reflected back to the emitter. Of more direct relevance to TPV operation, however, is the hemispherical emittance. Figure 4.2(b) shows hemispherical emittances of 88% and 91% for both the multilayer and grating structures close to $\lambda = 1.0$ μm, respectively. The high hemispherical emittance indicates that the emittance does not strongly depend on θ. To explore this in more detail, the directional emittance for both designs as a function of the angle of incidence was computed. Figure 4.3 shows the angle of incidence dependence in the case of the planar multilayer structure. This emitter presents presents very high peak emittance (above 90 %) for $\theta \leq 60°$ for both TE and TM polarizations. For the grating emitter case the angle dependence is more complex, as illustrated in Fig. 4.4. Resonances within the grating structure give rise to the peaks and troughs seen in Fig. 4.4. For TE polarization, a very high peak emittance (above 80 %) up to $\theta = 80°$ is obtained close to $\lambda = 1.1$ μm. The TM polarization emittance is also very high and presents a broader passband; however, it decreases abruptly between $\theta = 60°$ and $80°$. Table 4.1 summarizes the output power and the projected TPV efficiency for the structures proposed in this work along with a planar tungsten emitter and an ideal emitter at $T = 1680$ K. The grating emitter exhibits the best performance, due to broadband response that results from the excitation of multiple resonances.

TABLE 4.1. Performance comparison among structures evaluated.

	Planar W	Multilayer	Grating	Ideal
P_{out} (W/cm^2)	1.1336	2.0983	2.2444	2.6874
η_{TPV} (%)	24.03	27.12	29.95	39.83

The markedly higher performance of the grating emitter is due to its broader frequency and angular response. This enhancement originates from several physical phenomena. To elucidate these mechanisms, Figs. 4.5 and 4.6 show the simulated electric and magnetic fields profiles (Comsol, 2015) inside the grating for TE (Fig. 4.5) and TM (Fig. 4.6) polarizations at several selected wavelengths, which are highlighted in the insets of Fig. 4.4 using

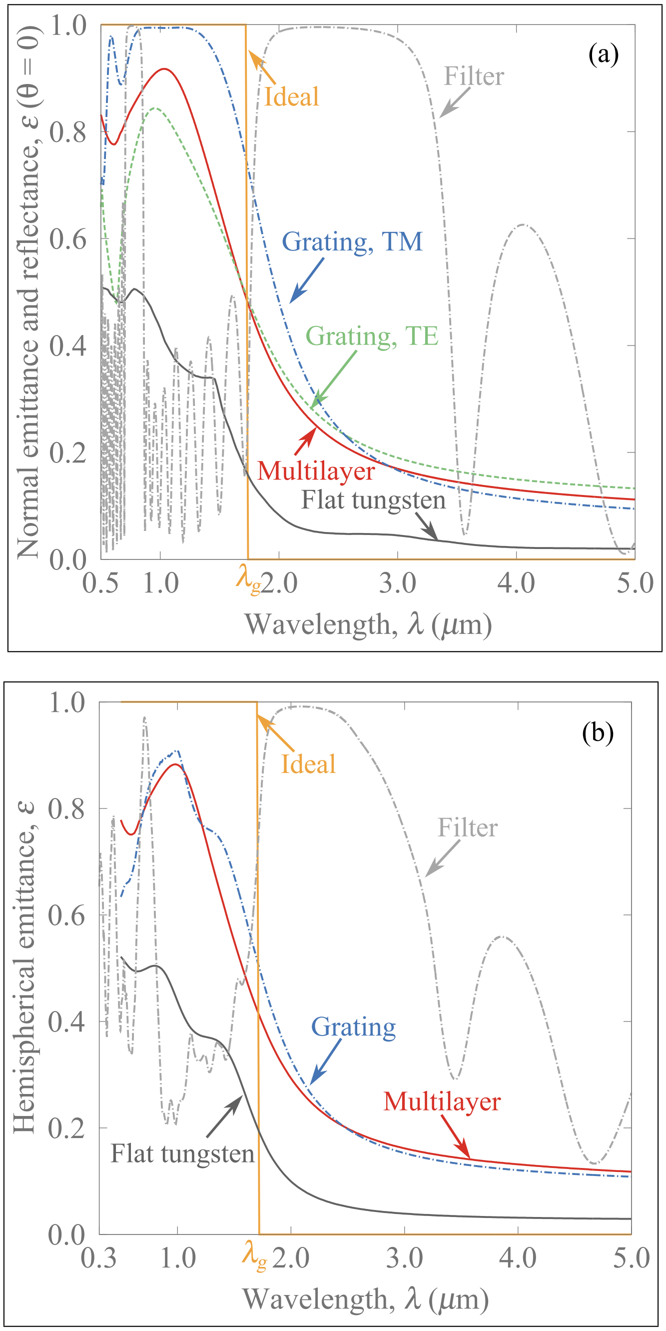

FIGURE 4.2. (a) normal emittance of the grating for TE (green-dashed line) and TM (blue-dotted-dashed line) polarizations of the incident radiation as well as the planar multilayer emittance (red-continuous line). (b) comparison of the hemispherical emittance for the grating (blue) and planar multilayer (red-continuous line) structures. In both figures the ideal emitter (orange-continuous line), with $\lambda_g = 1.72\ \mu$m, and the planar tungsten emittances (gray-continuous line) as well as the reflectance of the PV filter (light gray-dotted-dashed line) are shown for comparison.

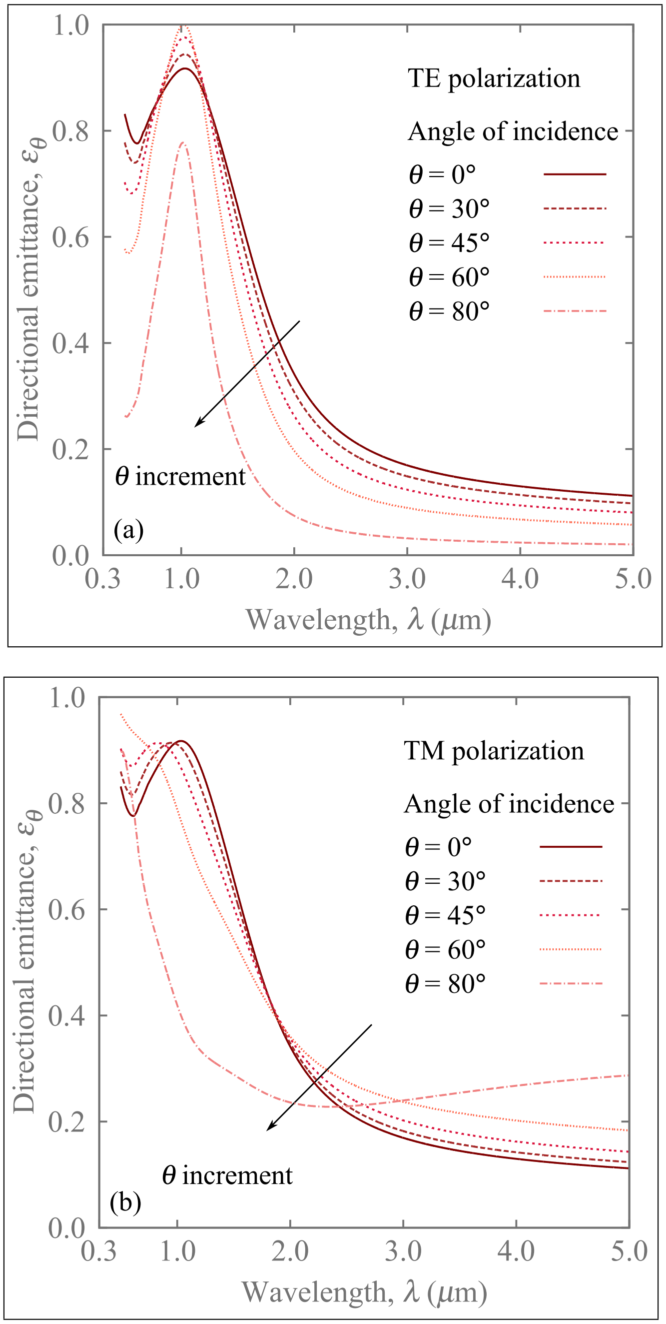

FIGURE 4.3. Directional emittance for the multilayer for both TE (a) and TM (b) polarizations for five different angles of incidence ($\theta = 0, 30, 45, 60,$ and $80°$).

blue dots. Figure 4.5(a) is consistent with an electric field cavity resonance inside the top hafnia layer, giving rise to the $\lambda = 0.93\ \mu$m, $\theta = 0°$ peak in Fig. 4.4. Similarly, Figs. 4.5 (b) and (c) show a strong magnetic field confinement inside the top hafnia layer; this suggests

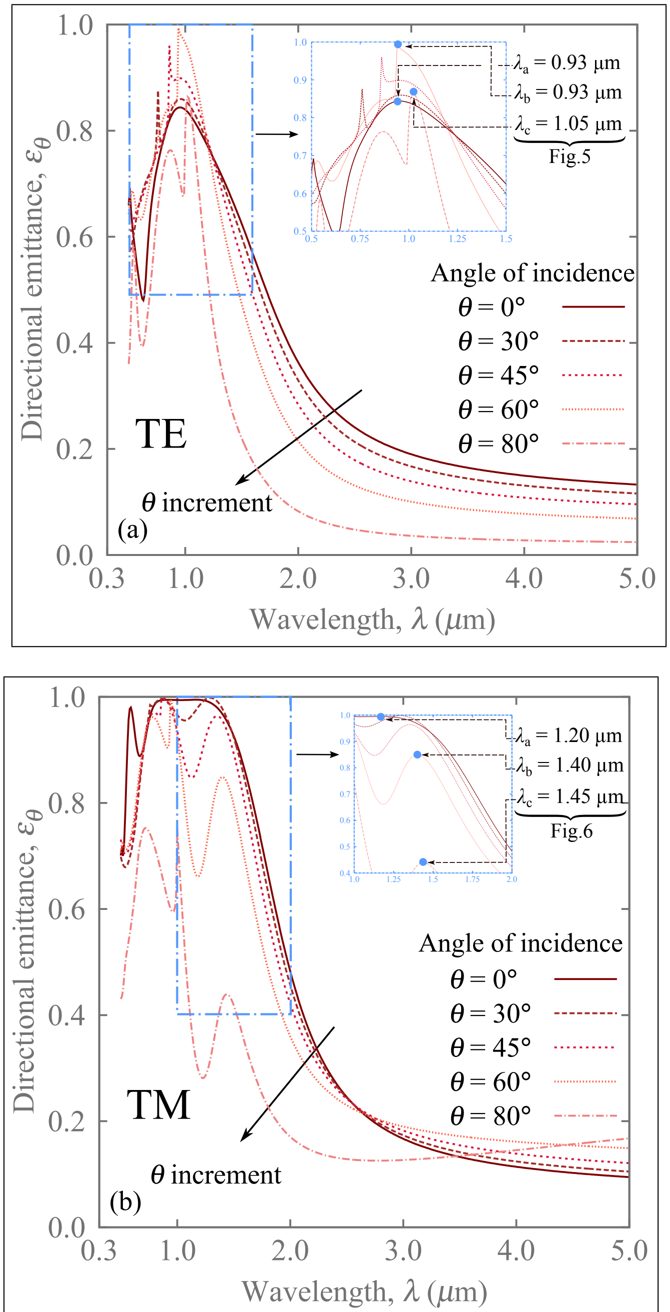

FIGURE 4.4. Directional emittance for the grating for both TE (a) and TM (b) polarizations for five different angles of incidence ($\theta = 0, 30, 45, 60,$ and $80°$). Insets highlight the peaks studied in Figs. 4.5 and 4.6.

that the two peaks for $\theta = 60°$ and $80°$ arise from FP resonances excited at $\lambda = 0.93$ μm and 1.05 μm, respectively. Furthermore, Figs. 4.6(a), (b), and (c) show the electric field profile for peaks observed at $\theta = 0°$, $60°$, and $80°$, respectively, in the case of TM polarization. The strong concentration of the electric field in these three cases is consistent with SPP excitation at wavelengths of $\lambda = 1.2$, 1.4, and $\lambda = 1.45$ μm. The SPP origin of these peaks is corroborated by a simple analysis. By using the dispersion relation for a metal-dielectric interface and momentum conservation $k_x = k_{spp}(\omega) + jK$, where k_x is the horizontal component of the wavevector, $k_x = (2\pi/\lambda)\sin\theta_i$, $k_{spp} = (2\pi/\lambda)\sqrt{\varepsilon_m\varepsilon_d/(\varepsilon_m + \varepsilon_d)}$ is the wavenumber of the surface wave, $K = 2\pi/\Lambda$ is the grating momentum, and j is an integer, the wavelength of SPP excitations can be predicted as a function of incident angle θ. Though simple, this relation gives the correct trend for the peak wavelengths as a function of the angle of incidence ($\lambda = 1.16, 1.33, 1.41, 1.48$, and 1.53μm for $\theta = 0°,\ 30°,\ 45°,\ 60°$, and $80°$, respectively).

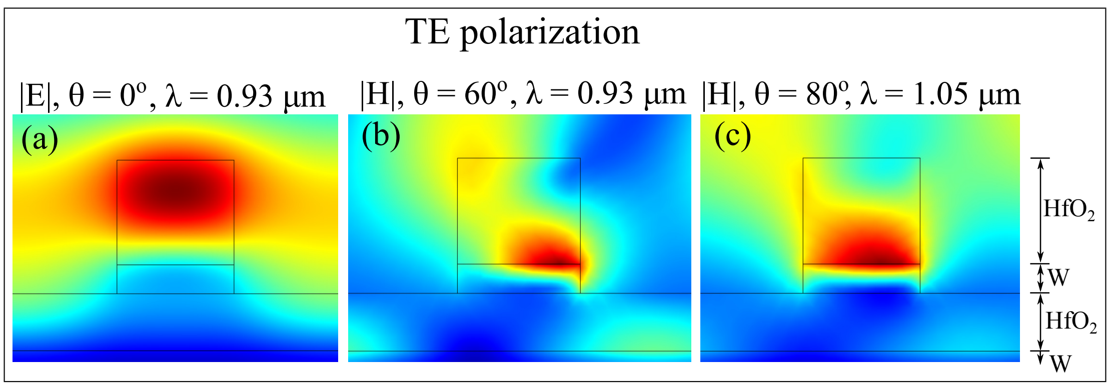

FIGURE 4.5. Electric (a) and magnetic (b, c) fields inside the grating structure for both the TE polarization. Three angles of incidence are considered (a) $\theta = 0°$, (b)60°, and (c) 80° for the wavelengths that match the peaks in the inset of Fig. 4.4(a).

4.3.2. Temperature dependence analysis

Since blackbody radiation depends on temperature, the influence of the emitter temperature on performance was evaluated. Figure 4.7 shows the output power and efficiency as a function of temperature from 1000 to 2000 K. A planar tungsten emitter as well as the ideal emitter have also been plotted for reference. As expected, curves for output power

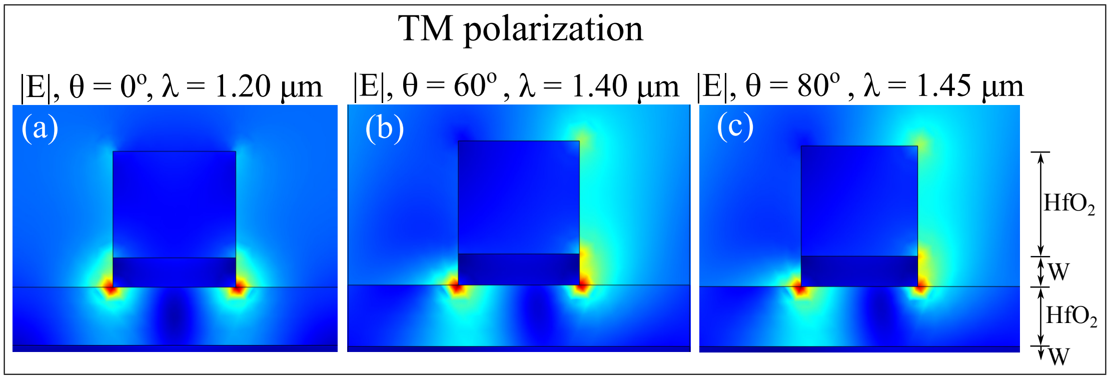

FIGURE 4.6. Electric field inside the grating structure for the TM polarization. Three angles of incidence are considered (a) $\theta = 0°$, (b) 60°, and (c) 80° for the wavelengths that match the peaks of Fig. 4.4(b).

(Fig. 4.7 (a)) increase as a function of temperature, and both the planar multilayer and grating exhibit similar performance trends to the ideal emitter, well above the performance of the planar tungsten emitter. The efficiency (Fig. 4.7 (b)) also increases with temperature for both of the optimized structures reported here as well as for the plain tungsten emitter. As can be seen, the efficiency for the ideal emitter follows a different trend from that of the planar tungsten and optimized designs. This difference is due to the fact that the ideal emitter's out-of-band emitted power is zero, while in the case of the other emitters, the out-of-band emitted power becomes comparable at lower temperatures. As the temperature is lowered for the ideal emitter, fewer photons with $\lambda < \lambda_g$ are produced, so the ideal emitter approaches a monochromatic emitter at low temperatures. This is an artifact of the abrupt drop in emittance assumed for $\lambda > \lambda_g$ in the ideal emitter. For more realistic emitters, the fail of photons with $\lambda > \lambda_g$ becomes more significant at lower temperatures, reducing the efficiency.

4.3.3. Geometric tolerance and sensitivity

Since the genetic optimization algorithm produces very small thicknesses for the tungsten layers for both emitter designs, a simple sensitivity analysis has been performed in order to assess the impact of inevitable variations that can arise in fabrication of these structures. Fabrication involving refractory metals such as tungsten can be challenging. In

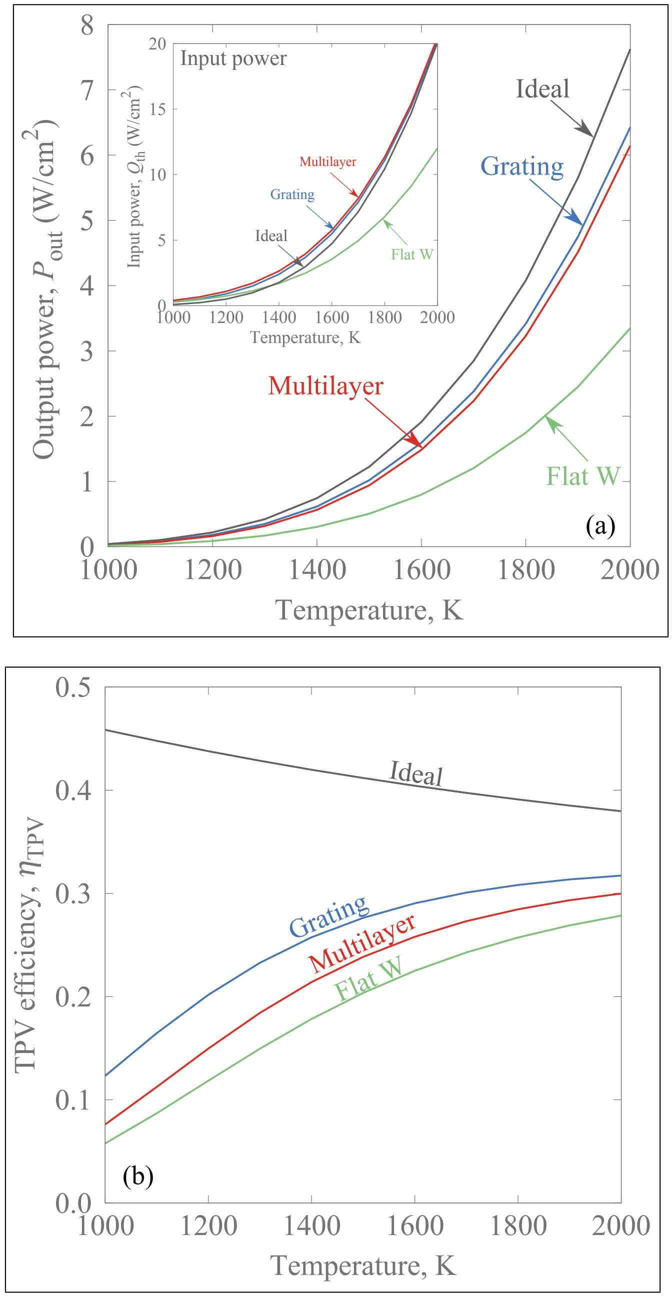

FIGURE 4.7. (a) Output power and (b) efficiency as a function of temperature for the multilayer (red) and grating (blue). Planar tungsten (green) and ideal (gray) emitters are shown for comparison.

particular, since refractory metals tend to form grains, fabrication of smooth, thin layers can be problematic.

The proposed emitter designs feature central tungsten layers with thicknesses of 7 to 44 nm, both of which are of the same order of magnitude as tungsten's typical grain size ($\sim$ 5 to 20 nm (Hao, Chen, & Xiao, 2015)). Figure 4.8 shows output power density and efficiency as a function of the tungsten thickness. The multilayer emitter efficiency remains approximately constant and close to 27 % for tungsten thicknesses between 0.01 and 0.05 μm. Furthermore, the output power density remains above 2 W/cm^2 within variations of 10 % of the tungsten thickness. Oppositely, for the grating emitter the output power remains almost constant for thicknesses above 20 nm. Furthermore, the efficiency of both emitters show very weak dependence on the central tungsten layer thickness. Since hafnia is typically deposited by atomic layer deposition (ALD), very conformal HfO_2 films with very precise thicknesses can be easily obtained.

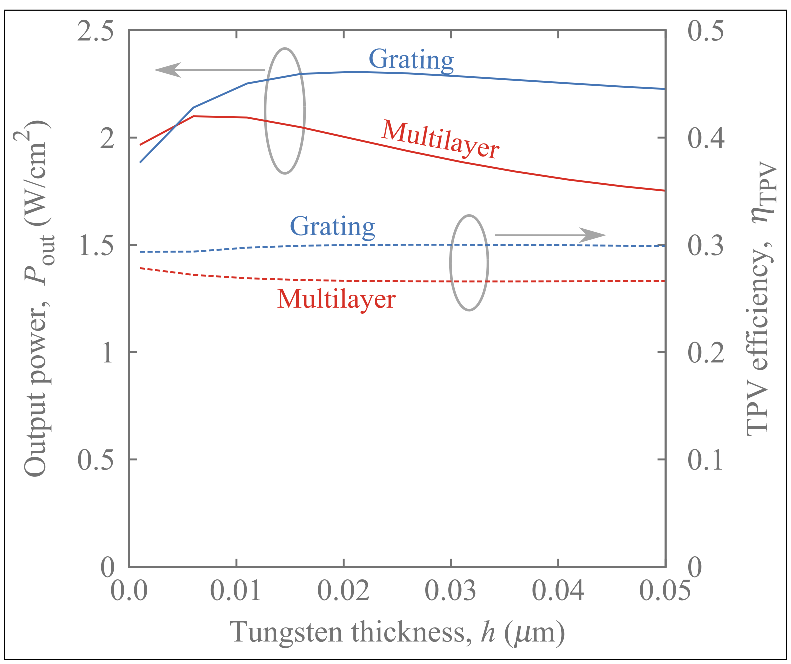

FIGURE 4.8. Output power (left axis) and TPV efficiency (right axis) as a function of tungsten thickness for both the multilayer (red lines) and the grating (blue lines) emitters at 1680 K.

4.4. Conclusions

Two tungsten-hafnia thermal emitter designs for TPV applications with high hemispherical thermal emittances have been evaluated. The designs are intended to match the optical response of GaSb PV cells. The designs were optimized by using a GA along with the RCWA method. Along with the hemispherical emittance, both output power and efficiency were studied. A comparison of both structures was performed by calculating the hemispherical emittance, where it was found that the grating emitter exhibits better performance due to several resonance mechanisms, such as CRs and SPPs. Furthermore, both output power and efficiency were obtained as a function of emitter temperature and tungsten thickness. Even though the performance of both structures is similar, the grating emitter design exhibits higher power density and efficiency as well as reduced sensitivity to metal thickness variations. Structures of this type can be further considered for the design of selective emitters with different metals, such as Mo or Ta as well as dielectrics such as Al_2O_3 or AlN.

5. CONCLUSION AND FUTURE RESEARCH

In this chapter, we summarize the contents and main results presented throughout this thesis. In addition, we present some recommendations for future work.

5.1. Review of the Results and General Remarks

Following an overview in Chapter 1, the detailed results that have been obtained are detailed in Chapters 2–4. In Chapter 2, a novel method based on the Methods of Moment (MoM) and a first-order Taylor expansion of the shape derivative is used to quantify how random surface perturbations impact on the performance of perfect electric conductor gratings under transverse electric (TE) polarized radiation. A MoM solver based on hierarchical bases was implemented and validated using a commercial software package. This implementation allowed us to develop a fast algorithm for quantifying higher order statistical moments, by way of sparse tensor approximations. This deterministic approach was benchmarked against the Monte-Carlo method, and very good agreement was obtained with dramatically less computational effort. We showed the applicability of this method through the calculation of the variance of the grating diffraction efficiency and a comparison with the experimental uncertainty obtained from measurements.

Chapter 3 was focused on the design and simulation of periodic structures as selective thermal emitters, where structures made of tungsten (W) and hafnia (HfO_2) were considered. In this part of the research, we show that by using a deep grating with a hafnia spacer, peaks of almost perfect emittance for both polarizations (TE and TM) can be obtained. This results in a selective thermal emitter with very low polarization sensitivity. We also show numerically and theoretically that the improvements in thermal emittance are due to surface plasmon polaritons (SPP) and magnetic polaritons (MP) in the case of TM polarization, and due to cavity resonances in the case of TE polarization.

In Chapter 4, based on the promising results obtained in Chapter 3, we presented two easy-to-fabricate structures made of tungsten and hafnia. Two structures—a planar multilayer stack and a grating—were optimized through a genetic algorithm (GA). In both cases, we obtained high hemispherical emittance as required for efficient TPV cells. We analyze the performance of both structures as a function of the emission cutoff wavelength as well as emitter temperature. Since the implemented GA suggests the use of very thin tungsten layers, a tolerance analysis was also performed, where it was found that the grating structure possesses more relaxed fabrication tolerances. Analysis of the nature of the emittance enhancement was supported by both numerical simulations and theoretical considerations. In Chapters 3 and 4 we showed that it is possible to obtain high emittance for both TE and TM polarization—as required for TPV applications—using one-dimensional periodic structures.

5.2. Future Research Topics

In this work, we presented two main tracks of research, broadly focused on the improvement of TPV cells. However, several paths for further investigation—not only for TPV cells, but also in different engineering devices—remain open. In the following, I will describe a few possible directions for future work based on the main results obtained in this thesis.

- We have shown and implemented an UQ model for TE polarization. A logical next step is to extend the model for TM polarization as well as impedance boundary conditions. To accomplish this goal, it is necessary to code the TM part by including new boundary conditions for the shape derivative and the double layer potential operator (Harbrecht, 2014). The calculation of the dispersion efficiency of the grating is set in the same way as it was for the TE polarization. Finally, the prediction of Wood's anomalies can be performed by using the grating equation. Since the impedance boundary conditions, Robin type, are a linear combination of Dirichlet and Neumann boundary conditions that have already been studied, the impedance boundary condition problem can be implemented in order to evaluate the impact of spatial variation in properties such as reflectance and absorptance in materials with small skin depth.

- The extension of the model to transmission problems, as well as to full 3D Maxwell equations for 1D and 2D periodic structures, will allow us to model different shapes and materials.
- Since the model was implemented based on the MoM, other periodic structures can also be modeled. This will allow us to quantify the effect of shape perturbations, for example, in the case arrays of cylinders (Watanabe, Nakatake, & Pištora, 2012).
- More fundamental studies are possible through the extension of the models developed here. For example, near–field light–matter interaction, where it has been show that surface roughness influence strong light–matter interaction (Lu, Li, & Liu, 2018), or hyperbolic metamaterials used in plasmonic lithography, where surface roughness produce drops in intensity patterns (X. Chen et al., 2017), could be studied.
- Other engineering applications that involve the shaping of the thermal radiation spectrum, such as radiative cooling (Zhao, Hu, Ao, Xuan, & Pei, 2018; Wong, Tso, Chao, Huang, & Wan, 2018), can be explored.
- Finally, since this work is purely numerical, measurements to validate models can be a path to follow in the case of experimental research.

References

Alabastri, A., Tuccio, S., Giugni, A., Toma, A., Liberale, C., Das, G., ... Zaccaria, R. P. (2013). Molding of plasmonic resonances in metallic nanostructures: Dependence of the non-linear electric permittivity on system size and temperature. *Materials*, *6*(11), 4879–4910. Retrieved from http://www.mdpi.com/1996-1944/6/11/4879 doi: 10.3390/ma6114879

Aljarrah, M. T., Wang, R., Evans, E. A., Clemons, C. B., & Young, G. W. (2011). Experimental characterization and modeling of a nanofiber-based selective emitter for thermophotovoltaic energy conversion: The effect of optical properties. *Journal of Applied Physics*, *109*(3). doi: 10.1063/1.3524567

Anderson, E., Bai, Z., Bischof, C., Blackford, L. S., Demmel, J. W., Dongarra, J. J., ... Sorensen, D. (1992). LAPACK users' guide. *SIAM*.

Babiker, S., Shuai, Y., Sid-Ahmed, M., & Xie, M. (2014). Thermophotovoltaic emitters based on a one-dimensional metallica-dielectric multilayer nanostructures. *Journal of Electronics Cooling and Thermal Control*, *5*(March), 39–48. Retrieved from http://search.ebscohost.com/login.aspx?direct=true{&}profile=ehost{&}scope=site{&}authtype=crawler{&}jrnl=20939655{&}AN=94969425{&}h=MiU9CVn61y11HWW3JHB21Mq3S5t8z8tDuq/cC+dfBilWKDw4svD/If1754gHZcTGHIyX86S50EYVf/XN9pdLvQ=={&}crl=chttp://www.sersc.org/journals/IJEIC/vol

Bermel, P., Ghebrebrhan, M., Chan, W. R., Yeng, Y. X., Araghchini, M., Hamam, R., ... Celanovic, I. (2010, sep). Design and global optimization of high-efficiency thermophotovoltaic systems. *Optics express*, *18 Suppl 3*(103), A314–34. Retrieved from http://www.ncbi.nlm.nih.gov/pubmed/21165063

Bermel, P., Yazawa, K., Gray, J. L., Xu, X., & Shakouri, A. (2016). Hybrid strategies and technologies for full spectrum solar conversion. *Energy Environ. Sci.*, *9*(9), 2776–2788. Retrieved from http://xlink.rsc.org/?DOI=C6EE01386D doi: 10.1039/C6EE01386D

Bett, A. W., & Sulima, O. V. (2003). Gasb photovoltaic cells for applications in tpv generators. *Semiconductor Science and Technology*, *18*(5), S184. Retrieved from http://stacks.iop.org/0268-1242/18/i=5/a=307

Bieri, M., Andreev, R., & Schwab, C. (2009). Sparse tensor discretizacion of elliptic SPDEs. , *31*(6), 4281–4304.

Borisov, A. G., García De Abajo, F. J., & Shabanov, S. V. (2005). Role of electromagnetic trapped modes in extraordinary transmission in nanostructured materials. *Physical Review B - Condensed Matter and Materials Physics*, *71*(7), 1–7. doi: 10.1103/PhysRevB.71.075408

Bruno, O. P., & Haslam, M. C. (2009, feb). Efficient high-order evaluation of scattering by periodic surfaces: deep gratings, high frequencies, and glancing incidences. *Journal of the Optical Society of America A*, *26*(3), 658 – 668. Retrieved from http://www.opticsinfobase.org/abstract.cfm?URI=josaa-26-3-658 doi: 10.1364/JOSAA.26.000658

Bruno, O. P., Lyon, M., Pérez-Arancibia, C., & Turc, C. (2016). Windowed Green Function Method for Layered-Media Scattering. *SIAM Journal on Applied Mathematics*, *76*(5), 1871–1898. Retrieved from http://arxiv.org/abs/1507.04445{%}5Cnhttp://epubs.siam.org/doi/10.1137/15M1033782 doi: 10.1137/15M1033782

Bruno, O. P., Shipman, S. P., Turc, C., & Venakides, S. (n.d.). Efficient Evaluation of Doubly Periodic Green Functions in 3D Scattering , Including Wood Anomaly Frequencies. , 1–36.

Buffa, A., & Hiptmair, R. (2003). Galerkin Boundary Element Methods for Electromagnetic Scattering. , 83–124. Retrieved from http://link.springer.com/10.1007/978-3-642-55483-4{_}3 doi: 10.1007/978-3-642-55483-4_3

Bungartz, H.-J., & Griebel, M. (2004, jun). Sparse grids. *Acta Numerica*, *13*, 147. Retrieved from http://www.journals.cambridge.org/abstract{_}S0962492904000182 doi: 10.1017/S0962492904000182

Celanovic, I. (2006). *Thermophotovoltaics: Shaping the Flow of Thermal Radiation* (Unpublished doctoral dissertation). Massachusetts Institute of Technology.

Celanovic, I., O'Sullivan, F., Jovanovic, N., Qi, M., & Kassakian, J. G. (2004, sep). 1D and 2D Photonic Crystals for Thermophotovoltaic Applications. In R. M. De La Rue, P. Viktorovitch, C. M. Sotomayor Torres, & M. Midrio (Eds.), *Photonic crystal materials and nanostructures* (Vol. 5450, pp. 416–422). Photonic Crystal Materials and Nanostructures. Retrieved from http://proceedings.spiedigitallibrary.org/proceeding.aspx?articleid=845533 doi: 10.1117/12.545539

Chan, D., Soljačić, M., & Joannopoulos, J. (2006, July). Thermal emission and design in one-dimensional periodic metallic photonic crystal slabs. *Physical Review E*, *74*(1), 016609. Retrieved from http://link.aps.org/doi/10.1103/PhysRevE.74.016609 doi: 10.1103/PhysRevE.74.016609

Chan, W. R., Bermel, P., Pilawa-Podgurski, R. C. N., Marton, C. H., Jensen, K. F., Senkevich, J. J., ... Celanovic, I. (2013, apr). Toward high-energy-density, high-efficiency, and moderate-temperature chip-scale thermophotovoltaics. *Proceedings of the National Academy of Sciences of the United States of America*, *110*(14), 5309–14. Retrieved from http://www.pubmedcentral.nih.gov/articlerender.fcgi?artid=3619342{&}tool=pmcentrez{&}rendertype=abstract doi: 10.1073/pnas.1301004110

Chan, W. R., Stelmakh, V., Waits, C. M., Soljacic, M., Joannopoulos, J. D., & Celanovic, I. (2015). Photonic Crystal Enabled Thermophotovoltaics for a Portable Microgenerator. *Journal of Physics: Conference Series*, *660*, 1–5. doi: 10.1088/1742-6596/660/1/012069

Chandler-Wilde, S. N. (1995). Boundary value problems for the Helmholtz equation in a half-plane. In *Proceedings of the 3rd international conference on mathematical and numerical aspects of wave propagation* (pp. 188–197).

Chandler-Wilde, S. N., & Graham, I. (2009). Highly Oscillatory Problems: Computation, Theory and Applications BT - Highly Oscillatory Problems: Computation, Theory and Applications. *Highly Oscillatory Problems: Computation, Theory and Applications*. Retrieved from papers2://publication/uuid/A1C28810-15F2-4E14-A73B-F36EA2A8782C

Chateau, N., & Hugonin, J.-P. (1994, Apr). Algorithm for the rigorous coupled-wave analysis of grating diffraction. *J. Opt. Soc. Am. A*, *11*(4), 1321–1331. Retrieved from http://josaa.osa.org/abstract.cfm?URI=josaa-11-4-1321 doi: 10.1364/JOSAA.11.001321

Chen, G. (2005). *Nanoscale Energy Transport and Conversion* (First edit ed.). Oxford University Press.

Chen, X., Zhang, C., Yang, F., Liang, G., Li, Q., & Guo, L. J. (2017). Plasmonic lithography utilizing epsilon near zero hyperbolic metamaterial. *ACS Nano*, *11*(10), 9863-9868. Retrieved from https://doi.org/10.1021/acsnano.7b03584 (PMID: 28968069) doi: 10.1021/acsnano.7b03584

Chen, Y.-B., & Zhang, Z. (2007, jan). Design of tungsten complex gratings for thermophotovoltaic radiators. *Optics Communications*, *269*(2), 411–417. Retrieved from http://linkinghub.elsevier.com/retrieve/pii/S0030401806008546 doi: 10.1016/j.optcom.2006.08.040

Chirumamilla, M., Chirumamilla, A., Yang, Y., Roberts, A. S., Kristensen, P. K., Chaudhuri, K., … Pedersen, K. (2017). Large-Area Ultrabroadband Absorber for Solar Thermophotovoltaics Based on 3D Titanium Nitride Nanopillars. *Advanced Optical Materials*, *1700552*, 1700552. Retrieved from http://doi.wiley.com/10.1002/adom.201700552 doi: 10.1002/adom.201700552

Chirumamilla, M., Roberts, A. S., Ding, F., Wang, D., Kristensen, P. K., Bozhevolnyi, S. I., & Pedersen, K. (2016). Multilayer tungsten-alumina-based broadband light absorbers for high-temperature applications. *Optical Materials Express*, *6*(8), 2704. Retrieved from https://www.osapublishing.org/abstract.cfm?URI=ome-6-8-2704 doi: 10.1364/OME.6.002704

Chou, J. B., Yeng, Y. X., Lenert, A., Rinnerbauer, V., Celanovic, I., Soljačić, M., … Kim, S.-G. (2013, dec). Design of wide-angle selective absorbers/emitters with dielectric filled metallic photonic crystals for energy applications. *Optics Express*, *22*(S1), A144. Retrieved from http://www.opticsinfobase.org/abstract.cfm?URI=oe-22-S1-A144 doi: 10.1364/OE.22.00A144

Chubb, D. (2007). *Fundamentals of Thermophotovoltaic Energy Conversion (Google eBook)*. Retrieved from http://books.google.com/books?hl=en{&}lr={&}id=sKal2bUROJgC{&}pgis=1

Comsol. (2015). Multiphysics reference guide for comsol 5.1 [Computer software manual].

Coutts, T. J. (1999). Review of progress in thermophotovoltaic generation of electricity. *Renewable & sustainable energy reviews*, *3*(2), 77–184. doi: 10.1016/S1364-0321(98)00021-5

Dambrine, M., Greff, I., Harbrecht, H., & Puig, B. (2014). SOLUTION OF THE POISSON EQUATION WITH A THIN LAYER OF RANDOM THICKNESS. *math.unibas.ch*, 1–23. Retrieved from https://math.unibas.ch/

uploads/x4epublication/56238/RandomDomain.pdf doi: 10.1137/140998652

Dashiell, M. W., Beausang, J. F., Ehsani, H., Nichols, G. J., Depoy, D. M., Danielson, L. R., ... In, A. (2006). Quaternary InGaAsSb Thermophotovoltaic Diodes. *IEEE Transactions on Electron Devices*, *53*(12), 2879–2891. doi: 10.1109/TED.2006.885087

Deng, H., Wang, T., Gao, J., & Yang, X. (2014, mar). Metamaterial thermal emitters based on nanowire cavities for high-efficiency thermophotovoltaics. *Journal of Optics*, *16*(3), 035102. Retrieved from http://stacks.iop.org/2040-8986/16/i=3/a=035102?key=crossref.5e88b365dace4bd2cda6044c2be970eb doi: 10.1088/2040-8978/16/3/035102

Desanto, J., Erdmann, G., Hereman, W., & Misra, M. (1998). Theoretical and computational aspects of scattering from periodic surfaces one-dimensional transmission interface. *Waves in Random Media*, *8*(303), 385–414. doi: 10.1088/0959-7174/8/4/001

Dyachenko, P. N., Molesky, S., Petrov, A. Y., Störmer, M., Krekeler, T., Lang, S., ... Eich, M. (2016). Controlling thermal emission with refractory epsilon-near-zero metamaterials via topological transitions. *Nature Communications*, *7*(May), 11809. Retrieved from http://www.nature.com/doifinder/10.1038/ncomms11809 doi: 10.1038/ncomms11809

Enoch, S., & Bonod, N. (Eds.). (2012). *Plasmonics* (Vol. 167). Berlin, Heidelberg: Springer Berlin Heidelberg. Retrieved from http://link.springer.com/10.1007/978-3-642-28079-5 doi: 10.1007/978-3-642-28079-5

Erwin G. Loewen, & Popov, E. (1997). *Diffraction Gratings and Applications*. New York, NY: CRC Press.

Ezaki, T., Werner, P., & Hane, M. (2003, Dec 01). Self-consistent quantum mechanical monte carlo mosfet device simulation. *Journal of Computational Electronics*, *2*(2), 97–103. Retrieved from https://doi.org/10.1023/B:JCEL.0000011406.20864.06 doi: 10.1023/B:JCEL.0000011406.20864.06

Fano, U. (1941). The theory of anomalous diffraction gratings and of quasi-stationary waves on metallic surfaces (Sommerfeld's waves). *JOSA*, *928*(1935). Retrieved from http://www.opticsinfobase.org/abstract.cfm?uri=josa-31-3-213

Fortin, G., & McCarthy, N. (2005). Chirped holographic grating used as the dispersive element in an optical spectrometer. *Applied Optics*, *44*(23), 4874–83. Retrieved from http://www.ncbi.nlm.nih.gov/pubmed/16114525 doi: 10.1364/AO.44.004874

Fu, S. M., Zhong, Y. K., Tu, M. H., Chen, B. R., & Lin, A. (2016). A Planarized Thermophotovoltaic Emitter With Idealized Selective Emission. *IEEE Photonics Journal*, *8*(4), 1–9. Retrieved from http://ieeexplore.ieee.org/lpdocs/epic03/wrapper.htm?arnumber=7523958 doi: 10.1109/JPHOT.2016.2594704

Gallinet, B., Butet, J., & Martin, O. J. (2015). Numerical methods for nanophotonics: Standard problems and future challenges. *Laser and Photonics Reviews*, *9*(6), 577–603. doi: 10.1002/lpor.201500122

Gertsner, T., & Griebel, M. (2008). Sparse grids (Quantitative Finance). *Encyclopedia of Quantitative Finance*, *13*, 5. doi: 10.1017/S0962492904000182

Ghanekar, A., Sun, M., Zhang, J., Zongqin, & Zheng, Y. (2017). Optimal Design of Wavelength Selective Thermal Emitter for Thermophotovoltaic Applications. *Journal of Thermal Science and Engineering Applications*, *10*(1), 011004. Retrieved from http://thermalscienceapplication.asmedigitalcollection

.asme.org/article.aspx?doi=10.1115/1.4036790 doi: 10.1115/1.4036790

Goldberg, D. E. (1989). *Genetic algorithms in search, optimization and machine learning* (1st ed.). Boston, MA, USA: Addison-Wesley Longman Publishing Co., Inc.

Grant, F. R. (1969). *Introduction to Modern Optics.* Dover Publications. doi: 10.1119/1.1975142

Han, F., Du, Y., Cheng, S., Zhou, Q., Chen, C., KeyongHou, ... Li, H. (2012). Computational fluid dynamics-monte carlo method for calculation of the ion trajectories and applications in ion mobility spectrometry. *International Journal of Mass Spectrometry*, *309*, 13 - 21. Retrieved from http://www.sciencedirect.com/science/article/pii/S1387380611003587 doi: https://doi.org/10.1016/j.ijms.2011.08.017

Hao, Q., Chen, W., & Xiao, G. (2015). Beta () tungsten thin films: Structure, electron transport, and giant spin hall effect. *Applied Physics Letters*, *106*(18), 182403. Retrieved from https://doi.org/10.1063/1.4919867 doi: 10.1063/1.4919867

Harbrecht, H. (2010, mar). A finite element method for elliptic problems with stochastic input data. *Applied Numerical Mathematics*, *60*(3), 227–244. Retrieved from http://linkinghub.elsevier.com/retrieve/pii/S0168927409001925 doi: 10.1016/j.apnum.2009.12.002

Harbrecht, H. (2014). Second Moment Analysis for Robin Boundary Value Problems on Random Domains. In M. Griebel (Ed.), *Singular phenomena and scaling in mathematical models* (pp. 361—-381). Springer International Publishing. Retrieved from http://dx.doi.org/10.1007/978-3-319-00786-1{_}16 doi: 10.1007/978-3-319-00786-1_16

Harbrecht, H., Peters, M., & Siebenmorgen, M. (2013, nov). Combination technique based k-th moment analysis of elliptic problems with random diffusion. *Journal of Computational Physics*, *252*, 128–141. Retrieved from http://linkinghub.elsevier.com/retrieve/pii/S0021999113004373 doi: 10.1016/j.jcp.2013.06.013

Harbrecht, H., Schwab, C., & Schneider, R. (2006). Sparse Second Moment Analysis for Potentials on Stochastic Domains. *Talk*. Retrieved from papers3://publication/uuid/84262CBC-ED4B-496A-802D-37168C290072

Harder, N.-P., & Würfel, P. (2003). Theoretical limits of thermophotovoltaic solar energy conversion. *Semiconductor Science and Technology*, *18*(5), S151–S157. Retrieved from http://stacks.iop.org/0268-1242/18/i=5/a=303{%}5Cnhttp://iopscience.iop.org/article/10.1088/0268-1242/18/5/303 doi: 10.1088/0268-1242/18/5/303

Herv, A., Drvillon, J., Ezzahri, Y., & Joulain, K. (2018). Radiative cooling by tailoring surfaces with microstructures: Association of a grating and a multi-layer structure. *Journal of Quantitative Spectroscopy and Radiative Transfer*, *221*, 155 - 163. Retrieved from http://www.sciencedirect.com/science/article/pii/S0022407318303388 doi: https://doi.org/10.1016/j.jqsrt.2018.09.015

Higdon, D., Klein, R., Anderson, M., Berliner, M., Covey, C., Ghattas, O., ... Stewart, J. (2006). *Uncertainty Quantification and Error Analysis* (Vol. 836; Tech. Rep.). Los Alamos, National Laboratory.

Hiptmair, R., Jerez-Hanckes, C., & Schwab, C. (2013). Sparse tensor edge elements. *BIT*, *53*(4), 925–939. Retrieved from http://dx.doi.org/10.1007/s10543-013-0435-3 doi: 10.1007/s10543-013-0435-3

Hiptmair, R., & Li, J. (2013). Shape derivatives in differential forms I: An intrinsic perspective. *Annali di Matematica Pura ed Applicata*, *192*(6), 1077–1098. doi: 10.1007/s10231-012-0259-9

Hiptmair, R., & Li, J. (2017). Shape Derivatives in Differential Forms II : Shape Derivatives for Scattering Problems. *Seminar of Applied Mathematics*.

Ilic, O., Jablan, M., Joannopoulos, J. D., Celanovic, I., & Soljacić, M. (2012, may). Overcoming the black body limit in plasmonic and graphene near-field thermophotovoltaic systems. *Optics express*, *20*(10), A366–84. Retrieved from http://www.ncbi.nlm.nih.gov/pubmed/22712094

J., E., & G., S. (n.d.). Diffraction in periodic structures and optimal design of binary gratings. part i: direct problems and gradient formulas. *Mathematical Methods in the Applied Sciences*, *21*(14), 1297-1342. Retrieved from https://onlinelibrary.wiley.com/doi/abs/10.1002/ doi: 10.1002/(SICI)1099-1476(19980925)21:14⟨1297::AID-MMA997⟩3.0.CO;2-C

Jerez-Hanckes, C., & Schwab, C. (2016). Electromagnetic wave scattering by random surfaces: uncertainty quantification via sparse tensor boundary elements. *IMA Journal of Numerical Analysis*, drw031. Retrieved from http://imanum.oxfordjournals.org/lookup/doi/10.1093/imanum/drw031 doi: 10.1093/imanum/drw031

Jin, J.-M. (2003). *The finite element method in electromagnetics*. Retrieved from http://books.google.com/books?id=scB4QgAACAAJ{&}pgis=1

Jin, J.-M. (2010). *Theory and Computation of Electromagnetic Fields*. Retrieved from http://doi.wiley.com/10.1002/9780470874257{%}0Ahttp://doi.wiley.com/10.1002/9780470874257.index doi: 10.1002/9780470874257.index

Johannes, B., & Simon, S. (n.d.). Using adaptive sparse grids to solve high-dimensional dynamic models. *Econometrica*, *85*(5), 1575-1612. Retrieved from https://onlinelibrary.wiley.com/doi/abs/10.3982/ECTA12216 doi: 10.3982/ECTA12216

Johnson, C. (1987). *Numerical Solution of Partial Differential Equations by the Finite Element Method*. New York, NY: Dover Publications.

Johnson, C., & Nedelec, J. (1980, oct). On the coupling of boundary integral and finite element methods. *Mathematics of Computation*, *35*(152), 1063–1079. Retrieved from http://www.jstor.org/stable/2006375

Kahnert, F. M. (2003). Numerical methods in electromagnetic scattering theory. *Journal of Quantitative Spectroscopy and Radiative Transfer*, *80*, 775–824. doi: 10.1016/S0022-40730200321-7

Kar, S. (2013). *High Permittivity Gate Dielectric Materials* (Vol. 43; S. Kar, Ed.). Berlin, Heidelberg: Springer Berlin Heidelberg. Retrieved from http://link.springer.com/10.1007/978-3-642-36535-5 doi: 10.1007/978-3-642-36535-5

Keramat, M., & Kielbasa, R. (1997, Jun). A study of stratified sampling in variance reduction techniques for parametric yield estimation. In *Circuits and systems, 1997. iscas '97., proceedings of 1997 ieee international symposium on* (Vol. 3, p. 1652-1655 vol.3). doi: 10.1109/ISCAS.1997.621450

Khankhoje, U. K., & Cwik, T. A. (2014). A mesh reconfiguration scheme for speeding up Monte Carlo simulations of electromagnetic scattering by random rough surfaces. *Computer Physics Communications*, *185*(2), 445–447. Retrieved from http://dx.doi.org/10.1016/j.cpc.2013.03.005 doi: 10.1016/j.cpc.2013.03.005

Kim, J. H., Jung, S. M., & Shin, M. W. (2017). High-temperature degradation of one-dimensional metallodielectric (W/SiO2) photonic crystal as selective thermal emitter for thermophotovoltaic system. *Optical Materials*, *72*, 45–51. Retrieved from https://doi.org/10.1016/j.optmat.2017.05.041 doi: 10.1016/j.optmat.2017.05.041

Kirsch, A. (1993). Diffraction by periodic structures. In L. Päivärinta & E. Somersalo (Eds.), *Inverse problems in mathematical physics* (pp. 87–102). Berlin, Heidelberg: Springer Berlin Heidelberg.

Knibbs, R. H. (1969, jun). The measurement of thermal expansion coefficient of tungsten at elevated temperatures. *Journal of Physics E: Scientific Instruments*, *2*(6), 311. Retrieved from http://stacks.iop.org/0022-3735/2/i=6/a=311?key=crossref.a5263d5690c3e907df4656f3e01a57eb doi: 10.1088/0022-3735/2/6/311

Kong, J. A. (1986). *Electromagnetic Wave Theory.* Retrieved from https://books.google.com.my/books/about/Electromagnetic{_}Wave{_}Theory.html?id=OposAAAAYAAJ{&}pgis=1 doi: 10.1109/PROC.1987.13818

L'Ecuyer, P., & Lemieux, C. (2005). Recent advances in randomized quasi-monte carlo methods. In M. Dror, P. L'Ecuyer, & F. Szidarovszky (Eds.), *Modeling uncertainty: An examination of stochastic theory, methods, and applications* (pp. 419–474). Boston, MA: Springer US. Retrieved from https://doi.org/10.1007/0-306-48102-2_20 doi: 10.1007/0-306-48102-2_20

Lee, H.-J., Smyth, K., Bathurst, S., Chou, J., Ghebrebrhan, M., Joannopoulos, J., ... Kim, S.-G. (2013, jun). Hafnia-plugged microcavities for thermal stability of selective emitters. *Applied Physics Letters*, *102*(24), 241904. Retrieved from http://aip.scitation.org/doi/10.1063/1.4811703 doi: 10.1063/1.4811703

Lenert, A., Bierman, D. M., Nam, Y., Chan, W. R., Celanovic, I., Soljačić, M., ... Celanović, I. (2014a, jan). A nanophotonic solar thermophotovoltaic device. *Nature Nanotechnology*, *9*(January), 1–5. Retrieved from http://www.ncbi.nlm.nih.gov/pubmed/24441985http://www.nature.com/doifinder/10.1038/nnano.2013.286 doi: 10.1038/nnano.2013.286

Lenert, A., Bierman, D. M., Nam, Y., Chan, W. R., Celanovic, I., Soljačić, M., ... Celanović, I. (2014b, jan). A nanophotonic solar thermophotovoltaic device. *Nature Nanotechnology*, *9*(January), 1–5. Retrieved from http://www.ncbi.nlm.nih.gov/pubmed/24441985http://www.nature.com/doifinder/10.1038/nnano.2013.286 doi: 10.1038/nnano.2013.286

Li, L. (1996, Sep). Use of fourier series in the analysis of discontinuous periodic structures. *J. Opt. Soc. Am. A*, *13*(9), 1870–1876. Retrieved from http://josaa.osa.org/abstract.cfm?URI=josaa-13-9-1870 doi: 10.1364/JOSAA.13.001870

Liao, T., Cai, L., Zhao, Y., & Chen, J. (2016). Efficiently exploiting the waste heat in solid oxide fuel cell by means of thermophotovoltaic cell. *Journal of Power Sources*, *306*, 666–673. Retrieved from http://dx.doi.org/10.1016/j.jpowsour.2015.12.080 doi: 10.1016/j.jpowsour.2015.12.080

Liu, M., Gao, Z., & Hesthaven, J. S. (2011). Adaptive sparse grid algorithms with applications to electromagnetic scattering under uncertainty. *Applied Numerical Mathematics*, *61*(1), 24 - 37. Retrieved from http://www.sciencedirect.com/science/article/pii/S0168927410001376 doi: https://doi.org/10.1016/j.apnum.2010.08.002

Loewen, E. G., & Popov, E. (1997). Diffraction gratings and applications. , 28.

Lu, Y.-w., Li, L.-y., & Liu, J.-f. (2018, dec). Influence of Surface Roughness on Strong Light-Matter Interaction of a Quantum Emitter-Metallic Nanoparticle System. *Scientific Reports*, *8*(1), 7115. Retrieved from http://dx.doi.org/10.1038/s41598-018-25584-5http://www.nature.com/articles/s41598-018-25584-5 doi: 10.1038/s41598-018-25584-5

Maier, S. A. (2008). *Plasmonics: Fundamentals and Applications* (first edit ed.). Springer. Retrieved from http://www.springer.com/gp/book/9780387331508

Markus Kollmann. (2008). *Shape Optimization with Shape Derivatives* (Unpublished doctoral dissertation). Johannes Kepler Universitat.

Marquier, F., Arnold, C., Laroche, M., Greffet, J. J., & Chen, Y. (2008). Degree of polarization of thermal light emitted by gratings supporting surface waves. *Optics express*, *16*(8), 5305–5313. doi: 10.1364/OE.16.005305

Marquier, F., Laroche, M., Carminati, R., & Greffet, J.-J. (2007). Anisotropic Polarized Emission of a Doped Silicon Lamellar Grating. *Journal of Heat Transfer*, *129*(1), 11. doi: 10.1115/1.2360594

Matlab optimization toolbox. (2017).

Matthew N O Sadiku. (2009). *Monte Carlo Methods for Electromagnetics* (First edit ed.; CRC Press, Ed.).

Mbakop, F. K., Djongyang, N., & Raidani, D. (2016). One - dimensional TiO2 / SiO2 photonic crystal filter for thermophotovoltaic applications. *Journal of the European Optical Society-Rapid Publications*, 12–23. doi: 10.1186/s41476-016-0026-4

McEntaffer, R., DeRoo, C., Schultz, T., Gantner, B., Tutt, J., Holland, A., … Koecher, L. (2013). First results from a next-generation off-plane X-ray diffraction grating. *Experimental Astronomy*, *36*(1-2), 389–405. doi: 10.1007/s10686-013-9338-1

Minissale, M., Pardanaud, C., Bisson, R., & Gallais, L. (2017). The temperature dependence of optical properties of tungsten in the visible and near-infrared domains: an experimental and theoretical study. *Journal of Physics D: Applied Physics*, *50*(45), 455601. Retrieved from http://stacks.iop.org/0022-3727/50/i=45/a=455601

Moharam, M., & Gaylord, T. (1981, jul). Rigorous coupled-wave analysis of planar-grating diffraction. *JOSA*, *71*(7), 811. Retrieved from http://www.opticsinfobase.org/abstract.cfm?URI=josa-71-7-811http://www.opticsinfobase.org/abstract.cfm?uri=josa-71-7-811 doi: 10.1364/JOSA.71.000811

Molesky, S., Dewalt, C. J., & Jacob, Z. (2013, Jan). High temperature epsilon-near-zero and epsilon-near-pole metamaterial emitters for thermophotovoltaics. *Opt. Express*, *21*(S1), A96–A110. Retrieved from http://www.opticsexpress.org/abstract.cfm?URI=oe-21-101-A96 doi: 10.1364/OE.21.000A96

Nam, Y., Yeng, Y. X., Lenert, A., Bermel, P., Celanovic, I., Soljačić, M., & Wang, E. N. (2014, mar). Solar thermophotovoltaic energy conversion systems with two-dimensional tantalum photonic crystal absorbers and emitters. *Solar Energy Materials and Solar Cells*, *122*, 287–296. Retrieved from http://linkinghub.elsevier.com/retrieve/pii/S0927024813006454 doi: 10.1016/j.solmat.2013.12.012

Neeser, F., & Massey, J. (1993). Proper complex random processes with applications to information theory. *IEEE Transactions on Information Theory*, *39*(4), 1293–1302. doi: 10.1109/18.243446

Nguyen-Huu, N., Chen, Y.-B., & Lo, Y.-L. (2012, mar). Development of a polarization-insensitive thermophotovoltaic emitter with a binary grating. *Optics express*, *20*(6), 5882–90. Retrieved from http://www.ncbi.nlm.nih.gov/pubmed/23422586

Nguyen-Huu, N., Lo, Y.-L., Chen, Y.-B., Yang, T.-Y., Nghia Nguyen-Huu, Lo, Y.-L., ... Yang, T.-Y. (2011). Realization of integrated polarizer and color filters based on subwavelength metallic gratings using a hybrid numerical scheme. *Applied optics*, *50*(4), 415–426. Retrieved from http://apps.isiknowledge.com.libproxy.ucl.ac.uk/full{_}record.do?product=WOS{&}search{_}mode=GeneralSearch{&}qid=11{&}SID=R1i9EO4PmP266i9HmcG{&}page=1{&}doc=2{%}5Cnhttp://www.ncbi.nlm.nih.gov/pubmed/21283230 doi: 10.1364/AO.50.000415

Nguyen-Huu, N., Pištora, J., & Cada, M. (2016). Wavelength-selective emitters with pyramid nanogratings enhanced by multiple resonance modes. *Nanotechnology*, *27*(15), 155402. Retrieved from http://stacks.iop.org/0957-4484/27/i=15/a=155402?key=crossref.f85963f7f6f561fbc4ca9e7ea92bf917 doi: 10.1088/0957-4484/27/15/155402

Ohnuki, S., Chew, W. C., & Hinata, T. (2005). Monte Carlo simulation of 1-D rough surface scattering in 2-D space. *Journal of Electromagnetic Waves and Applications*, *19*(8), 1085–1102. Retrieved from http://www.scopus.com/inward/record.url?eid=2-s2.0-22744457214{&}partnerID=40{&}md5=ec34a1c3bc916dc73f853ca0f0828916 doi: 10.1163/156939305775526106

O'Sullivan, F., Celanovic, I., Jovanovic, N., Kassakian, J., Akiyama, S., & Wada, K. (2005). Optical characteristics of one-dimensional sisio$_2$ photonic crystals for thermophotovoltaic applications. *Journal of Applied Physics*, *97*(3), 033529. doi: 10.1063/1.1849437

Owen, A. B. (2013). *Monte carlo theory, methods and examples*.

Ozgun, O., & Kuzuoglu, M. (2013). Transformation electromagnetics based analysis of waveguides with random rough or periodic grooved surfaces. *IEEE Transactions on Microwave Theory and Techniques*, *61*(2), 709–719. doi: 10.1109/TMTT.2012.2231428

Padma Kumar, H., Vidya, S., Saravana Kumar, S., Vijayakumar, C., Solomon, S., & Thomas, J. (2015). Optical properties of nanocrystalline HfO2 synthesized by an auto-igniting combustion synthesis. *Journal of Asian Ceramic Societies*, *3*(1), 64–69. Retrieved from http://linkinghub.elsevier.com/retrieve/pii/S2187076414001006 doi: 10.1016/j.jascer.2014.10.009

Palmer, C., & Loewen, E. (2014). *Diffraction gratings handbook*.

Petit, R. (1980). *Electromagnetic Theory of Gratings* (Vol. 22; R. Petit, Ed.). Berlin, Heidelberg: Springer Berlin Heidelberg. Retrieved from http://link.springer.com/10.1007/978-3-642-81500-3 doi: 10.1007/978-3-642-81500-3

Pfiester, N. A., & Vandervelde, T. E. (2016). Selective emitters for thermophotovoltaic applications. *Physica Status Solidi (A) Applications and Materials Science*, *1600410*(1), 1–24. doi: 10.1002/pssa.201600410

Potthast, R. (1996a). Domain Derivatives in Electromagnetic Scattering. , *19*(September 1995), 1157–1175.

Potthast, R. (1996b). Frechet differentiability of the solution to the acoustic {N}eumann scattering problem with respect to the domain. *J. Inverse Ill-Posed Problems*, *4*(1), 67–84. doi: 10.1515/jiip.1996.4.1.67

Rabady, R. I. (2017). Optimized spectral splitting in thermo-photovoltaic system for maximum conversion ef fi ciency. *Energy*, *119*, 852–859. Retrieved from http://dx.doi.org/10.1016/j.energy.2016.11.055 doi: 10.1016/j.energy.2016.11.055

Rakic, A. D., Djurisic, A. B., Elazar, J. M., & Majewski, M. L. (1998). Optical properties of metallic films for vertical-cavity optoelectronic devices. *Applied optics*, *37*(22), 5271–5283. Retrieved from http://www.ncbi.nlm.nih.gov/pubmed/18286006 doi: 10.1364/AO.37.005271

Rayleigh, L. (1907). On The Dynamical Theory of Gratings. *Proceedings of the Royal Society of London A: Mathematical, Physical and Engineering Sciences*, *79*, 399—-416. Retrieved from http://rspa.royalsocietypublishing.org/content/79/532/399 doi: 10.1098/rspa.1907.0051

Rephaeli, E., & Fan, S. (2009, aug). Absorber and emitter for solar thermo-photovoltaic systems to achieve efficiency exceeding the Shockley-Queisser limit. *Optics express*, *17*(17), 15145–59. Retrieved from http://www.ncbi.nlm.nih.gov/pubmed/19687992

Rinnerbauer, V., & Lenert, A. (2014). Metallic Photonic Crystal Absorber-Emitter for Efficient Spectral Control in High-Temperature Solar Thermophotovoltaics. *Advanced Energy . . .*, 1–29. Retrieved from http://scholar.google.com/scholar?hl=en{&}btnG=Search{&}q=intitle:No+Title{#}0http://onlinelibrary.wiley.com/doi/10.1002/aenm.201400334/full doi: 10.1002/aenm.))

Rinnerbauer, V., Yeng, Y. X., Chan, W. R., Senkevich, J. J., Joannopoulos, J. D., Solja, M., & Celanovic, I. (2013). High-temperature stability and selective thermal emission of polycrystalline tantalum photonic crystals. *International online journal of Optics*, *21*(9), 298–303. doi: 10.1364/OE.21.011482

Sanamzadeh, M., Tsang, L., Johnson, J. T., Burkholder, R. J., & Tan, S. (2017). Scattering of electromagnetic waves from 3D multilayer random rough surfaces based on the second-order small perturbation method: energy conservation, reflectivity, and emissivity. *Journal of the Optical Society of America A*, *34*(3), 395. Retrieved from https://www.osapublishing.org/DirectPDFAccess/55EFE835-BE7F-EE34-4140FAEEEEF7E319{_}360224/josaa-34-3-395.pdf?da=1{&}id=360224{&}seq=0{&}mobile=no{%}5Cnhttps://www.osapublishing.org/abstract.cfm?URI=josaa-34-3-395 doi: 10.1364/JOSAA.34.000395

Sauter, S. A., & Schwab, C. (2011). *Boundary Element Methods* (Vol. 39). Berlin, Heidelberg: Springer Berlin Heidelberg. Retrieved from http://www.sciencedirect.com/science/article/pii/B9780080402000500431http://link.springer.com/10.1007/978-3-540-68093-2 doi: 10.1007/978-3-540-68093-2

Schwab, C., & Gittelson, C. J. (2011, apr). Sparse tensor discretizations of high-dimensional parametric and stochastic PDEs. *Acta Numerica*, *20*(2011), 291–467. Retrieved from http://www.journals.cambridge.org/abstract{_}S0962492911000055 doi: 10.1017/S0962492911000055

Seyf, H. R., & Henry, A. (2016). Thermophotovoltaics: a potential pathway to high efficiency concentrated solar power. *Energy & Environmental Science*, *9*, 2654–2665. Retrieved from http://dx.doi.org/10.1039/C6EE01372D doi: 10.1039/c6ee01372d

Sheng, X.-Q., & Song, W. (2012). *Essentials of Computational Electromagnetics*. Singapore: John Wiley & Sons, Ltd. Retrieved from http://doi.wiley.com/10.1002/9780470829646 doi: 10.1002/9780470829646

Shin, R. T., & Kong, J. A. (1984). Scattering of electromagnetic waves from a randomly perturbed quasiperiodic surface. *Journal of Applied Physics*, *56*(1), 10–21. doi: 10.1063/1.333743

Shiraishi, K., Higuchi, S., Muraki, K., & Yoda, H. (2016). Silver-film subwavelength gratings for polarizers in the terahertz and mid-infrared regions. *Optics Express*, *24*(18), 20177–20186.

Shuai, Y., Tan, H., & Liang, Y. (2014). Polariton-enhanced emittance of metallic-dielectric multilayer structures for selective thermal emitters. *Journal of Quantitative Spectroscopy and Radiative Transfer*, *135*, 50–57. Retrieved from http://dx.doi.org/10.1016/j.jqsrt.2013.11.011 doi: 10.1016/j.jqsrt.2013.11.011

Silva-Oelker, G., Jerez-Hanckes, C., & Fay, P. (2018, Oct). Study of W/HfO2 grating selective thermal emitters for thermophotovoltaic applications. *Opt. Express*, *26*(22), A929–A936. Retrieved from http://www.opticsexpress.org/abstract.cfm?URI=oe-26-22-A929 doi: 10.1364/OE.26.00A929

Sinharoy, S., Weizer, V. G., Wakchaure, Y., Su, N., Fay, P., & Scheiman, D. (2005). Development of a very high efficiency, dot-junction, InGaAs Thermophotovoltaic (TPV) converter for deep space missions. *Conference Record of the IEEE Photovoltaic Specialists Conference*, 766–769. doi: 10.1109/PVSC.2005.1488245

Smolyak, S. A. (1963). Quadrature and interpolation formulas for tensor products of certain classes of functions. *Dokl. Akad. Nauk SSSR*, *148*(5), 1042 - 1045. Retrieved from http://mi.mathnet.ru/dan27586 doi: https://doi.org/10.1016/j.apnum.2010.08.002

Soifer, V. A. (2017). *Diffractive Optics and Nanophotonics: Resolution Below the Diffraction Limit*. Boca Raton, Florida: CRC Press Taylor and Francis Group.

Sokolowski, J., & Zolesio, J. P. (1992). *Introduction to shape optimization, Shape sensitive analisys*. Springer. Retrieved from http://www.springer.com/us/book/9783642634710

Solano, M., Faryad, M., Hall, A. S., Mallouk, T. E., Monk, P. B., & Lakhtakia, A. (2013, feb). Optimization of the absorption efficiency of an amorphous-silicon thin-film tandem solar cell backed by a metallic surface-relief grating. *Applied optics*, *52*(5), 966–79. Retrieved from http://www.ncbi.nlm.nih.gov/pubmed/23400058

Song, J., Si, M., Cheng, Q., & Luo, Z. (2016). Two-dimensional trilayer grating with a metal / insulator / metal structure as a thermophotovoltaic emitter. *Applied optics*, *55*(6), 1284–1290. doi: 10.1364/AO.55.001284

Song, J., Wu, H., Cheng, Q., & Zhao, J. (2015). 1D trilayer films grating with W/SiO2/W structure as a wavelength-selective emitter for thermophotovoltaic applications. *Journal of Quantitative Spectroscopy and Radiative Transfer*, *158*, 136–144. Retrieved from http://dx.doi.org/10.1016/j.jqsrt.2015.02.002 doi: 10.1016/j.jqsrt.2015.02.002

Stein, M. (1987). Large sample properties of simulations using latin hypercube sampling. *Technometrics*, *29*(2), 143-151. Retrieved from https://www.tandfonline.com/doi/abs/10.1080/00401706.1987.10488205 doi: 10.1080/00401706.1987.10488205

Steinbach, O. (2008). *Numerical Approximation Methods for Elliptic Boundary Value Problems*. New York, NY: Springer New York. Retrieved from http://www.springerlink.com/index/10.1007/978-0-387-68805-3http://link.springer.com/10.1007/978-0-387-68805-3 doi: 10.1007/978-0-387-68805-3

Stelmakh, V., Chan, W. R., Joannopoulos, J. D., Soljacic, M., & Celanovic, I. (2016). Sputtered tantalum photonic crystal coatings for high-temperature energy conversion applications. *IEEE-NANO 2015 - 15th International Conference on Nanotechnology*, *15*(2), 1134–1137. doi: 10.1109/NANO.2015.7388824

Stelmakh, V., Rinnerbauer, V., Geil, R. D., Aimone, P. R., Senkevich, J. J., Joannopoulos, J. D., ... Celanovic, I. (2013). High-temperature tantalum tungsten alloy photonic crystals: Stability, optical properties, and fabrication. *Applied Physics Letters*, *103*(12), 123903. Retrieved from http://scitation.aip.org/content/aip/journal/apl/103/12/10.1063/1.4821586 doi: 10.1063/1.4821586

Su, N., Fay, P., Sinharoy, S., Forbes, D., & Scheiman, D. (2007). Characterization and modeling of InGaAs/InAsP thermophotovoltaic converters under high illumination intensities. *Journal of Applied Physics*, *101*(6). doi: 10.1063/1.2713366

Sullivan, T. (2015). *Introduction to Uncertainty Quantification* (Vol. 63). Retrieved from http://link.springer.com/10.1007/978-3-319-23395-6 doi: 10.1007/978-3-319-23395-6

Sy, O. O., van Beurden, M. C., Michielsen, B. L., Vaessen, J. a. H. M., & Tijhuis, a. G. (2010). Second-order statistics of complex observables in fully stochastic electromagnetic interactions: Applications to EMC. *Radio Science*, *45*(4), 1–16. Retrieved from http://doi.wiley.com/10.1029/2009RS004216 doi: 10.1029/2009RS004216

Taillaert, D., Van Laere, F., Ayre, M., Bogaerts, W., Van Thourhout, D., Bienstman, P., & Baets, R. (2006). Grating couplers for coupling between optical fibers and nanophotonic waveguides. *Japanese Journal of Applied Physics, Part 1: Regular Papers and Short Notes and Review Papers*, *45*(8 A), 6071–6077. doi: 10.1143/JJAP.45.6071

Tan, M., Ji, L., Wu, Y., Dai, P., Wang, Q., Li, K., ... Yang, H. (2014). Investigation of InGaAs thermophotovoltaic cells under blackbody radiation. *Applied Physics Express*, *7*(9). doi: 10.7567/APEX.7.096601

Teofilo, V. L., Choong, P., Chang, J., Tseng, Y. L., & Ermer, S. (2008). Thermophotovoltaic energy conversion for space. *Journal of Physical Chemistry C*, *112*(21), 7841–7845. doi: 10.1021/jp711315c

Thorlabs. (2017). Introduction to diffraction grating [Computer software manual].

Toropov, A. A., & Shubina, T. V. (2015). *Plasmonic Effects in Metal-Semiconductor Nanostructures*. doi: 10.1093/acprof:oso/9780199699315.001.0001

Tran, H., Webster, C. G., & Zhang, G. (2016). A sparse grid method for bayesian uncertainty quantification with application to large eddy simulation turbulence models. In J. Garcke & D. Pflüger (Eds.), *Sparse grids and applications - stuttgart 2014* (pp. 291–313). Cham: Springer International Publishing.

Tsang, L., Kong, J. A., Ding, K.-H., & Ao, C. O. (2001). *Scattering of Electromagnetic Waves: Numerical Simulations*. New York, USA: John Wiley & Sons, Inc. Retrieved from http://www.wiley.com/WileyCDA/WileyTitle/productCd-0471388009.html

Ungaro, C., Gray, S. K., & Gupta, M. C. (2015). Solar thermophotovoltaic system using nanostructures. *Optics Express*, *23*(19), A1149. doi: 10.1364/OE.23.0A1149

Utlu, Z., & Önal, B. S. (2018, mar). Thermodynamic analysis of thermophotovoltaic systems used in waste heat recovery systems : an application. *International Journal of Low-Carbon Technologies*, *13*(May), 52–60. Retrieved from https://academic.oup.com/ijlct/article/13/1/52/4791145 doi: 10.1093/ijlct/ctx019

Veselago, V. G. (1968). The Electrodynamics of Substances With Simultaneously Negative Values of ε and μ. *Soviet Physics Uspekhi*, *10*(4), 509–514. Retrieved from http://iopscience.iop.org/article/10.1070/PU1968v010n04ABEH003699/meta{%}5Cnhttp://stacks.iop.org/0038-5670/10/i=4/a=R04?key=crossref.49e6b8a483029417bb518fd3889a3ed3{%}5Cnhttp://ufn.ru/en/articles/1968/4/d/ doi: 10.1070/PU1968v010n04ABEH003699

von Petersdorff, T., Schwab, C., von Petersdorff, T., & Schwab, C. (2006). Sparse finite element methods for operator equations with stochastic data. *Applications of Mathematics*, *51*(02), 145–180. Retrieved from http://link.springer.com/article/10.1007/s10492-006-0010-1

Wang, H., Chang, J.-y., Yang, Y., & Wang, L. (2016). Performance analysis of solar thermophotovoltaic conversion enhanced by selective metamaterial absorbers and emitters. *International Journal of Heat and Mass Transfer*, *98*, 788–798. Retrieved from http://dx.doi.org/10.1016/j.ijheatmasstransfer.2016.03.074 doi: 10.1016/j.ijheatmasstransfer.2016.03.074

Wang, L. P., & Zhang, Z. M. (2012). Wavelength-selective and diffuse emitter enhanced by magnetic polaritons for thermophotovoltaics. *Applied Physics Letters*, *100*(6), 063902. Retrieved from http://link.aip.org/link/APPLAB/v100/i6/p063902/s1{&}Agg=doi doi: 10.1063/1.3684874

Watanabe, K., Nakatake, Y., & Pištora, J. (2012, May). Accurate analysis of electromagnetic scattering from periodic circular cylinder array with defects. *Opt. Express*, *20*(10), 10646–10657. Retrieved from http://www.opticsexpress.org/abstract.cfm?URI=oe-20-10-10646 doi: 10.1364/OE.20.010646

Wedlockt, B. D. (1963). Thermo-Photo-Voltaic Energy Conversion. *Proceedings of the IEEE*, 694–698.

Wong, R. Y., Tso, C., Chao, C. Y., Huang, B., & Wan, M. (2018). Ultra-broadband asymmetric transmission metallic gratings for subtropical passive day-time radiative cooling. *Solar Energy Materials and Solar Cells*, *186*, 330 - 339. Retrieved from http://www.sciencedirect.com/science/article/pii/S0927024818303647 doi: https://doi.org/10.1016/j.solmat.2018.07.002

Wood, R. W. (1902). On a Remarkable Case of Uneven Distribution of Light in a Diffraction Grating Spectrum. *Proceedings of the Physical Society of London*, *18*(1), 269–275. Retrieved from http://stacks.iop.org/1478-7814/18/i=1/a=325?key=crossref.7ebbe1383fb00dffe4b52e1569cdd953 doi: 10.1088/1478-7814/18/1/325

Xiao, Z., Liow, T.-Y., Zhang, J., Shum, P., & Luan, F. (2013). Bandwidth analysis of waveguide grating coupler. *Optics Express*, *21*(5), 5688. Retrieved from https://www.osapublishing.org/oe/abstract.cfm?uri=oe-21-5-5688 doi: 10.1364/OE.21.005688

Xu, X., Ye, H., Xu, Y., Shen, M., Zhang, X., & Wu, X. (2014). Experimental and theoretical analysis of cell module output performance for a thermophotovoltaic system. *Applied Energy*, *113*, 924–931. doi: 10.1016/j.apenergy.2013.08.029

Xuan, Y., & Zhang, Y. (2014). Investigation on the physical mechanism of magnetic plasmons polaritons. *Journal of Quantitative Spectroscopy and Radiative Transfer*, *132*, 43–51. Retrieved from http://dx.doi.org/10.1016/j.jqsrt.2012.10.020 doi: 10.1016/j.jqsrt.2012.10.020

Yang, G., & Du, Y. (2014, may). An optimized Monte Carlo procedure and its application in electromagnetic scattering from rough surfaces. *IEEE Transactions on Geoscience and Remote Sensing*, *52*(5), 2607–2616. Retrieved from http://ieeexplore.ieee.org/lpdocs/epic03/wrapper.htm?arnumber=6578554 doi: 10.1109/TGRS.2013.2263637

Yeng, Y. X., Chan, W. R., Rinnerbauer, V., Stelmakh, V., Senkevich, J. J., Joannopoulos, J. D., … Čelanović, I. (2015). Photonic crystal enhanced silicon cell based thermophotovoltaic systems. *Optics Express*, *23*(3), A157. Retrieved from http://www.opticsinfobase.org/abstract.cfm?URI=oe-23-3-A157 doi: 10.1364/OE.23.00A157

Yeng, Y. X., Chou, J. B., Rinnerbauer, V., Shen, Y., Kim, S.-G., Joannopoulos, J. D., … Čelanović, I. (2014). Global optimization of omnidirectional wavelength selective emitters/absorbers based on dielectric-filled anti-reflection coated two-dimensional metallic photonic crystals. *Optics Express*, *22*(18), 21711. Retrieved from https://www.osapublishing.org/oe/abstract.cfm?uri=oe-22-18-21711 doi: 10.1364/OE.22.021711

Yeng, Y. X., Ghebrebrhan, M., Bermel, P., Chan, W. R., Joannopoulos, J. D., Soljačić, M., & Celanovic, I. (2012, feb). Enabling high-temperature nanophotonics for energy applications. *Proceedings of the National Academy of Sciences of the United States of America*, *109*(7), 2280–5. Retrieved from http://www.pubmedcentral.nih.gov/articlerender.fcgi?artid=3289359{&}tool=pmcentrez{&}rendertype=abstract doi: 10.1073/pnas.1120149109

Yong, S., Sid-ahmed, M. O., & Ming, X. (2014). One-dimensional Microstructure Tungsten Gratings for Thermo Photovoltaic Applications. *Research Journal of Applied Sciences, Engineering and Technology*, *7*(11), 2271–2277.

Yueh, H. A., Shin, R. T., & Kong, J. A. (1988). Scattering of electromagnetic waves from a periodic surface with random roughness. *Journal of Applied Physics*, *64*(4), 1657–1670. doi: 10.1063/1.341786

Zhang, Z. M. (2007). *Nano/Micro Scale Heat Transfer.pdf*. New York, NY: McGraw-Hill.

Zhao, B. (2016). *Thermal Radiative Properties of Micro/Nanostructured Plasmonic Metamaterials Including Two-Dimensional Materials* (PhD Thesis). Georgia Institute of Technology.

Zhao, B., Hu, M., Ao, X., Xuan, Q., & Pei, G. (2018). Comprehensive photonic approach for diurnal photovoltaic and nocturnal radiative cooling. *Solar Energy Materials and Solar Cells*, *178*, 266 - 272. Retrieved from http://www.sciencedirect.com/science/article/pii/S0927024818300230 doi: https://doi.org/10.1016/j.solmat.2018.01.023

Zhou, Z., Chen, Q., & Bermel, P. (2015). Prospects for high-performance thermophotovoltaic conversion efficiencies exceeding the Shockley-Queisser limit. *Energy Conversion and Management*, *97*, 63–69. Retrieved from http://dx.doi.org/10.1016/j.enconman.2015.03.035 doi: 10.1016/j.enconman.2015.03.035

Zhou, Z., Sakr, E., Sun, Y., & Bermel, P. (2016). Solar thermophotovoltaics: reshaping the solar spectrum. *Nanophotonics*, *0*(0), 1–21. Retrieved from http://www.degruyter.com/view/j/nanoph.ahead-of-print/nanoph-2016-0011/nanoph-2016-0011.xml doi: 10.1515/nanoph-2016-0011

APPENDIX A. GALERKIN METHOD

In this appendix a general procedure for the Galerkin-Bubnov method is given. For readers interested in the more abstract setting, theorems, and convergence see (Steinbach, 2008) and references therein.

Let us consider a bounded elliptic operator $\mathcal{A} : X' \to X$. For a given $f \in X'$ we want to find the solution $u \in X$ of

$$\mathcal{A}u = f. \tag{A.1}$$

Instead of solving A.1 we may consider an equivalent variational problem:

$$\langle \mathcal{A}u, v\rangle = \langle f, v\rangle, \quad \forall\, v \in X. \tag{A.2}$$

According to Lax-Milgram theorem there exists a unique solution of A.2. We consider the sequence

$$X_M := \text{span}\{\phi_k\}_{k=1}^{M} \subset X, \tag{A.3}$$

then we can write the approximate solution

$$u_M := \sum_{k=1}^{M} u_k \phi_k \in X_M \tag{A.4}$$

so that

$$\langle A u_M, v_M\rangle = \langle f, v_M\rangle \quad \forall\, v_M \in X_M, \tag{A.5}$$

where u_M is defined as the solution of the Galerkin-Bubnov variational problem A.5. Inserting the approximate solution A.4 in the last equation, we obtain:

$$\sum_{k=1}^{M} u_k \langle \mathcal{A}\phi_k, \phi_l\rangle = \langle f, \phi_l\rangle \text{ for } l = 1, 2, \ldots, M. \tag{A.6}$$

For $k, l = 1, \ldots, M$ this is equivalent to the linear system of equations:

$$\mathcal{A}_M \mathbf{u} = \mathbf{f}, \tag{A.7}$$

where $\mathcal{A}_M[l, k] := \langle A\phi_k, \phi_l\rangle$ and $f_l := \langle f, \phi_l\rangle$.

APPENDIX B. GREEN INTEGRAL THEOREMS

Green's integral theorems are a generalization of the integration-by-parts formula. Let us consider an open and bounded domain of dimension N $D \subseteq \mathbb{R}^N$ with a regular boundary $\Gamma = \partial D$ and a unitary vector $\hat{n}$ to that surface. Considering the function u and v we have:

- Green's first integral theorem

$$\int_D \Delta u v d\mathbf{x} = -\int_D \nabla u \nabla v d\mathbf{x} + \int_\Gamma \partial_\mathbf{n} v d\Gamma. \tag{B.1}$$

- Green's second integral theorem

$$\int_D (u\Delta v - v\Delta u) d\mathbf{x} = \int_\Gamma (u\partial_\mathbf{n} v - v\partial_\mathbf{n} u) d\Gamma. \tag{B.2}$$